March 2020

Development of a Monolithic Implantable Neural Interface from Cubic Silicon Carbide and Evaluation of Its MRI Compatibility

Mohammad Beygi
University of South Florida

Development of a Monolithic Implantable Neural Interface from Cubic Silicon Carbide and Evaluation of Its MRI Compatibility

by

Mohammad Beygi

A dissertation submitted in partial fulfillment
of the requirements for the degree of
Doctor of Philosophy in Electrical Engineering
Department of Electrical Engineering
College of Engineering
University of South Florida

Co-Major Professor: Stephen E. Saddow, Ph.D.
Co-Major Professor: Gokhan Mumcu, Ph.D.
Robert D. Frisina, Ph.D.
Arash Takshi, Ph.D.
Christopher L. Frewin, Ph.D.

Date of Approval:
March 27, 2020

Keywords: Michigan Style Neural Probe, Magnetic Resonance Compatibility, Monolithic Silicon Carbide, Brain Machine Interface

Dedication

To my lovely fiancé, Pavlina, and my wonderful family, who stand by me in all ups and downs of my life, who encourage me to reach further and whose love and dedication always inspire me to summit the highest peaks in my life.

Acknowledgments

I would like to express my sincerest appreciation to Dr. Stephen Saddow, who never stopped supporting me during my Ph.D. studies. Dr. Saddow was not only a wonderful advisor whose advice always showed me the right way, but also, he was a kind friend, a paragon of support, inspiration and encouragement during the past years. His inspiring advices, and discussions always helped me in my research and tuned my mindset as a researcher. Thanks for encouraging me during these years, helping me in the research and my personal life and thanks for believing in me.

I would also like to express my gratitude to my co-advisor, Dr. Gokhan Mumcu, who has given me the chance to have long discussions about the details of the project, whose suggestions and advice have been always extremely helpful in my research. I should also thank Dr. Mumcu for providing me with all the tools, software and hardware that were necessary in the research.

I would particularly like to thank Dr. William Dominquez of Moffitt Cancer Center, for his extraordinary support and amazing expertise in the MRI field. His in-depth understanding of MRI machines, both hardware and software, helped me learn a lot about MRI systems. His advice in the design and conducting experiments was undoubtedly crucial in this research.

Finally, I would like to thank all my committee members, Dr. Arash Takshi, Dr. Robert Frisina, and Dr. Christopher Frewin for their time and great advice. I truly appreciate all their invaluable support. I thank Dr. F. La Via of the IMM-CNR, Catania, IT, for providing the 3C-SiC epilayers used in this work. Also, thanks to the Silicon Carbide Biotechnology team, particularly Chenyin Feng and John Bentley for all their help during this work.

Table of Contents

List of Tables

List of Figures

Abstract

One of the main issues with micron-sized intracortical neural interfaces (INIs) is their long-term reliability, with one major factor stemming from device material failure caused by the heterogeneous integration of multiple materials used to realize the implant. Single crystalline cubic silicon carbide (3C-SiC) is a semiconductor material that has been long recognized for its mechanical robustness and chemical inertness. It has the benefit of demonstrated biocompatibility, which makes it a promising candidate for chronically-stable, implantable INIs. In the first section of this dissertation, the fabrication and initial electrochemical characterization of a nearly monolithic, Michigan-style 3C-SiC microelectrode array (MEA) probe is reported. The probe consists of a single 5 mm-long shank with 16 electrode sites. An ~8 µm-thick p-type 3C-SiC epilayer was grown on a silicon-on-insulator (SOI) wafer, which was followed by a ~2 µm-thick epilayer of heavily n-type (n^+) doped 3C-SiC in order to form conductive traces and the electrode sites. Diodes formed between the p and n^+ layers provided substrate isolation between the channels. A thin layer of amorphous silicon carbide (*a*-SiC) was deposited via plasma-enhanced chemical vapor deposition (PECVD) to insulate the surface of the probe from the external environment. Forming the probes on a SOI wafer enable the ease of probe removal from the handle wafer by simple immersion in HF, thus aiding in the manufacturability of the probes. Free-standing probes and planar, single-ended test microelectrodes, were fabricated from the same 3C-SiC epiwafers. Cyclic voltammetry (CV) and electrochemical impedance spectroscopy (EIS) were performed on test microelectrodes with an area of 491 μm^2 in phosphate buffered saline (PBS) solution. The measurements showed an impedance magnitude of 165 kΩ ± 14.7 kΩ (mean ± standard deviation)

at 1 kHz, anodic charge storage capacity (CSC) of 15.4 ± 1.46 mC/cm^2, and a cathodic CSC of 15.2 ± 1.03 mC/cm^2. Current-voltage tests were conducted to characterize the p-n diode, n-p-n junction isolation, and related leakage currents. The turn-on voltage was determined to be on the order of ~1.4 V and the leakage current was less than 8 μA_{rms}. This all-SiC neural probe realizes nearly the monolithic integration of device components to provide a likely neurocompatible INI that should mitigate long-term reliability issues associated with chronic implantation.

The second section of this dissertation focuses on evaluation of magnetic resonance imaging (MRI) compatibility of the 3C-SiC based neural implants. This was performed using various finite element method (FEM) and Fourier-based method simulations, and multiple experiments under 7 T MRI excitation in a small-animal Bruker system at the Moffit Cancer Center. The MRI compatibility in the current work mainly focuses on static magnetic field ($\mathbf{B_0}$) perturbation induced by the magnetic susceptibility differences between the probe and tissue phantom. In addition, induced tissue heating and specific absorption rate (SAR) distribution caused by electromagnetic coupling between the radio frequency (RF) field inside the MRI and conductive parts of samples fabricated were evaluated. Hereby, a comparative study with respect to MRI induced $\mathbf{B_0}$ perturbation, which are revealed via image artifacts, and MRI induced heating was presented to compare the MRI compatibility of 3C-SiC neural implants to reference materials fabricated from platinum (Pt) and silicon (Si). The results of the Fourier-based simulations to predict image artifacts and the experimental results show that free-standing 3C-SiC probes released from SOI handle wafers are completely invisible inside the MRI at 7 T while the reference materials produced severe image artifacts. In addition, FEM simulations show an ~30% maximum SAR reduction for 3C-SiC material comparing to Pt. These results are validated via experimental measurements and appear to indicate that fully-functional all-SiC INI devices may be MRI

compatible thus allowing for MRI as a diagnostic means to assess neural functionality without the need to first remove the INI.

Chapter 1: Introduction

1.1 Introduction and Motivation

The brain machine interface (BMI) creates pathways between an external controlling unit to the brain regions in order to build connections to the central nervous system through invasive or non-invasive means. Invasive methods result in high temporal and spatial resolution and gives access to the deep regions of the brain. In this method, BMI devices collect information from the brain regions and stimulates central nervous system which consequently gives rise to the creation of cortical neuroprosthetics via intra-cortical micro-stimulation (ICMS) and also treatment of several movement disorders via deep brain stimulation (DBS) [1], [2].

DBS is one of the most effective treatments for many central nervous system (CNS) disorders such as chronic pain, Parkinson's disease, tremors and dystonia [3]. These nervous system disorders are primarily treated via stimulation of deep brain regions. In this method, electrical pulses are generated and conveyed within the brain, all the way to the deep regions using long implanted electrodes which have stimulation sites placed at their tips [4]. Although this method has shown very promising results in the treatment of patients with movement disorders, the underlying mechanism that electrical pulses have in the treatment of these neurological disorders is obscure [5].

Neural implants offer a method for external electronic devices to be connected to the CNS in order to stimulate or record neurological signals, such as action potentials or multi-unit extracellular potentials, with the additional benefit of high spatial and temporal resolution. This interface forms a link for direct communication with the CNS through which the complex activities

of neurons can be decoded to control active prosthetic devices or to stimulate one or more neural circuits to restore or enhance physiological functions [6].

Long-term reliability of these neural implants is one the issues that limits the utilization of these implants in many cases. The desired long-term reliability for these devices is, in fact, the lifetime of the patient. In many cases, a desired device/system life-time, defined by robust design margins, should be over a century [7]. Therefore, long-term reliability is one of the most essential parameters when developing a neural implant for humans. Thus, the choice of material used for fabricating these neural implants is critical.

In the meantime, use of magnetic resonance imaging (MRI) as a standard diagnostic tool that forms high quality images of organs, will be highly restricted in patients with neural implants, throughout their life. In addition, MRI images are used to evaluate the outcome of treatments performed using neural implants. In addition, MRI is used by the surgeon to place the DBS lead properly as well as to find the right pathway through the brain tissue. Thus, any electromagnetic coupling between the MRI magnetic fields and neural implants may be risky for the patients. For this reason, in order for a neural implant to be reliable for patient life-time MRI compatibility of the neural implant should be also considered as a very important factor. Due to these considerations present-day (2020) medical practice calls for limiting MRI static magnetic fields, which determine imaging resolution, to less than 1.5 Tesla (T) in the presence of implants including catheters.

This chapter provides an overview of various technologies utilized to develop neural implants and explains several failure modes that these neural implants may undergo chronically or acutely which limits their long-term reliability. Following this, the material properties of silicon carbide (SiC), which is a semiconductor that our team is developing to improve the long-term reliability of these devices are introduced. Then, the magnetic resonance compatibility of neural

implants is discussed and the various forms of electromagnetic interference with these neural implants under MRI explained. Finally, the properties of cubic silicon carbide (3C-SiC) that give neural probes based on this highly promising material system potentially high MRI compatibility, are introduced. This serves as the foundation of the hypothesis that 3C-SiC can be a long-term reliable and MRI compatible neural implant, even for static magnetic (B) fields of 7 T.

1.2 Review of Neural Implant Technologies and Their Failure Modes

1.2.1 Overview of Neural Recording and Neural Implants

Attempts to understand the electrophysiology of the nervous system started in the 17th century with stimulation of frog sciatic nerve [8]. Later in the 19th century, stainless steel wire electrode arrays were first implanted in the amygdala nuclei of monkeys and cats to investigate brain activity [9]. This was followed by the implantation of tungsten microelectrodes in the visual cortex of cats to investigate the behavior of individual cortical cells [10]. Study of the visual cortex, which requires a denser array of electrodes, drove a transition from metal wire electrode arrays to silicon-based three-dimensional microelectrode arrays (MEAs), such as the Utah array, which was introduced in the late 1980s [11], [12]. This design minimized the electrode area and, as a result, allowed for higher spatial resolution during recording and stimulation of small populations of neurons, as well as utilized a reliable and repeatable manufacturing process. The high density of electrode sites, ability to individually address each electrode site, high-throughput fabrication, and compatibility with integrated circuit fabrication processes has made silicon an attractive material for high density, electrical neural interface applications.

A milestone in the development of silicon-based implantable intracortical neural interfaces (INIs) was the Michigan probe, introduced in 1970 [13], which employed multiple electrode sites on a single shank for chronic intracortical stimulation of, or recording from, single neurons [14].

In recent years, researchers developing neural implants have turned their focus to flexible materials and designs to develop tissue-like INIs that address both mechanical and form factor compatibility. One implementation is an ultra-flexible, polymer-based probe in which a metal layer is sandwiched between two layers of SU-8 polymer [15]. Although this polymer-metal probe, and other similar designs [16], [17], have shown a reduced immune response and were able to record action potentials and stimulate neurons, difficulty in the fabrication of these polymer-based devices, insertion of flexible polymer probes into the brain, and oxidation still remain fundamental issues [18]. Another method used to enhance the biocompatibility of neural probes are coatings that alter surface chemistry to provide hemostatic or immunomodulatory support [19]. In one example [20], a L1 protein coating was used to reduce microglial surface coverage. However, the surface coatings lose effectiveness over time leading to increased impedance and reduction in the recorded signals and, in some cases, the mechanisms through which modulation of neurodegeneration and the corrosive behavior of encapsulating cells occurred was unclear [21].

For an INI to stimulate and record neural signals reliably over many years, both the choice of material and their homogeneity must be carefully taken into consideration.

1.2.2 Failure Modes

The occurrence of mechanical, material, and biological failures, both acute and chronic [22], has been a major factor in the reliability of silicon- and metallic-based micro-INIs for human utilization. Mechanical failure, in the form of lead or connector breakage, material degradation, or

insulation delamination, along with concomitant biological failures, such as bleeding, cell death, meningitis, gliosis, and fibrotic encapsulation and extrusion, have been reported elsewhere [23]. In one report, collected from an evaluation of 78 silicon-based intracortical MEAs chronically implanted in rhesus macaques, nearly half of the chronic failures happened within the first year [24]. The majority of those chronic failures (53%) were reported as biological failure caused by meningeal encapsulation and extrusion from the tissue. These results indicate the importance of a mechanically and chemically robust INI that offers better compatibility with the CNS to provide long-term recording and stimulation capabilities.

In addition to the material, electrical and mechanical properties of INIs, their biocompatibility is also an essential factor that defines long-term reliability of the INIs. Together all of these factors determine the signal to noise ratio (SNR) of the recorded signals. Failure to satisfy any one of these factors can cause either acute or chronic loss of implant function [24].

From the material point of view, neural probes should possess sufficient mechanical strength to be able to tolerate stress while being implanted or exposed to brain micro-motions. In addition, higher flexibility is favorable when deflection occurs outside of the body or when a neural probe is implanted. Neural probes should be also thin enough to reduce damage to the tissue during surgical implantation [21].

In order to have a high SNR from the recording sites, the materials that are used to implement the conducting traces should possess high conductivity. Transferring a high amount of charge per activation period is essential to ensure adequate stimulation of the surrounding neurons. As described in [12], in order to facilitate this charge transfer from neural probes to the neighboring tissue, a thin layer of metal(s) or metal oxide, with low resistivity, is coated on the surface of the recording sites. Platinum, titanium, iridium, iridium oxide and titanium nitride are mostly utilized

for the realization of the recording sites [17], [23]–[28]. These materials have shown good in-vivo response and have been used for different types of neural implants. The properties of the insulating material which covers the shank and the conducting traces is also essential. It has been demonstrated that insulation material failure is the main reason behind electrical signal failure in-vivo [24]. A broad range of insulating materials have been used over the history of neural probes with different cons and pros. A review of these various insulating materials may be found in [24].

Biocompatibility of the materials used for fabricating neural probes is another factor which affects long-term INI performance. In fact, the quality of the recorded signals, as well as their durability and reliability, are highly influenced by neuro-inflammatory responses caused by the introduction of a foreign object in brain tissue [23]. In order to prevent this negative effect, many researchers have switched their attention to the important factor of biocompatibility of the materials used for fabricating neural implants. Different groups have developed various approaches in order to reduce tissue response and increase the biocompatibility of the neural implants. This includes size manipulation of the neural probes to decrease the stress around the implants, coating them with biocompatible materials, pharmaceutical approaches, and constructing them out of biocompatible materials [17] including various polymers and metals [26]–[28].

For an INI to stimulate and record neural signals reliably over many years, both choice of material and their homogeneity must be carefully taken into consideration. Crystalline silicon carbide (SiC) is a semiconductor with a short bond length that gives it high physical resilience and chemical inertness. One of the important properties of SiC is that it displays polymorphism, which results in numerous single-crystal forms with the principal being hexagonal (i.e., 4H- and 6H-SiC) and cubic (i.e., 3C-SiC) [29]. SiC has been used in both the high-power electronics and MEMS industries [30], [31] and recently in heat dissipation applications to improve through-plane thermal

conductivity [32]. It has also demonstrated a high degree of biological tolerance in vitro [33]–[38]. In addition, amorphous SiC (*a*-SiC), which provides excellent electrical insulation, has also shown good compatibility with neural cells [39]–[43], and has previously been used in the fabrication of several types of MEAs [39], [44]–[48]. The properties of crystalline and amorphous SiC, and the results of previous studies, indicate that SiC can address the interrelated issues of INI biocompatibility and long-term reliability.

1.3 Magnetic Resonance Compatibility of Neural Implants

1.3.1 Magnetic Resonance Imaging Overview

Magnetic Resonance Imaging (MRI) is a well-known technique that is used to both evaluate brain function, via functional MRI (fMRI), and measure changes in brain function after treatments such as medication or DBS [49]. The medical community is in need of neural interfaces that can remain in the brain during MRI scanning. Unfortunately, 'MRI compatible' neural probes have been of limited use as the maximum magnetic field they may be used with is limited to B=1.5 T for the most cases [50].

As mentioned above the material, electrical and mechanical properties of neural probes, as well as their biocompatibility, are factors that typically define reliability, durability and signal to noise ratio (SNR) of the signals recorded from neural probes. Failure to satisfy any of these factors can cause either acute or chronic loss of implant function [24]. In addition to these failure modes, another concern regarding implanted neural probes is patient safety when undergoing MRI scans [51].

MRI incorporates radio frequency (RF) signals, based on the precession of magnetic moments of hydrogen protons, to form an image of tissue in the body. MRI consists of three

different magnetic fields: a static B field (B_0), a gradient B field, and an RF (42.58 MHz/T) field (B_1) with varying amplitudes, all of which are synchronized to reconstruct an image of soft tissue. The strong static B_0 field (strength ranging from 0.3 to 9.4 T) lines up the spinning hydrogen protons. The gradient magnetic fields localize each part of the image by utilizing the method of frequency and phase encoding. Finally, the RF fields are transmitted perpendicular to the static magnetic fields to induce precession in the nuclei [50], [52].

Each of these three fields can interact with neural implants and the surrounding tissue which, as a result, can reduce image quality, and risk patient safety by inducing heating in the tissue surrounding the implants or damaging the tissue through induced mechanical vibration. Both the gradient and RF fields can induce current in the conducting parts of neural probes [53] . This induced current generates heat through Ohmic and dielectric losses. The gradient fields, on the other hand, can cause mechanical vibrations on neural implants based on the fact that a magnetic moment is induced on the probe as reported in [54], when patients with cervical fixation devices underwent MRI scans. Electric conductivity, magnetic susceptibility and thermal conductivity of materials define their degree of MRI compatibility.

1.3.2 Electric Conductivity versus MRI Compatibility

The electrical conductivity of materials has a direct correlation with the induced current when exposed to a high frequency electromagnetic (EM) field [55]. EM fields can be coupled into materials with high conductivity and, if the length of the metal is long enough (comparable to the wavelength of the EM field) [56], then a high frequency current is generated. This current then induces an EM field in the surrounding area. If metal is placed inside the brain tissue, the energy of the induced EM field will be absorbed by this tissue environment and consequently extra heat

is generated which can damage the tissue [57]. In addition, the induced current can dissipate heat through Ohmic loss in the conductive parts. The amount of absorbed energy by the tissue that causes the induced heating is defined by the specific abortion rate (SAR) in watts per kg (W/Kg). SAR defines the amount of energy absorbed by each unit of tissue weight under MRI and is the primary parameter used to assess MRI compatibility.

1.3.3 Magnetic Susceptibility versus MRI Compatibility

Magnetic susceptibility of a material defines its degree of magnetization in the presence of a magnetic field. It is a unitless term that can be either positive (attracted to magnetic fields) or negative (repelled from magnetic fields). Most metals, for instance, have high magnetic susceptibility which is considerably higher than that of tissue. This difference between tissue and metal susceptibility can cause magnetic perturbation in the vicinity of neural implants and also introduces image artifacts to the MRI receiver [58], [59]. This can be calculated mathematically for various B_0 intensities [60]. These artifacts make post-MRI scan processes almost impossible as, in the most cases, they are too extensive and greatly distort the image in the vicinity of the implant [59].

1.3.4 Thermal Conductivity versus MRI Compatibility

Thermal conductivity of a material is another factor that defines how well a device can transfer or dissipate heat. A material with a higher conductivity transfers heat away from hot spots thus preventing the accumulation of the heat in one place. Specifically, when excessive heat is induced inside an implantable device through Ohmic losses, to prevent damage to the tissue this

heat must flow away from the implant tip, otherwise it accumulates and increases the local tissue temperature, specifically in the case of long MR scans [61].

1.3.5 MRI Compatibility Literature Review

During the past decade, several studies have focused on the safety of implantable devices under MRI. Several techniques have been proposed to overcome the safety issue of implantable devices [53], [62]–[67]. However, most of the proposed techniques either are unable to find a long-term solution for this issue, or instead of improving the MRI compatibility of implants they focus their attention on MRI coils that are reconfigurable or patient adjustable [68]. While this approach has shown good results on paper, it is not a realistic solution as these devices may not be cost effective for most of testing centers, and it is not recommended for SAR values above that specified by the implant manufacturer. Also, the effectiveness of these reconfigurable coils is not guaranteed for over 1.5 T MRI systems. Another method that can influence the SAR intensity around implantable DBS electrodes is to replace the straight wires with helical wires. In spite of their effectiveness in reducing SAR, their impact in decreasing artifacts has not been studied to the best of our knowledge. In addition, helical wires can increase the effective volume of the implantable DBS lead which consequently increases the mechanical stress to the tissue and increases chance of failure in chronic implants [23].

In one of these studies [59], the severity of the artifacts caused by a magnetic susceptibility difference in metallic materials, or silicon, with tissue was investigated. This study showed that material magnetic susceptibility plays an important role in defining the intensity of the artifacts under MRI. It also concluded that, besides the magnetic and electrical properties of the implant

materials, the shape of the neural interfaces, their orientation with respect to the magnetic field, and the MRI pulse sequences also have an effect on artifact intensity.

Another study investigated the shape of the implanted probes and the relationship to the severity of the SAR in the surrounding tissue [69]. In this study, several generic straight and helical implanted electrodes were designed and used for the experiments. The study concluded that the SAR around the helical implant is less severe in comparison to the straight implants but did not state if any artifact changes were observed.

Other studies have investigated the effect of redesigning the MRI coil in order to reduce the EM fields around DBS implants. In these studies, the coil design was modified in a way so that minimal coupling occurred to the implantable devices. Golestanirad, et al. [68] used a rotatable linearly polarized coil instead of a circularly polarized coil. In this reconfigurable coil, there is a region that has very low EM field intensity. By adjusting this low-intensity EM region for a particular patient, the high frequency EM field will be very low in energy around the implants and hence the absorbed energy induced by the implant to the surrounding tissue is decreased.

Regarding the heat induced by the gradient magnetic and RF fields in implanted devices, several in-vitro and in-vivo simulation studies have been conducted in order to estimate the temperature rise induced by each MRI scan [70]–[75]. The range of the temperature rise reported by each study is widely diverse and essentially dependent on the probe materials and geometry, frequency and intensity of the magnetic fields and many other factors which can influence the results of each experiment.

There have been several cases with serious injuries caused by MRI-induced heat reported in the literature. In one case, reported in [76], a 56-year-old male patient was subjected to DBS for the treatment of Parkinson's disease. After he underwent multiple MRI scans in a 1-T MRI system,

this patient displayed serious neurological deficits immediately after the session. The computed tomographic (CT) scan in Figure 1-A shows clearly the hemorrhage surrounding the DBS electrode on the left side of his brain. It is believed, after very careful examination of this case, that this injury was caused by RF induced heating even at a very low B field of 1 T.

Thermal conductivity of materials is a measure of their capability to conduct heat. If this quantity is low in a material, induced heat may accumulate at one spot and thus cause a significant temperature rise. The thermal conductivity of SiC is relatively high and approximately that of copper at room temperature (copper being used as a heat sink in electronics as a point of reference). The nominal value for SiC thermal conductivity is between 3.3 and 4.9 $W \cdot cm^{-1} \cdot K^{-1}$ [77]. While SiC thermal conductivity is similar in all of the various polytypes, the doping level and crystal direction may change this value [78]. The thermal conductivity of SiC is comparable to metals (e.g. pure copper is ~ 4 $W.cm^{-1}.K^{-1}$) and much higher than that of silicon (1.4-1.5 $W \cdot cm^{-1} \cdot K^{-1}$) [77]. Under MRI scans, due to EM coupling between conductive traces and the RF and gradient magnetic fields, an electric current may be induced in the passive conductive traces. This current may cause heat generation within the traces due to ohmic losses and in the tissue via dielectric losses. Both these mechanisms increase the temperature surrounding the neural implant. If a high thermal conductivity material is used on the stimulation sites and traces, this induced heat may flow away from the stimulation sites, reducing the local temperature to ideally below the SAR damage threshold.

As mentioned in Section 1.3.3, a materials magnetic susceptibility χ defines their level of magnetization when exposed to magnetic fields. This can be either negative (diamagnetic), which means the magnetization is aligned opposite to the applied magnetic field. Conversely a positive χ means that the magnetization is aligned in the direction of the applied magnetic field. Thus, the

magnetization caused by the magnetic susceptibility of materials can shift the net local static magnetic field during MRI. Human brain tissue has a very weak diamagnetic property, with susceptibility $\chi \sim -9$ ppm. Generally, due to the inhomogeneity of human tissue and also the magnetic field inside the MRI, magnetic perturbation may happen during a scan. Another scenario happens when there is another foreign object that has a different magnetic susceptibility. An implant inside the brain tissue is an example of this situation. In this case, as the implant has a different magnetic susceptibility than that of the brain tissue, a much larger frequency shift may occur (as large as 100 Hz for each ppm under 7 T [79]). This frequency shift causes artifacts to be displayed in MRI images [79]. In order to keep these artifacts as low as possible in the case of a brain implants, the implant should be fabricated with a material that has a magnetic susceptibility as close as possible to that of the brain tissue. SiC has a magnetic susceptibility $\chi = -12.87$ ppm, which in comparison with platinum (267 ppm) and silicon (-3.24 ppm), is very close to that of human tissue ($\chi \sim -9$ ppm). However, the magnetic susceptibility values may vary in semiconductors depending on their doping type (n or p) and possibly their doping densities [80], [81].

1.4 MRI Compatibility of Silicon Carbide Neural Probe

One of the most interesting polytypes of SiC is the cubic type known as 3C-SiC. 3C-SiC is a chemically inert semiconductor material with ceramic-like properties and is the only polytype which can be grown on silicon substrates. 3C-SiC based neural implants is a possible implant material which may be compatible with MRI fields. Due to the high thermal conductivity of 3C-SiC, its tissue-compatible magnetic susceptibility, and the ability to form relatively high resistivity conductive traces, in comparison with metals, neural probes fabricated monolithically from 3C-

SiC may reduce the magnetic perturbation caused by magnetic susceptibility differences. In addition, it decreases the heat generated by MRI induced currents on the neural probes' conductive traces. This was noticed in an initial experiment whereby no image artifacts were observed in a 2T MRI field whereas an 'MRI compatible' neural probe, composed of PtIr insulated with parylene C, induced severe image artifacts. This is shown in Figure 2 [82].

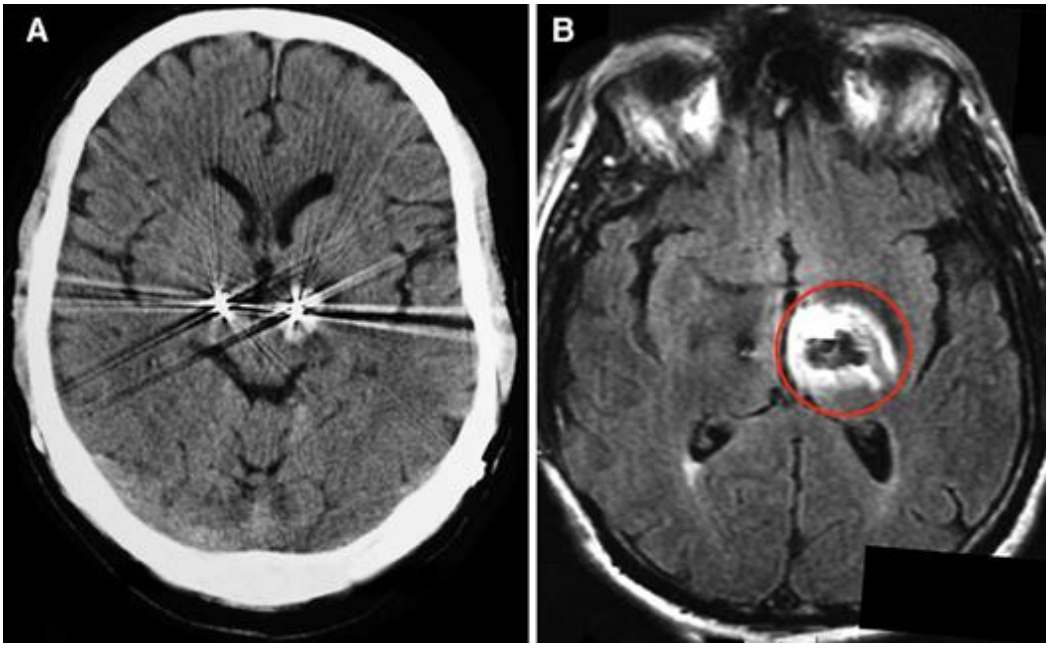

Figure 1.1. A Computerized tomographic (CT) scan of a 56-year-old male brain with DBS in the left hemisphere after undergoing multiple MRI scans showing hemorrhage surrounding the DBS electrode. B) MRI image indicating edema surrounding the DBS electrode (red circle) indicating serious damage to brain [76]. Reprinted from [76], with permission from OXFORD University Press.

Previously it was noted that the thermal conductivity of a material indicates their capability in conducting heat which would reduce the risk of hot spots in tissue surrounding an implant during MRI scanning. The thermal conductivity of SiC is relatively high at between 3.3 and 4.9 $W \cdot cm^{-1} \cdot K^{-1}$ depending on the polytype [77]. While SiC thermal conductivity is similar in various

polytypes, the doping level and crystal direction may change this value [78]. The thermal conductivity of SiC is comparable to that of metals (e.g. pure copper is ~ 4 $W \cdot cm^{-1} \cdot K^{-1}$) and much higher than that of silicon (1.4-1.5 $W \cdot cm^{-1} \cdot K^{-1}$) [77]. Under MRI scanning, due to EM coupling between conductive traces and RF and gradient magnetic fields, an electric current may be induced in the passive conductive traces. This current may cause induced heating within the traces due to ohmic losses and in the tissue via dielectric losses. Both mechanisms increase the temperature surrounding the neural implant. If a high thermal conductivity material is used on the stimulation sites and traces, this induced heat is expected to flow away from the stimulation sites, reducing the local temperature. This is one important reason why SiC may be an excellent candidate to construct neural implants as it should decrease localized induced heat during MRI scans.

As mentioned in Section 1.3.3, material magnetic susceptibility defines their level of magnetization when exposed to magnetic fields.

One additional factor, in terms of why 3C-SiC may be an ideal choice for neural implants exposed to MRI fields, is that this material is ceramic-like in nature and interacts with the brain tissue through capacitive, rather than a conductive, mechanism. In a capacitive interface, no ionic species are transferred between the brain and probe. Instead charging and discharging of the electrode-electrolyte double layer occurs which is very important: reactive chemical species are not involved in charge transfer thus reducing both tissue and implant material damage as is often the case when Faradaic reactions are present [83]Thus, having a highly conductive electrode may not be necessary to increase the charge-discharge cycle occurring at the interface curing device operation. In addition, the porosity of the material used to fabricate the electrode may help increase the amount of charging that occurs at the interface [83]. This mechanism enables the fabrication of electrodes with relatively high resistance due to enhance charge transfer, although high

resistance may decrease SNR. By doping 3C-SiC to semi-metallic levels (N_D~10^{19} cm^{-3}), one can expect to achieve an adequate SNR while decreasing the EM coupling during MRI scans.

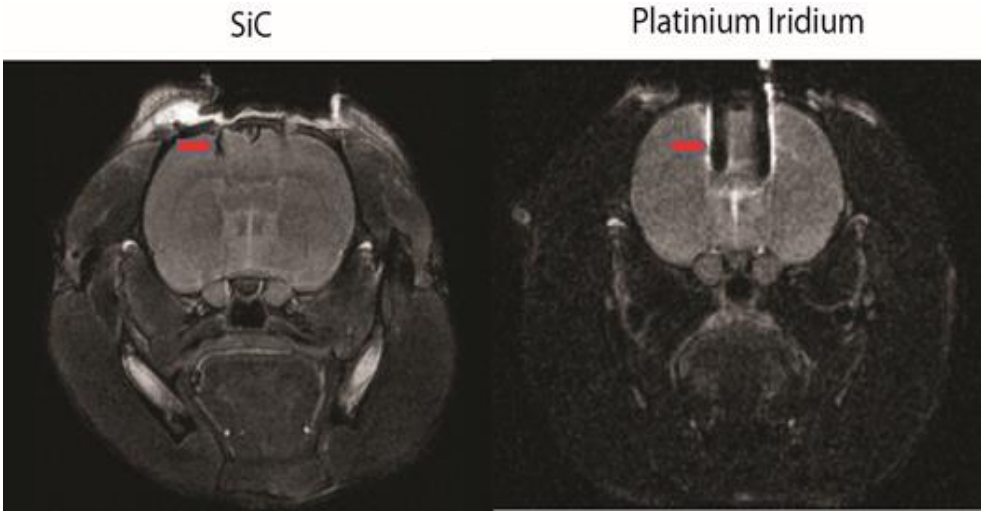

Figure 1.2. Comparison of 3C-SiC (left) probe and PtIr MRI compatible probe (right) during 2T MRI scan in a rat. Note image artifacts (white contrast) in vicinity of PtIr implant while no artifact was observed for 3C-SiC. Image taken by Dr. Jackeline Malheiros, USP São Carlos, Brazil [82]. Reprinted from [82] with permission from Elsevier.

1.5 Chapter Summary

Cubic silicon carbide (3C-SiC) is mechanically robust, chemically inert, and has shown high bio- and hemocompatibility in several in-vitro and in-vivo studies. All of these properties indicate that this material may be an excellent candidate for developing highly stable neural implants that function in the body for many years. In addition to these properties, the tissue compatible magnetic susceptibility of 3C-SiC, and its high thermal conductivity, may help to reduce the magnetic perturbation with minimum temperature rise under MRI. Also, in the case of developing a monolithic neural probe from 3C-SiC material, by manipulating the doping level in the conductive traces, one can realize an optimized resistance in these traces. With an optimum

resistance value, these traces can still allow for adequate SNR while the induced current and resulting device/tissue heating from electromagnetic coupling under MRI is reduced.

Due to the properties of 3C-SiC mentioned above, this material is believed to possibly be MRI compatible. Throughout this work, the author utilizes scientific methods, computational analysis and experiments to test this hypothesis. in order to accomplish this objective, a micro-fabrication process was developed that realizes a monolithic Michigan style 3C-SiC neural probe. Initial electrical and electrochemical characterizations were also performed indicating neural electrode performance superior to state-of-the-art platinum electrodes. Based on these very promising results these same probes were used to evaluate the MRI compatibility of 3C-SiC which forms the base of the research reported here in this dissertation.

1.6 Dissertation Organization

In Chapter 2 the theory and definitions that are needed to test our hypothesis are presented. This includes basics of semiconductors, specifically wide-band-gap semiconductors, the semiconductor-neuron interface, physics of magnetic resonance imaging and resonance coils, as well as MRI safety factors. Chapter 3 then presents the fabrication and characterization of monolithic 3C-SiC neural implants upon which the MRI compatibility is presented in Chapter 4 which compares this material system to both silicon and various neural implant materials such as gold and platinum. Finally, the dissertation is summarized in Chapter 5 where a list of suggested future work is presented in the hope that this work will continue, ultimately resulting in a commercialized MRI-compatible neural interface for the biomedical community.

Chapter 2: Theory and Overview

2.1 Introduction and Chapter Overview

In this chapter, the basic theory and knowledge involved in developing the monolithic 3C-SiC neural probes, and evaluating their MRI compatibility, is explored.

The first part of this chapter focuses on semiconductor materials and their properties, specifically on SiC as a wide-band-gap semiconductor. First, the basics of solid-state physics are discussed which covers semiconductor crystalline structure, energy bandgap, and doping. Then, p-n and metal-semiconductor junctions are discussed. This part is closed by introducing semiconductor-electrochemical interface and the mechanism for charge transfer in solution which mimics the behavior in tissue.

The second part focuses on MRI basics, and the electromagnetic theory behind MRI scans. After the basics are covered, MRI interactions with various material types and MRI compatibility of materials are discussed. Finally, various types of RF coils, which are used for producing RF signals, are discussed with special attention to the, volume birdcage coil which is used in this work.

2.2 Semiconductors Basics

2.2.1 Introduction

Semiconductors are materials whose electrical conductivity falls between that of conductors and insulators. By adding an impurity to the semiconductor crystal lattice, their electrical conductivity changes. Depending on the impurity atoms incorporated, semiconductors may contain an excess of electron (n-type) or hole (p-type) carriers. This gives semiconductors

different electrical, mechanical, electromagnetic and thermal properties [84]. Although the added impurities represent a very small portion of the total atomic density of the host material, it has a tremendous effect on defining the host physical properties. The density of these carriers varies between 10^{14} - 10^{19} cm^{-3}, which is much smaller than the atomic density of semiconductors which is on the order of 10^{23} cm^{-3}.

A junction between an n-type and a p-type semiconductor creates a p-n junction device that is the foundation of diodes, transistors and integrated electronics. These electronic components are the base of all the devices we have access to on a daily basis. In addition, compound semiconductors, composed of two or more atomic species, can give a wide range of properties to semiconductors, thus expanding their utilization [85].

2.2.2 Crystalline Structure

In terms of solid-state crystal formation, semiconductors are generally categorized into three different crystal types: single (or mono-) crystalline, poly-crystalline and amorphous. A single crystalline semiconductor is composed of a crystal unit cell with a specific atomic structure which continues throughout the sample in a periodic manner. Poly-crystalline semiconductors, on the other hand, contain single crystalline grains that are separated from each other inside the semiconductor via borders called grain boundaries. Finally, amorphous semiconductors contain atoms that are randomly placed inside the lattice and display no long-range periodicity inside the lattice [86]. Figure 2.1 illustrates crystalline and amorphous structures in semiconductors.

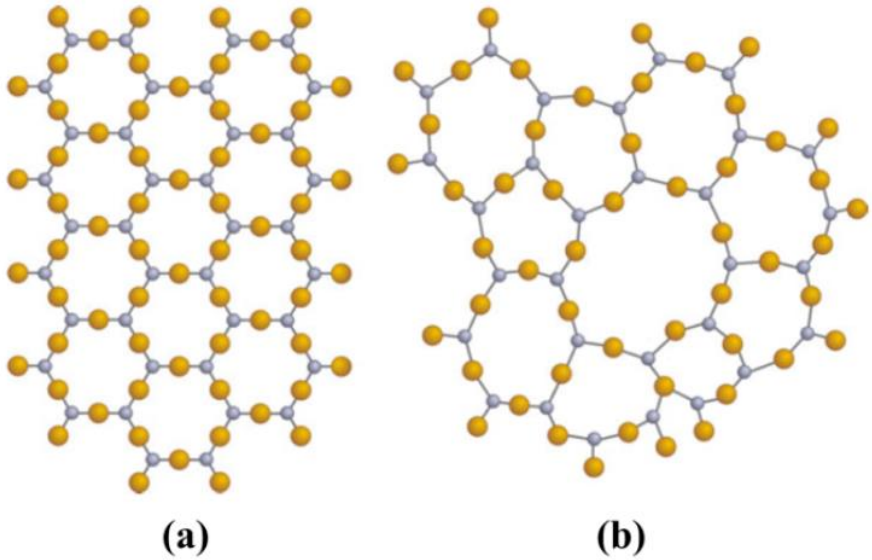

Figure 2.1. Illustration of (a) crystalline and (b) amorphous semiconductor [84]. Reprinted from [84] with permission from Springer.

Most semiconductors are from group IV of the periodic table which are composed of elemental species including silicon (Si), germanium (Ge), tin (Sn), selenium (Se) and tellurium (Te). The semiconductor elements in the periodic table are shown in Figure 2.2 [84]. In addition, a combination of elements in different groups results in compound semiconductors, which gives this group a different range of physical properties. For example, gallium arsenide (GaAs) is a binary compound which consists of Ga from group III and arsenide from group V (i.e., a III-V compound semiconductor). This combination gives this compound semiconductor a higher electron mobility, and saturated electron velocity that makes it more ideal for high-speed electronics [87]. Another compound semiconductor that is the base of the current work is silicon carbide, which consists of Si and C, both from IV group. Hence SiC is a Group IV-IV compound semiconductor.

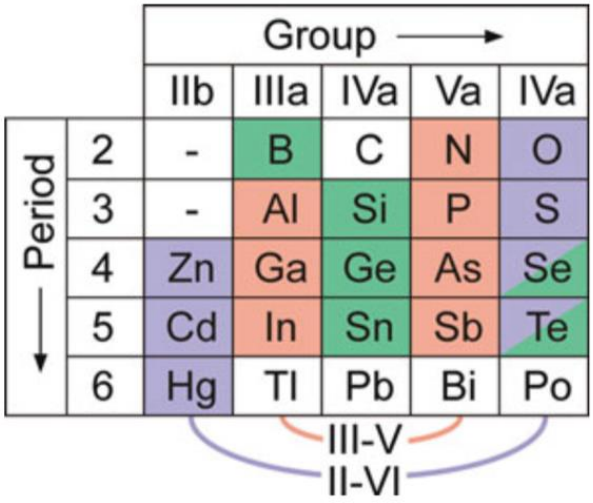

Figure 2.2. Semiconductor elements in the periodic table. The green color illustrates the single-species (elemental) semiconductors, while orange and purple indicate compounds of III-V and II-IV [84]. Reprinted from [84] with permission from Springer.

2.2.3 Semiconductor Energy Bandgap

In solid-state physics, the energy band gap defines the energy level that charge carriers inside a solid material need to have to jump from the valance band to the conduction band in order to conduct electric current. This is an energy level is defined based on electron transport and, thus, is in units of electron volts (eV). The energy required to transfer an electron across the gap may come in the form of a phonon (heat/vibration) or photon (light) [84]. In general, insulators have the highest, and metals have the lowest, band gap which is illustrated in Figure 2.3. Semiconductors thus have an intermediate bandgap compared to insulators metals and, at room temperature, it is relatively easy to apply the required energy to 'switch' the semiconductor state which is why they are so useful. The energy of the band gap in semiconductors is dependent on the type of semiconductor, which defines its electrical properties [84].

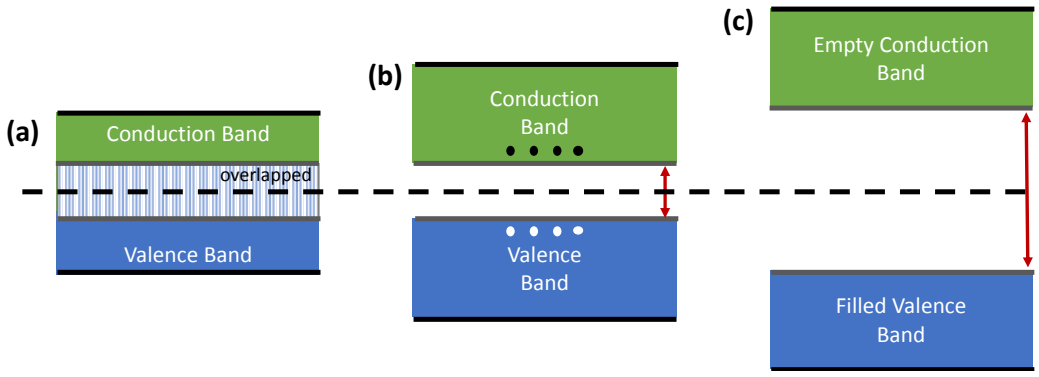

Figure 2.3. Figure. The red arrows illustrate the level of energy band gap in different solids. Note that in metals the valence and conduction bands typically overlap, or are a few mV.

2.2.4 Doping

Various impurities are added to semiconductors in order to change their electrical, mechanical, thermal, optical and magnetic properties. The type of dopant present defines the properties that a doped semiconductor displays [88]. A semiconductor without any dopant impurities is called an intrinsic semiconductor. The dopant concentration can define many electrical properties in semiconductors; thus it is the primary characteristic used to both design electronic devices and evaluate their performance. By increasing the doping level, the carrier concentration increases and, as a result, a higher number of chargers are involved in electrical conduction and consequently the electrical resistivity of the semiconductor drops [89]. The concentration of electrons and holes in an intrinsic semiconductor in thermal equilibrium is equal thus the material is 'charge neutral' as it does not display either an excess of electrons or holes (a hole being the absence of an electron). The relationship between electron concentration, n, and hole concentration, p, is found using the mass-action law:

$$n = p = n_i \qquad \textit{(Equation 2.1)}$$

When an impurity is added to the semiconductor, then product of the impurity densities is a function of the intrinsic carrier concentration as follows:

$$n_0 \times p_0 = n_i^2 \qquad \textit{(Equation 2.2)}$$

In equations 2.1 and 2.2, n_0 and p_0 are the electron and hole concentration due to impurity doping while n_i is the intrinsic carrier concentration.

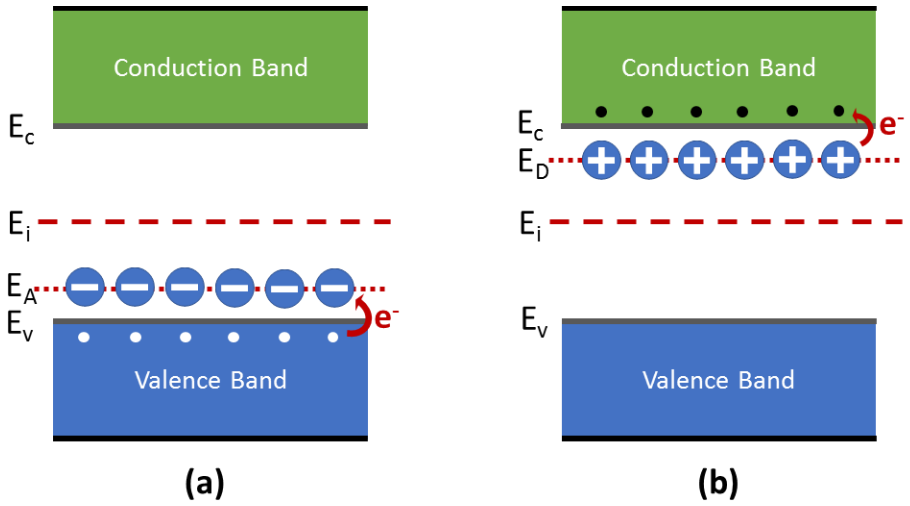

Figure 2.4. Energy levels in the band gap are produced by adding dopants to an intrinsic semiconductor. (a) Adding electron acceptors creates an acceptor level close to the valence band. The blue circles with negative signs show activated acceptor ions and the white dots inside the valence band indicates holes formed after electrons were captured by the acceptor dopants. (b) Adding electron donors to semiconductor creates a donor energy level near the conduction band. Circles with positive signs indicate activated donor ions and the black dots indicate electrons donated to the conduction band.

Doping with impurities adds additional energy levels between valence and conduction bands (i.e., in the band gap). Depending on type of dopants, these energy levels are either created near the valence or conduction band. If an acceptor dopant is added to a semiconductor, an extra

energy level is formed near the valence band, while a donor dopant creates a level below the conduction band [86]. This effect is illustrated in Figure 2.4.

2.2.5 P-N Junction

An abrupt change in impurity profile within a semiconductor forms a junction at the interface where the change occurs. If one side of the junction is p-type and the other part n-type, this forms the so-called pn junction. The pn junction allows electrical current to flow through the semiconductor principally in one direction only, while in the opposite direction the semiconductor blocks the current [90]. In the semiconductor, both p-type and n-type regions can conduct electricity, and at the junction site a charge depletion region, also called a space-charge region, is formed. When there is no bias on the semiconductor, this depletion region keeps electrons from the n-side, and holes from the p-side, separated from each other. In order to overcome this depletion region and pass electric current through the p-n junction diode, an electric field must be applied across this region to transport the charges from one side of the depletion to the other side. The amount of bias voltage that is needed to overcome the depletion region energy barrier is called built-in voltage, V_{bi} [84]. The value of the built-in voltage is semiconductor-dependent and primarily is related to the band gap energy, E_G. The built-in voltage is calculated as follows:

$$\boldsymbol{V_{bi} = \frac{KT}{q} ln \left(\frac{N_D . N_A}{n_i^2}\right)} \qquad \textit{(Equation 2.3)}$$

where N_D and N_A are the donor and acceptor doping concentration, respectively, K is the Boltzman constant, T is temperature in Kelvin and q is the electron charge.

Charges are transported across the space charge region in both diffusion and drift modes. At equilibrium, when there is no bias voltage across the diode, drift and diffusion currents cancel out each other making a zero net current inside the diode [86]. The current-voltage (IV)

characteristic of a diode is illustrated in Figure 2.5. When the diode is forward biased, the depletion region starts narrowing down and as a result more carriers can pass through the depletion and conduct electricity. As the forward bias voltage increases, at the knee of the IV curve, the diode turns on and the diffusion current flows. Once the diode is reverse biased, the diffusion current stops flowing. However, due to the presence of the minority carriers and built-in electric field, a small amount of current still exists that is called leakage current. If the reverse voltage continues rising, then at some point when the electric field is high enough, the carriers can move across the pn junction and therefore the pn junction breaks. This voltage is called breakdown voltage [84].

2.2.6 Metal-Semiconductor Contacts

Metal semiconductor contacts can be either ohmic or Schottky, depending on the metal used, the doping type and doping density of the semiconductor. In the development of 3C-SiC neural probes, it is very critical to be able to form a good quality ohmic contact to connect the electrodes to an electronic interface. Here the parameters involved in ohmic and Schottky contact formation is discussed, which allows us to choose the right metal or metal alloy for creating ohmic contacts on the neural probes.

Metal-semiconductor contacts can be explained using the energy-band diagram. Figure 2.6 illustrates the energy-band diagram of a metal-semiconductor contact during various stages of its [86]. First, we assume no contact is formed at the junction as shown in Figure 2.6 (a). This figure illustrates the energy-band diagram of the metal and semiconductor in two separated systems. The metal work function ($q\varphi_m$) in this graph is the potential difference between the metal Fermi level and vacuum. When a junction between the metal and the semiconductor is formed, the Fermi level equalizes in the two solids, otherwise a current will flow inside the junction in equilibrium [91].

On the other hand, the work function in the semiconductor is the summation of the semiconductor electron affinity ($q\chi$), and the energy difference between the Fermi level (which is doping-dependent) and the conduction energy band ($q\varphi_n$) in the semiconductor. Before equilibrium, because the Fermi level of the semiconductor is less than that of the metal, electrons flow from the semiconductor into the metal. Due to this movement of electrons, an electric field is formed at the interface between the metal and the semiconductor. Thus, a potential difference exists between the two sides of the metal-semiconductor junction.

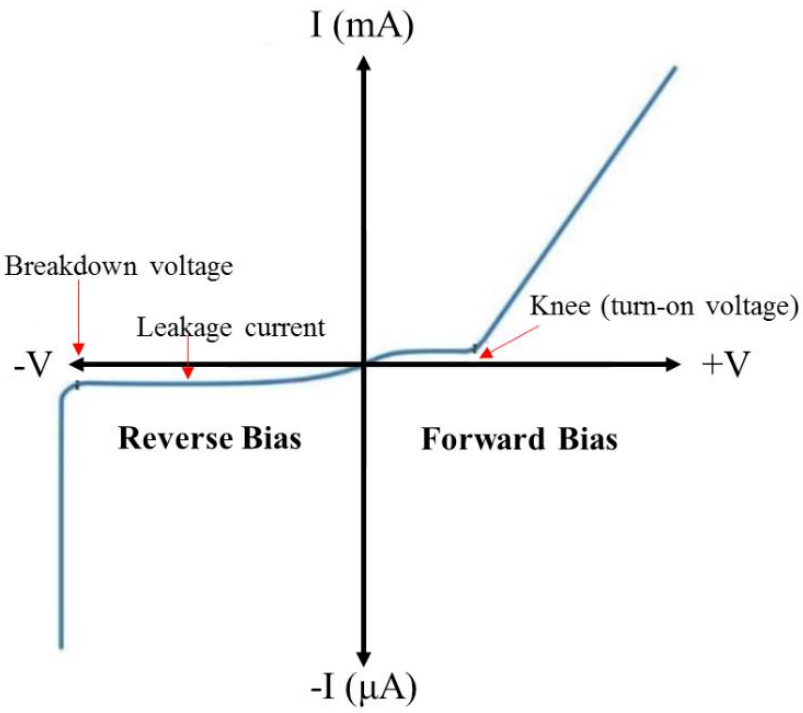

Figure 2.5. The current-voltage (IV) characteristic of a diode. When the diode is forward biased, the depletion region starts narrowing down and as a result more carriers can pass through the depletion. As the forward bias voltage increases, at the knee of the IV curve, the diode turns on and the diffusion current flows. Once the diode is reverse biased, the diffusion current stops flowing. Due to the built-in electric field, a small amount of current, called leakage current, still flows. If the reverse voltage continues rising, then at some point when the electric field is high enough, the carriers can move across the pn junction and therefore the pn junction breaks. This voltage is called breakdown voltage.

When the energy gap at the junction reduces, the electric field in the gap increases and leads to an accumulation of electrons on the metal side. When this gap reduces even further, then

the electrons can pass through it and a barrier is established. After the creation of the barrier, called a Schottky barrier, the electrons from the semiconductor are repelled from the barrier and this causes an accumulation of positive ions inside the depletion region. The height of the barrier is the difference between the work function of the metal and the electron affinity of the semiconductor as illustrated in Figure 2.6 (d), and calculated as follow [86],

$$q\varphi_{n0} = q(\varphi_m - \chi) \qquad \textit{(Equation 2.4)}$$

In order to make a pure ohmic contact, as is necessary in the development of 3C-SiC neural probe, a metal or metal-alloy should be chosen so that the Schottky barrier is minimum, otherwise a Schottky diode is formed at the junction.

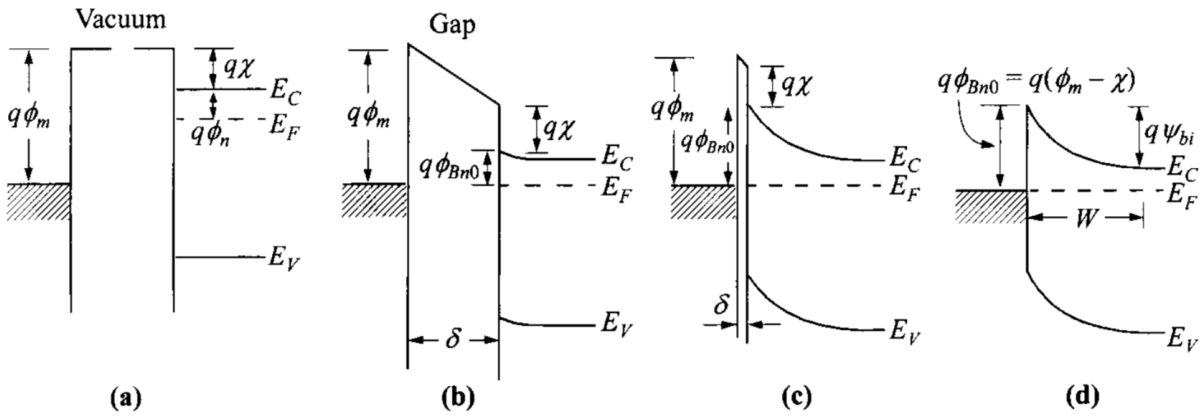

Figure 2.6. Creation of a metal-semiconductor junction. The semiconductor is n-type. (a) This shows two semiconductor and the metal in two different systems before the junction. (b) Two solids are connected and (c) the gap between them decrease, and finally (d) the gap is vanished and the barrier is formed [86]. Reprinted from [86] with permission from John Wiley and Sons.

2.2.7 Semiconductor-Electrolyte Interface

The interface between a semiconductor and electrolyte is capacitive, meaning that no chemical species are produced during the process. This is opposite to the faradaic interface in which actual charges are transferred between the solid and the electrolyte [83]. In a semiconductor-

electrolyte interface various electrochemical and electrical reactions occur which leads to the accumulation of charges across the interface. These reactions take place in three different regions at the semiconductor-electrolyte interface which are double layers: space charge region (SCR) in the semiconductor, the Helmholtz double layer (HL), and the Gouy Layer (GL) inside the electrolyte [91].

The SCR can be discussed using energy band and states terminologies. In the case of an n-type semiconductor inside an electrolytic solution with oxidizing species, prior to equilibrium, the electrons transfer from the semiconductor to the electrolyte and this results in a space lacking negative charges in comparison to the bulk of the semiconductor. Because E_{redox}, which is an energy level in an electrolyte between the energy band of reducing species and oxidizing species in the electrolyte, is lower than the Fermi level of the semiconductor then the valence and conduction bands bend up. This is shown in Figure 2.7 (a).

Another layer of electrochemical species that is formed close to the semiconductor-electrolyte interface is the HL that is a planar sheet of negative ions (in the case of an n-type semiconductor) and another sheet of positive ions attracted by the negative ions. The GL is a layer that has excess of one type of the charge which is caused by the electric field normal to the layer. This is shown in Figure 2.7 (b).

2.2.8 Silicon Carbide Material Overview

Silicon carbide (SiC) is a compound semiconductor. The specific chemical structure of molecules in SiC, such as very short length covalent bonding between Si and C that forms a tetrahedron bilayers (Figure 2.8), gives it a remarkable chemical and mechanical stability [29]. SiC

can be formed in polycrystalline, monocrystalline and amorphous forms and it has different mechanical, chemical and electrical properties depending on the crystalline formation [92].

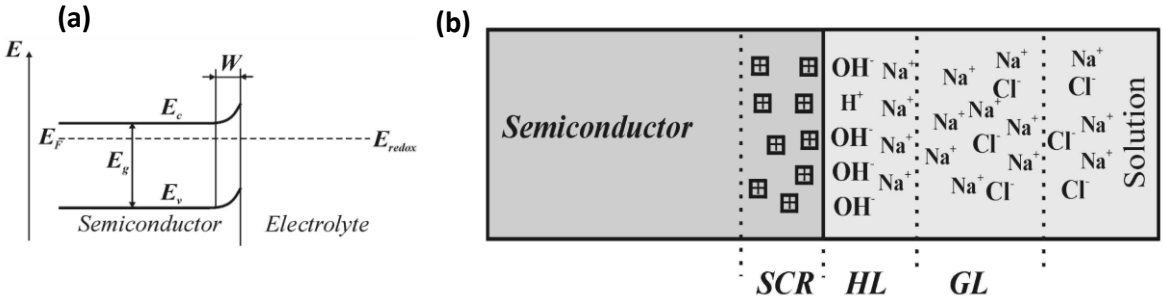

Figure 2.7. Semiconductor-electrolyte interface. (a) Energy band diagram of a semiconductor-electrolyte interface. If E_{redox} is lower than the Fermi level of the semiconductor then the valence and conduction states are bent up. (b) The double layers formed at the interface between the semiconductor-electrolyte interface [91].

There are more than 200 crystalline types of SiC formed in three main crystallizations of fully cubic (β-SiC) and two hexagonal structures (α-SiC). The cubic crystalline form of SiC is denoted in the literature by 3C-SiC, with 3 indicating that three bilayers of Si and C are needed to form the cubic lattice. The hexagonal crystalline forms consist of 4H-SiC and 6H-SiC, with 4 and 6 indicating the number of the Si and C bilayers needed to form the hexagonal lattice while H indicates the hexagonal structure [29]. These structures are shown in Figure 2.9. SiC can be either grown as a bulk material or epitaxially on either a hexagonal substrate (4H- and 6H-SiC) or on a Si substrate (3C-SiC only).

SiC is a wide bandgap semiconductor. Each polytype of SiC has a different energy bandgap. 3C-SiC has slightly lower bandgap of 2.29 eV at temperature of 300 K, comparing to 4H- and 6H-SiC with 3.2 eV and 3.00 eV, respectively. For comparison Si has an energy bandgap of 1.12 eV at 300 K. This higher energy bandgap of SiC has made them a suitable choice for high power and high temperature operations. Due to this higher energy bandgap, SiC significantly lower

thermal ionization of electrons for high temperature and power operations while this is a main issue in Si technology [92]. In addition, SiC polytypes have higher thermal conductivity in comparison with Si. The thermal conductivity of SiC is 3.6-3.7 *W/cm K* depending on the polytype while for Si this value is 1.49 *W/cm K*.

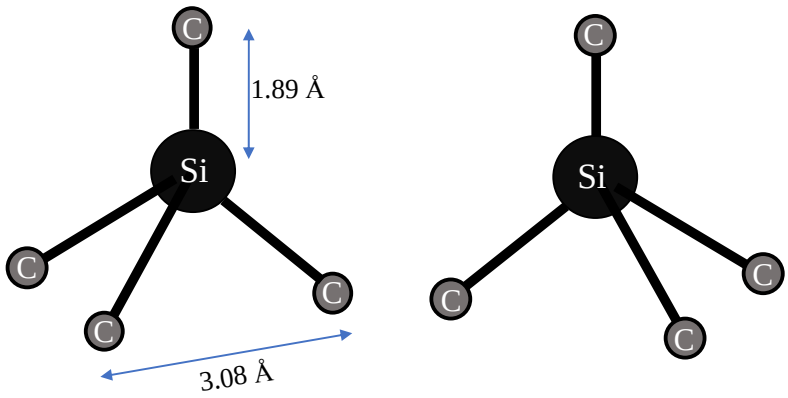

Figure 2.8. Si-C tetrahedron bonding in silicon carbide (SiC) crystals. Due to the short length covalent bonding between Si and C atom, SiC molecules have high chemical and mechanical stability [92].

SiC films have been historically produced using various epitaxial growth methods. Liquid phase epitaxy (LPE) was first introduced in 1980s to grow 6H-SiC [93]. Hetero-epitaxial growth of cubic silicon carbide (3C-SiC) was introduced later in 1980s using chemical vapor deposition (CVD). CVD epitaxial growth of 3C-SiC produced a very poor quality 3C-SiC, whose electrical properties were far below theoretical expectations. Later, homo-epitaxial growth of 6H-SiC via CVD resulted in very pure, good quality SiC. Hence homoepitaxy, via cold-wall CVD and later (1990's) hot-wall CVD, became the standard for producing good quality 6H-SiC with near theoretical electrical properties [94].

SiC materials can be doped during bulk and epitaxial growth processes. n-type doping is simply formed by introducing nitrogen (N_2) gas during the growth process. Also, N_2 gas can be

diluted by adding Ar gas during the process. The doping density of N_2 atoms in SiC crystals can be increased to form an n-type SiC crystal with lower resistivity. The common doping density of nitrogen atoms for commercial processes varies between 1.5×10^{16} to 6×10^{18} cm^{-3}, in order to form low resistivity SiC (0.015-0.025 Ω.cm). In an epitaxial growth process, when the temperature and the pressure inside the growth chamber is fixed, the C/Si ratio and the flow rate of N_2 are the two parameters that control the intentional doping density [77].

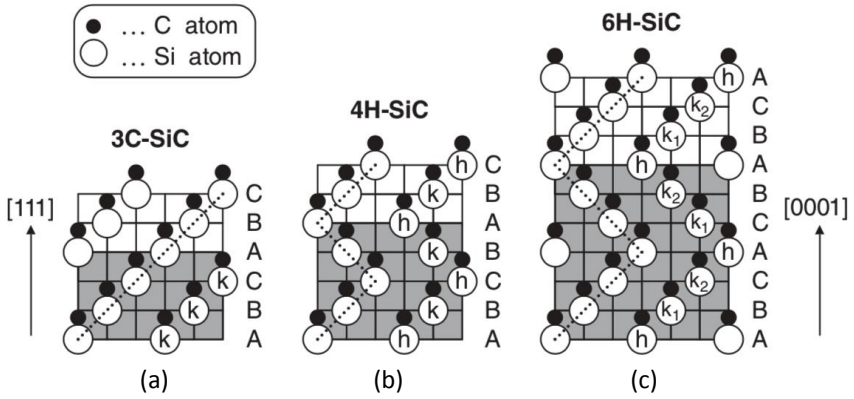

Figure 2.9. Schematic of stacking sequence of SiC polytypes. (a) cubic silicon carbide (3C-SiC) polytype, with 3 indicating three bilayers of SiC and C indicating cubic crystalline. (b) Hexagonal polytypes of silicon carbide (4H-SiC) and (c) (6H-SiC), with 4 and 6 indicating the number of the bilayers and H indicating the hexagonal structure [77]. Taken from [77] with permission from John Wiley and sons.

There are two principal p-type dopants in SiC growth: boron (B) and aluminum (Al). Aluminum is preferred as the acceptor energy level is significantly shallower than for B acceptors. Thus p-type doping in SiC is done through adding trimethylaluminum (TMA: $Al(CH_3)_3$) to the SiC material during the epitaxial growth in CVD. p-type doping efficiency using TMA is higher when the TMA is introduced on the Si face. This can be explained using the site competition doping model [95] whereby Al atoms compete for Si lattice sites during growth. On the Si face, the acceptor density is increasing linearly with TMA flow in the gas phase, simply because TMA

increases the C/Si ratio by reducing the net Si concentration in the film [77]. The range of Al doping during this process can vary between 2×10^{14} and 5×10^{20} cm^{-3}. Heavily doped p-type SiC is possible only on the Si face due to the reason mentioned earlier and also because increasing TMA supply on the C face can lead to a rough surface [96]. In addition to Al, the other materials that can be used as p-type dopants in SiC doping are boron (B) and gallium (Ga). However, these two dopants may lead to high resistivity SiC films [77]. The doping range in p-type doing of SiC can be expanded by controlling the ratio of C/Si. Given a fast transition between p-type and n-type doping in SiC is required, one needs to control the C/Si ratio.

2.3 Magnetic Resonance Imaging

Throughout this section the physics involved in magnetic resonance imaging (MRI) is discussed. The basic principles that are fundamental in creating MRI images are covered. Spin physics, which defines how dipoles and their alignments under a magnetic field are involved in formation of MRI scans, is explained and nuclear magnetic resonance (NMR) spectroscopy is discussed. Then, MRI imaging principles, similarities and differences are defined and some of the imaging techniques utilized throughout this work are explained. Thereafter, an overview of MRI hardware is provided and a connection between the MRI physics and hardware made. This is followed by a discussion of safety concerns to the patient during MRI scans. MRI artifacts, another critical phenomenon defining the quality and usability of MRI scans, and their cause and severity will be explained. Finally, radio frequency (RF) coils, critical in formation of MRI images and also the cause of safety issue regarding MRI induced heat, is explained.

2.3.1 Introduction

MRI is a tomographic medical imaging technique that creates high quality images from organs and soft tissue and is used as an important diagnostic technique. It is used in the study of numerous disorders and problems within the human body such as neurological disorders, cardiovascular issues, as well as the diagnosis of cancers and tumors and determining its stage of development [97], [98]. Its benefit has also been proven in mapping to aide in the placement of deep-brain stimulation (DBS) leads in the brain [99].

MRI works based on the principles of nuclear magnetic resonance (NMR). NMR is based upon the fact that most atomic nuclei spin and, consequently, have a property called magnetic momentum. The frequency of this spin is determined by the external magnetic field that is applied to the nuclei. The energy transferred to the nuclei occurs at the spin frequency of the specific nuclei. These nuclei can emit energy at the same frequency that they absorb it, when the electromagnetic field that changed the momentum is removed. By collecting this emitted energy and analyzing their temporal and spatial information, very useful information regarding the structure of a specific group of nuclei is achieved [100]. Using this concept, MRI can make high quality images from different virtual depth slices of the body. Each slice in the MRI scan is formed out of volume elements called the voxel. The images taken in MRI are composed of pixels and the contrast of each pixel is proportional to the signal intensity received from each voxel that these images are built from.

The human body contains mostly water and fat. Fat and water have hydrogen atoms in their structure and, since hydrogen atoms have a nuclei that emits NMR signals, hydrogen nuclei are therefore a perfect candidate for making MRI images [52].

One of the benefits that MRI has over other medical imaging techniques such as X-Rays is that it does not contain any ionizing radiation and thus, in principle, does not harm the human body directly. Instead, MRI images from the body are based upon the interaction between a static magnetic field (**B_0**), a low frequency time domain gradient magnetic field (**dB/dx**), and a high frequency electromagnetic field (**B_1**). This benefit, and also the benefit of building images from soft tissue, have made MRI a very popular and common diagnostic tool in a medical field.

2.3.2 Spin Physics

Spin is an intrinsic property of subatomic particles. All electrons orbiting the atom's nucleus, as well as the protons and neutrons inside the nucleus, have spin properties or, in other words, display intrinsic angular momentum. A detailed explanation of the physics involved requires Quantum Mechanics, but it is sufficient for this dissertation to review the basics without delving into the detailed physics at the quantum level. Each of these protons, neutrons and electrons that are unpaired has a spin of ½. On the other hand, particles that have opposite spins can pair up and cancel each other's spin resulting zero net spin. Here is an example of this. There are certain conditions that should be considered when calculating the spin of the nucleus. Therefore, the rule of thumb is when both numbers of protons and neutrons are even, then the spin is zero. If the number of protons plus the number of neutrons is even, then the value of spin is half integers (i.e. ½, 3/2, 5/2, etc.). And finally, if the number of neutrons and number of protons are both odd, then the spin is a full integer (i.e. 1, 2, 3, etc.) [101]. In MRI those nuclei that possess an unpaired spin particle are important and are considered in MRI imaging. Hydrogen, with a single proton and neutron, falls into the full integer spin category which implies that the sensitivity in using atomic spin to form an MRI is optimum.

In a static magnetic field B_0 with intensity in Tesla (T), a nucleus that has a non-zero spin can absorb a photon of energy with the frequency of $\boldsymbol{\nu}$. This frequency ($\boldsymbol{\nu}$), also called Larmor frequency, depends on the gyromagnetic ratio ($\boldsymbol{\gamma}$) of the nucleus and the intensity of the magnetic field [52], using the following equation:

$$\boldsymbol{\nu = \gamma B_0} \qquad \textit{(Equation 2.5)}$$

The gyromagnetic ratio for hydrogen atoms is 42.58 MHz/T. For example, the Larmor frequency for hydrogen in a static magnetic field of 7 T is equal to ~298 MHz.

Protons inside the nucleus possess spin and this spin acts like a magnetic moment vector. In the presence of an external magnetic field, protons either line up in the direction of the magnetic field or in the opposite direction depending on the energy states that they are at. If a proton is in a lower energy state, when it is given a photon of energy exactly the same amount as the difference between two energy states, it moves to the higher energy state. This is shown in Figure 2.10. The amount of this photon of energy ($\boldsymbol{E}$) depends on the frequency of the spin, and is calculated using the following equation:

$$\boldsymbol{E = h\,\nu} \qquad \textit{(Equation 2.6)}$$

In Equation 2.6, E is the photon of energy given to a proton to change its energy state, $\boldsymbol{h}$ is Planck's constant ($h = 6.626 \times 10^{-34}$ J s) and $\boldsymbol{\nu}$ is the frequency of the spin [102].

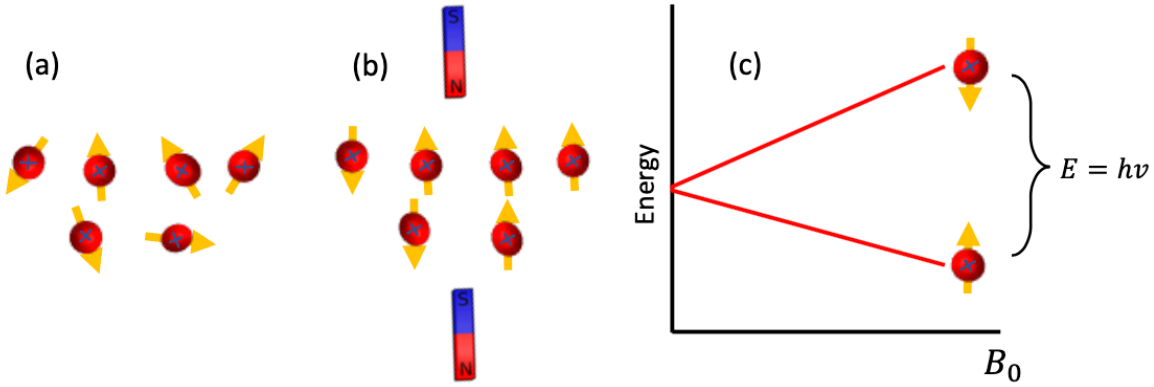

Figure 2.10. Spin moment vectors and energy states of spinning protons. (a) Magnetic moments of protons in the absence of a magnetic field. (b) Proton Magnetic moments in the presence of an external magnetic field. Protons in high energy states line up in the opposite direction of the magnetic field, and protons in low energy states line up in the direction of the magnetic field. (c) Energy states of the spinning protons and the difference between energy states given to the proton at the lower energy state to jump to the higher energy state.

At room temperature, the number of the protons that are in low energy states is slightly higher than those in high energy states. When incident photons transfer their energy to the lower state protons, these protons jump to the higher energy state. At the moment that the source of energy is removed, these excited protons relax back to the lower state and lose the absorbed energy in the process via conservation of energy. The extra energy is emitted at the same frequency as the incident photon. The amount of the energy is directly correlated to the population difference between low and high energy state protons. Because MRI spectroscopy is capable of sensing this slight difference in energy population, it is a very sensitive and accurate spectroscopy method [52].

2.3.3 Spin-Lattice Relaxation and Precession

At equilibrium, when the system is exposed to a $\mathbf{B_0}$ magnetic field, the net magnetization ($\mathbf{M_0}$) is in the direction of the $\mathbf{B_0}$. When packets of photons impinge on the protons, the net magnetization may change to yield a new magnetization vector ($\mathbf{M_z}$), which is along the same axis

as $\mathbf{B_0}$. When the source of energy (packets of photons) is removed, then $\mathbf{M_z}$ relaxes back to equilibrium in an exponential time frame, with the time constant of T_1, as per the following equation:

$$\boldsymbol{M_z} = \boldsymbol{M_0}\left(1 - 2e^{-t/T_1}\right) \qquad \textit{(Equation 2.7)}$$

In Equation 2.7, the T_1 constant is called the spin-lattice relaxation time, and is defined as the time to decrease the difference between two components of longitudinal magnetization, $\mathbf{M_z}$ and $\mathbf{M_0}$, by a factor of *e* [103].

When the net magnetization is placed on the XY plane instead of the Z axis, which is the spin axis, the magnetic moment vector rotates around the Z axis. The rotation of this magnetic moment around the Z axis is called precession, as illustrated in Figure 2.11 [52].

2.3.4 Spin-Spin Relaxation

As mentioned in Section 2.3.3, the magnetization vector is not only limited to the longitudinal magnetization ($\mathbf{M_z}$), but also there is a transverse magnetization vector ($\mathbf{M_{XY}}$) that is the product of precession about the Z axis. By injecting photon packets into the sample, the components of the transverse magnetization vector may start to diphase each other, due to slightly different Larmor frequencies. After removing the source of energy, the transverse components of the transverse magnetization vector start lining up their phases and relaxed back to the equilibrium condition ($\mathbf{M_{XY0}}$). The constant characterizing the time that it takes for the transverse magnetization vectors to rephase and lose the absorbed energy, and thus return to the equilibrium transverse magnetization, is called spin-spin relaxation time or T_2. The dephased transverse magnetization and the equilibrium transverse magnetization is related through the following equation [104]:

$$\boldsymbol{M_{XY}} = \boldsymbol{M_{XY0}}\left(e^{-t/T_2}\right) \qquad \textit{(Equation 2.8)}$$

In an XYZ coordinate system, if a pulsed alternating magnetic field ($\mathbf{B_1}$) at the Larmor frequency rotates about the Z axis for a specific duration known as τ, it can change the phase of the magnetization vector according to the following equation:

$$\theta = 2\pi\,\gamma\,\tau\,B_1 \qquad \textit{(Equation 2.9)}$$

where θ is the phase of the magnetization vector, γ is the gyromagnetic ratio, τ is the pulse duration, and B_1 is the intensity of the alternating magnetic field.

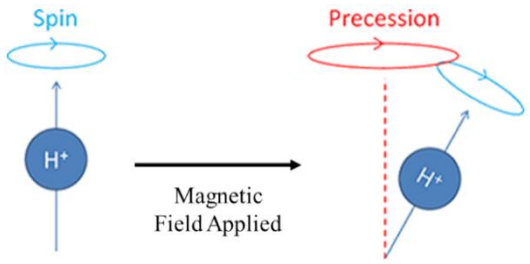

Figure 2.11. The magnetic moment vector rotates around the Z axis. The rotation of this magnetic moment around the Z axis is called precession.

2.3.5 MRI Sequences

- *The 90-FID Sequence*

In a 90º free induction decay (FID) pulse sequence, by applying a rotating RF signal the magnetization vector turns 90º from the longitudinal direction to the X'Y' plane and rotates about the Z axis. Then the magnetization vector starts decaying over time. X'Y' axes are rotating XY axes at the Larmor frequency (Figure 2.12). This convention is used in order to simplify the mathematical models. This sequence may be repeated multiple times to improve the signal quality or signal to noise ratio (SNR). The amplitude of the receiving signal depends on the spin-lattice

relaxation time (T_1) and the gap time between the repetitions (TR). The amplitude of the signal in the 90-FID sequence is calculated using the following equation:

$$S = k\rho\left(1 - e^{-TR/T_1}\right) \qquad \textit{(Equation 2.10)}$$

where S is the amplitude of the signal, k is a proportionality constant, and ρ is the spin density [52].

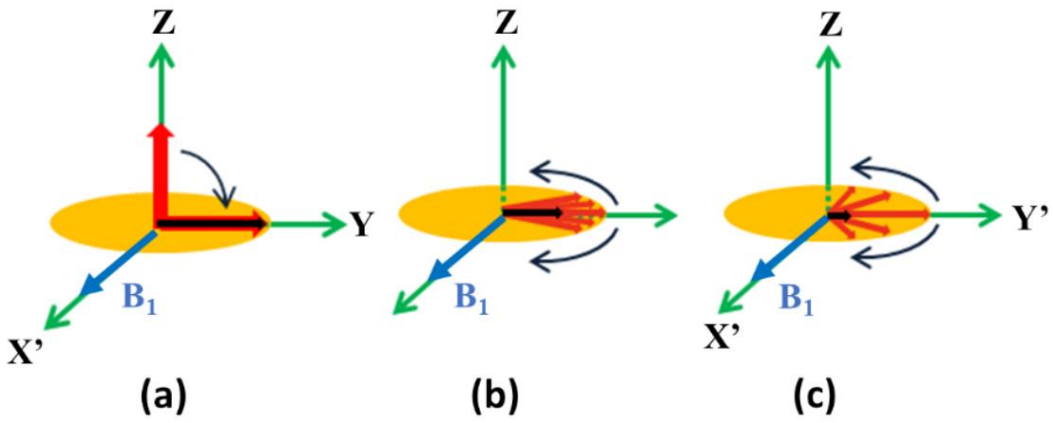

Figure 2.12. 90º free induction decay (FID) pulse sequence. (a) By applying B_1 the magnetization vector turns 90º from the longitudinal direction to (b) the X'Y' plane and rotates about the Z axis. (c) Then the magnetization vector starts decaying over time.

- *Conventional and Fast Spin-Echo Sequences*

In a conventional spin-echo sequence, first a 90º pulse signal is applied. This causes the longitudinal magnetization to fall on the X'Y' plane and starts decaying. Now, the transverse magnetization vector starts rotating about the Z axis and starts dephasing. At this point a 180º pulse is applied that shifts the transverse magnetization 180º and, as a result, the vector partially rephases. This creates another decaying signal called an echo. Another type of spin-echo sequence is the fast spin echo sequence in which, after 90º pulse multiples 180 º pulses are applied. These two are illustrated in Figure 2.13. The maximum amplitude of the received signal depends on the

repetition time (TR), echo time (TE) which is the duration between the 90º pulses, and is calculated via the following equation [105]:,

$$S = k\rho\left(1 - e^{-TR/T_1}\right)e^{-TE/T_2} \qquad \textit{(Equation 2.10)}$$

Equation 2.10 is valid when TR >> TE.

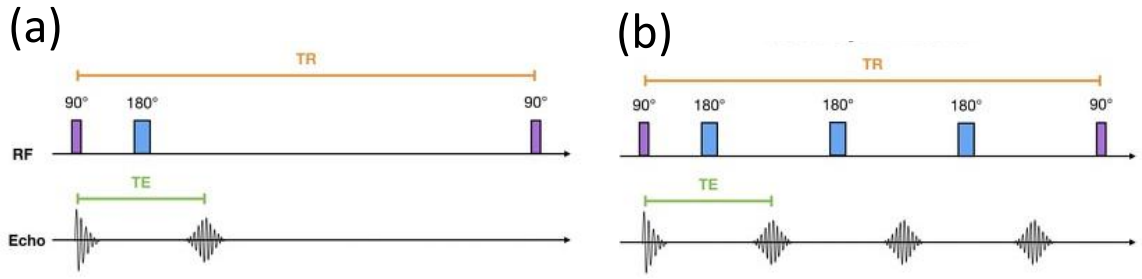

Figure 2.13. Spin echo sequences during MRI operation. (a) The conventional spin-echo sequence, first a 90º pulse signal is applied. This causes the longitudinal magnetization to fall on the X'Y' plane and starts decaying. Now, the transverse magnetization vector starts rotating about the Z axis and starts dephasing. At this point a 180º pulse is applied that shifts the transverse magnetization 180º and, as a result, the vector partially rephases. (b) In the Fast spin-echo sequence, multiple 180º pulses are applied before the next repletion begins.

2.3.6 MR Image Localization

As mentioned in the previous sections, MRI works based on the spin physics for hydrogen atoms that exist in body tissue. As most of the human body is composed of water and fat, and since both water and fat contain hydrogen, these two elements can be used to construct MRI images. However, since the Larmor frequency for all hydrogen atoms in different body parts are similar given a constant static magnetic field $\mathbf{B_0}$ is applied throughout the body, taking localized images from a specific virtual slice of the body seems impossible. In order to be able to form localized images from a targeted body slice, a gradient magnetic field can be introduced to the system. This

means $\mathbf{B_0}$ is no longer a constant value all over the subject, rather a variation in the static magnetic field may be defined in all directions [106]. These gradient magnetic fields are denoted G_X, G_Y, and G_Z, indicating the gradient fields in the X, Y and Z directions.

The center of the magnet where (x,y,z) = (0,0,0) is called the MRI isocenter and has a static magnetic field equal to $\mathbf{B_0}$. The intensity of the static magnetic field in another section inside the MRI depends on the location and hence the Larmor frequency in different locations varies slightly. Therefore, the Larmor frequency for each position, given that the gradient is in the X direction, is encoded using the following equations [52]:

$$v = \gamma(xG_x + B_0) = \gamma x G_x + v_0 \qquad \textit{(Equation 2.11)}$$

Thus 'virtual' tissue slices may be formed within tissue to allow for depth localization of the MRI signal so as to form 3D images of the human body.

2.3.7 Back Projection Imaging Technique

In order to select a virtual slice to form an MRI image, a 90º pulsed RF signal with a gradient magnetic field in the direction of the slice should be applied to the subject. The RF signal is companied with a 90º pulse in order to flip the spins at 90º. Selection of a targeted slice can be done through encoding of the localized signals.

One of the issues with pulsed signals in MRI is that the Fourier Transform of a pulse is a sinc function which consists of a range of signals with various amplitudes in the frequency domain. Therefore, the neighboring slices can be also affected. This results in the other slices being rotated slightly and reduces the quality of the image. This is shown in Figure 2.14 (a). One solution to this issue is to use a sinc pulse signal instead of a rectangular pulse. The Fourier Transfer of a sinc signal is a simple square pulse, therefore a narrow range of frequency can be chosen using this

method. The time-domain and the frequency domain of the 90º RF signal, as well as the signals needed to construct an image of the targeted slice, is shown in Figure 2.14 (b,c) [52].

2.3.8 MRI Hardware

An MRI machine mainly consists of a central tube, call the bore, with DC field magnets and RF coils inside, and a controlling section encompassing a computer, as well as signal amplifiers and generators for the manipulation of the various magnetic fields generated inside the MRI. The bore itself consists of a powerful static magnet that generates B_0, three different gradient magnets generating B_0 gradients in X, Y and Z, and finally an RF coil that generates the RF signal. This is illustrated in Figure 2.15.

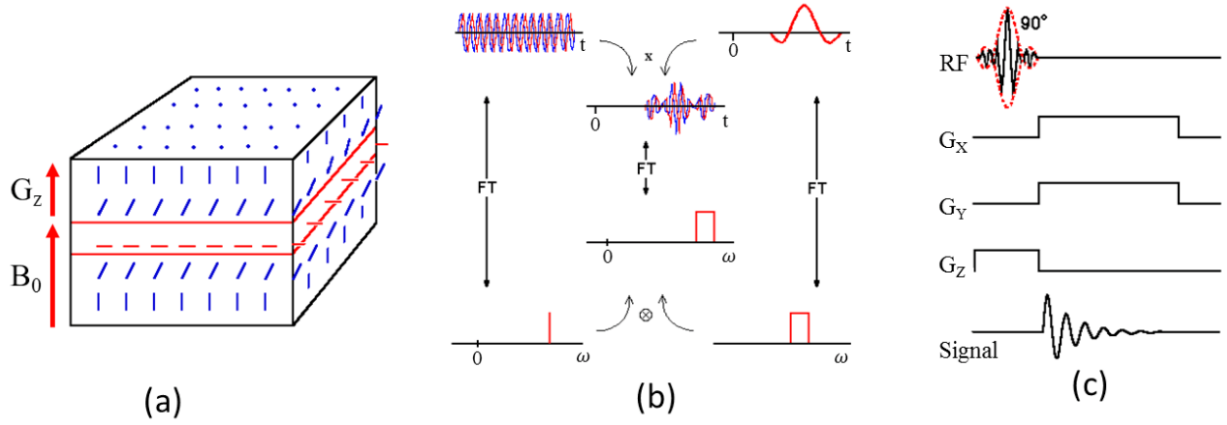

Figure 2.14. Localized images in MRI. (a) Magnetic moments (blue and red arrows) during application of a rectangular RF signal pulse. Slice and signal localization is poor and the nuclei in other parts of the subject may be rotated slightly resulting in low-quality images. (b) A sinc pulse used instead of a rectangular pulse. The resulting signal in the frequency is rectangular pulse that can specifically target a thin slice. (c) An FID-90 sequence with RF signal applied with a 90º sinc pulse. First the Z gradient is active to choose a targeted slice while the RF signal is active to rotate the spin of the nuclei inside the slice. Then, the X and Y gradients are activated to encode the image and localize each voxel [52]. Reprinted from [52] with permission from Joseph Hornak, Ph.D., via email.

- *Static Magnet*

The magnet is a coil of superconducting wire that is placed inside a helium container to keep the temperature near absolute zero (0K). By keeping the temperature of the superconducting wire close to zero, and flowing current inside the coil, the coil keeps the current flowing as long as it is kept inside the helium. Another buffer may be needed to cover the helium container, that acts as a thermal buffer between the liquid helium and the room temperature. In the early designs, liquid nitrogen (77K) was used for this purpose. In later designs with stronger static B_0 fields liquid nitrogen was replaced with a helium cryocooler [52].

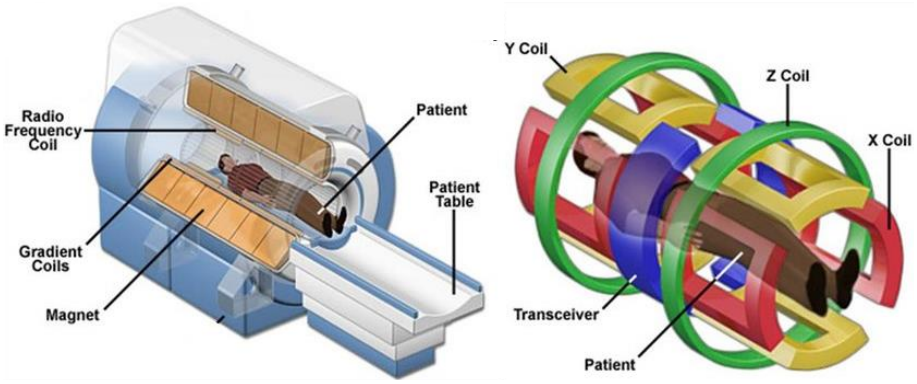

Figure 2.15. Various coils and magnets inside an MRI bore (i.e., where the patient is placed during MRI analysis as shown) that generate B_0, the gradient fields and RF signal. Both human (shown) and animal bore (not shown) have been developed, the later to facilitate animal studies but at lower cost due to the smaller size of the system. Public domain taken from [107].

- *Gradient Coils*

The gradient coils are used to add variation to the $\mathbf{B_0}$ field in all vector (i.e., X, Y and Z) directions. To understand how this works first consider that the MRI has a horizontal superconducting magnet that establishes $\mathbf{B_0}$ in the Z direction. In order to add a gradient to the $\mathbf{B_0}$

in this direction, a pair of antihelmholtz coils are used. An antihelmholtz coil is shown in Figure 2.16 (a). In this pair of coils, each coil generates a magnetic field in the opposite direction of the other coil. As a result of this coil combination, vector sum of the two magnetic fields is zero at the center of the bore and becomes negative or positive elsewhere depending on the proximity to the coil generating the magnetic field gradient at that point in space. In addition, there are gradient magnetic fields in the X and Y directions. In order to generate these gradients in X and Y another combination of coils is chosen as illustrated in Figure 2.16 (b,c). This coil combination allows for a gradient magnetic field in the X-Y plane throughout the Z axis direction [108].

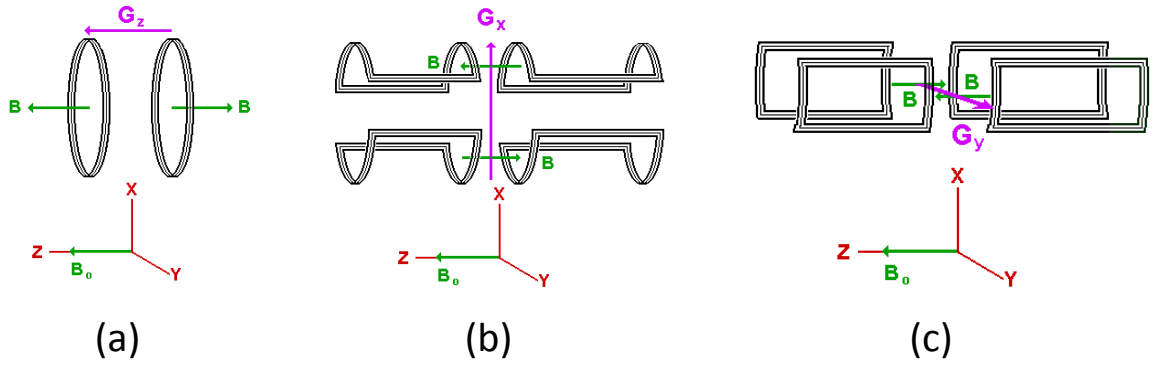

Figure 2.16. MRI gradient coils used to impose a magnetic field gradient $\mathbf{G}_{XYZ}$ on $\mathbf{B}_0$. (a) Antihelmholtz coil pair to generate a gradient in $\mathbf{B}_0$ in the Z direction. Coils used to generate a gradient in the (b) X and (c) Y directions [52]. Reprinted from [52] with permission from Joseph Hornak, Ph.D., via email.

- *RF Coils*

RF coils are used in MR imaging to generate the $\mathbf{B}_1$ magnetic field. $\mathbf{B}_1$ causes the magnetization vector to rotate. In order for the net magnetization to rotate, packets of energy must be absorbed by hydrogen nuclei at the Larmor frequency. Therefore, RF coils are, in fact, resonator coils that resonate at the Larmor frequency. The RF coils are categorized into three different groups: transmit only, receive only and transmit-receive. One of these coils, or a combination of

them, may be required for scans from different body parts. In addition, surface coils and volume coils are available to be utilized in certain conditions that will be explained in the following sections [109].

Not only must the RF coils accurately resonate at the Larmor frequency, but they must generate a homogeneous $\mathbf{B_1}$ inside a certain volume. This homogeneity is required mainly because even a tiny offset in $\mathbf{B_1}$ intensity causes the net magnetization to rotate at a different angle and, as a result, emits a different amount of energy [110]. Thus, the RF receiver receives distinct energy values from similar hydrogen atoms which are piled up to create a tissue slice image. Consequently, the image quality and contrast drop if there is even the slightest offset in $\mathbf{B_1}$.

Although not as homogeneous as the volume coils, a surface coil can be used for irregular shaped subjects or in cases when an image from certain areas of the subject is required that cannot fit inside a whole-body coil (bore). In addition, surface coils may create lower SAR and higher SNR in their proximity while the RF signal drops considerably when the distance is higher than the diameter of the surface coil [111].

The MRI compatibility of the 3C-SiC intracortical implant is at the center of focus of the current work, thus a volume coil is more favorable when it comes to large cross-section brain images. As a consequence, the next section focuses on the technical details of volume RF coils, specifically birdcage coils which are one of the most common coils used in whole-body and brain imaging.

2.3.9 Birdcage Volume Coil Resonator

As its name indicates, birdcage coils are cylindrical coils with a birdcage-shaped structure that resonates at the Larmor frequency. They are built from vertical legs or rungs placed around a

cylinder with a similar gap between them. These rungs are attached to two rings at both ends of the cylinder. Birdcage coils generate a highly homogeneous transverse circularly polarized magnetic field ($\mathbf{B_1}$) within the cylinder. When an electrical current at the Larmor frequency of interest flows through each of the rungs in a different phase, this generates a circularly polarized magnetic field within the coil at the Larmor frequency. The end-rings form loops by connecting the rungs together and, therefore, they flow more electrical current. As a consequence, they are physically wider than the rungs.

The placement of the rungs, the phase difference between the rungs, the diameter of the coil and its length are the factors determining the homogeneity of $\mathbf{B_1}$ in a birdcage coil [112]. All of these factors are highly correlated and a slight change in one may improve one of the coil specifications while deteriorating the other ones. For instance, while increasing the ratio of the length to the diameter one can improve the $\mathbf{B_1}$ uniformity and homogeneity, however this reduces the SNR. An optimum value may be selected for each of these factors depending on the case(s) that the coil is to be used for.

The circuit model of an N-rung birdcage resonator consists of a network of RLC lumped elements containing N meshes. Ideally, the rung resistance is very low so that it can be neglected to simplify analysis of the birdcage lumped circuit. Figure 2.17 illustrates a birdcage resonator and its lumped element model. This specific configuration containing capacitors at both the rungs and the end-rings and is called the hybrid or band-pass configuration. Depending on the location of the capacitors in a birdcage resonator, it may form a low-pass, band-pass or high-pass configuration. A high-pass birdcage has capacitors only at the end rings while a low-pass birdcage has capacitors only at the rungs [109].

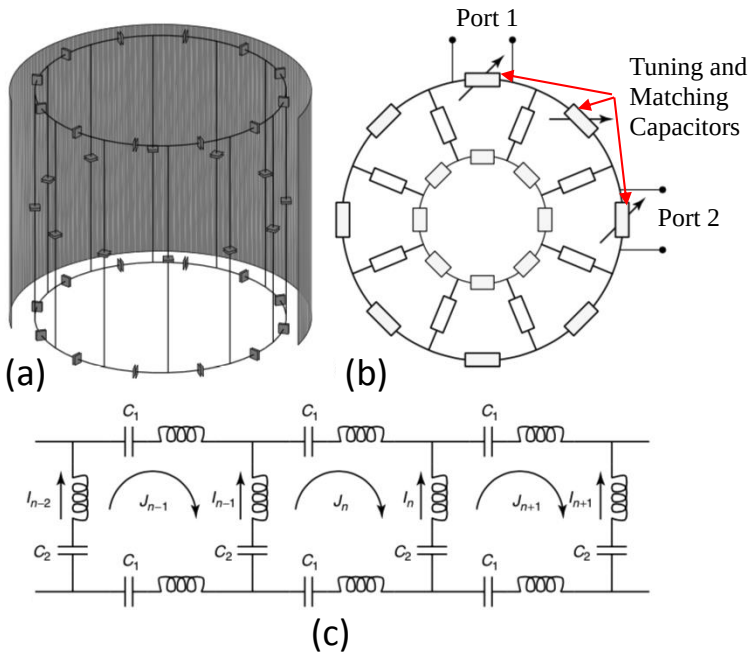

Figure 2.17. A hybrid or band-pass birdcage resonator. (a) Depiction of a birdcage coil consisting of vertical legs or rungs connected to two end-rings. The capacitors (small squares in the figure) in this specific configuration are placed on both the rungs and the end-rings. A metallic shield is placed around the coil that acts as a signal ground. It also reduces the coupling effect with the other coils (i.e. gradient coils) within the MRI bore, as well as reducing outside noise. (b) This image shows a top view of a two-port coil with tuning and matching capacitors. (c) Schematic of a section of the lumped-element network of a band-pass coil containing wire and coupling inductors, and rung and end-ring capacitors. The current of each rung and the mesh current density J_N are shown in this circuit for reference [109]. Reprinted from [109] with permission from John Wiley and Sons.

A birdcage resonator may have a metallic shield that acts as a ground for the high frequency signal flowing inside the rungs and the rings. This metallic shield can also reduce the electromagnetic coupling with the other magnetic sources inside and outside of the MRI bore. In addition, birdcage coils may include tuning and matching capacitors at certain locations on the coil to tune and match the RF signal.

One of the factors that defines the image quality when a specific birdcage coil is used is the sensitivity of the coil. The sensitivity of a birdcage coil is defined as the ratio between the

amplitude of $\mathbf{B_1}$ at a certain location inside the coil and the square root of the power given to the ports. The highest sensitivity is obtained when the ratio between the coil length and diameter is approximately $\sqrt{2}$ for an unshielded coil and less for a shielded coil. This factor, together with the coil SNR, are critical factors that define the usability of a birdcage coil for a certain MR imaging case [113].

One of the important considerations in designing a birdcage coil is the topology of the birdcage coil including low-pass, band-pass and high-pass topologies. These factors include (but are not limited to) frequency of operation, the length of the coil, sensitivity to load, SAR, and port connections.

- *Frequency of Operation*

Low-pass birdcage coils have lower capacitor values than high-pass coils. Larger capacitors are usually more lossy and preferred at higher frequencies. For this reason, low-pass birdcage coils are preferred to be used in lower frequencies while high-pass coils are used in higher frequencies.

- *Coil Length*

In order to keep the SNR at an acceptable level, which is another important criterion, the length of the coil must be less than $\lambda/20$ where λ is the Larmor frequency wavelength. If a birdcage coil needs to be longer than $\lambda/20$, the rungs can be split into sections by adding capacitors between them. Therefore, a hybrid, or band-pass, coil is a more convenient choice for longer coils [113].

- *Sensitivity to Load*

In order to reduce the sensitivity to lossy loads in birdcage coils, a hybrid or band-pass topology may be a better choice. The resonance frequency may slightly shift when a lossy load is introduced to a birdcage coil. By introducing a lossy load, the resonance frequency may decrease

in low-pass coils while it increases in high-pass coils. By controlling the ratio between the rung capacitors and the end-ring capacitors in a band-pass topology, the sensitivity to a lossy load can be reduced [109].

- *Specific Absorption Rate (SAR)*

SAR is a safety concern in MR imaging. This value needs to be kept below a certain standard level when a subject undergoes MRI scans. SAR distribution may completely change depending on the selected topology and the load. Therefore, the topology may be chosen depending on the importance of the SAR present during operation and the geometrical specifications of the subject.

- *Port Connections*

In a low-pass birdcage coil, ports are usually connected to the middle of the coil while in a high-pass coil they are connected to the ends of the coil. In a hybrid topology they can be connected to either of the middle or the ends [109].

In order to generate a uniform, homogeneous circularly polarized $\mathbf{B_1}$ in the birdcage coil, each of the rungs should be fed by an RF power level at a certain phase. While feeding all of the rungs using an individual port is inconvenient, the network of capacitors together with the wire inductance form the necessary phase difference between rungs. In order to initiate this circularly polarized RF signal, one common approach is to use a quadrature port configuration. In this configuration, the RF power is coupled to the two linearly polarized ports with a 90º phase difference. These two ports are placed 90º apart around the coil. Using this approach and a suitable combination of capacitors, a circularly polarized $\mathbf{B_1}$ is generated in the birdcage coil.

Isolation between the two quadrature ports, as well as matching and tuning them, are also critical parameters that define the quality of the produced images in an MRI scan as well as the overall power consumption of the system.

- *Port Isolation*

Isolation between two ports can always be improved by adding capacitors to the network to compensate for any asymmetries in the coil construction. Usually isolation capacitors are placed at 45º, 135º or 225º around the coil. Port isolation is generally improved if the lumped components are more accurate so that the difference in their values is negligible [109].

- *Matching and Tuning*

In order to match the impedance of the ports and the power lines to reduce reflected power, a matching circuit is utilized. Several matching circuits have been introduced in the literature that can be used for various birdcage coils configurations [109], [114]. When a birdcage coil is loaded with various lossy loads, the resonance frequency of the coil may be slightly shifted. To compensate for this resonance frequency shift tuning capacitors are typically used. Tuning is done by adding variable capacitors in parallel to the capacitors placed at the ports. The value of the tuning capacitors should be kept below 8% of the port capacitors in order to maintain homogeneity of the magnetic field inside the coil [115].

2.3.10 MRI Safety

Patient safety when undergoing MRI scans, specifically those patients with metallic implants, has been always a concern [116]. The implant's metallic parts can interact with the magnetic fields inside the MRI resulting in implant heating or induced torque. The resulting implant displacement may damage the surrounding tissue and consequently cause serious injuries

to the patient. In order to avoid these disastrous situations several standard procedures and tests have been defined to examine implant safety during MRI operation [56], [117], [118]. In this section, the implant's conductive parts interaction with gradient magnetic fields, RF fields and static magnetic fields are studied, and the nature of each interaction elaborated.

A. RF Field and Induced Heat

The RF coils basically consists of either a transmitter or receiver, or both transmitter and the receiver as discussed in the previous sections. The RF fields ($\mathbf{B_1}$) are applied perpendicular to the static field $\mathbf{B_0}$ at the Larmor frequency of interest.

The induced electric field ($\mathbf{E_i}$) can be calculated using the incident electric field ($\mathbf{E_0}$) radiated by the RF coils. Then, using a reaction integral on the conductive parts of the implant, the induced current can be calculated. The incident electric field and the induced electric field are determined by Equation 2.12 and 2.13, respectively [119]:

$$\boldsymbol{E}_0 = -j\omega\boldsymbol{A}(r) + \frac{\nabla(\nabla.\boldsymbol{A}(r))}{j\omega\varepsilon\mu} \qquad \textit{(Equation 2.12)}$$

$$\boldsymbol{E_i} = -\boldsymbol{E}_0.\hat{z} \qquad \textit{(Equation 2.13)}$$

where $\boldsymbol{A}$ is the magnetic vector potential, ε and μ are the medium permittivity and magnetic permeability, respectively. The deposited power, which is expressed by the specific absorption rate, SAR (*W/Kg*) [109], is calculated via Equation 2.14:

$$SAR = \frac{\sigma \boldsymbol{E}^2}{\rho} \qquad \textit{(Equation 2.14)}$$

where σ is the electric conductivity and ρ is the mass density.

The heat transferred from the surface of the conductor to the surrounding tissue is obtained by the heat transfer equation for a non-perfused material with an internal heat source [56], as indicated by Equation 2.15:

$$\rho c_p \frac{d\boldsymbol{T}}{dt} = \nabla.(k\nabla\boldsymbol{T}) + SAR\rho \qquad \textit{(Equation 2.15)}$$

where ρ is the density of material, c_p is the specific heat, $\boldsymbol{T} = \boldsymbol{T}(r, z, t)$ is the temperature function (℃) and k is the thermal conductivity (*W/m-K*) with K temperature in Kelvin.

B. Gradient Magnetic Field and Induced Heat

The use of a gradient magnetic field creates a spatial variation in the static magnetic field profile by adding a field gradient to $\mathbf{B_0}$. The intensity of the gradient magnetic field is given by d$\boldsymbol{B}$/dx in T/m. Early MRI systems could generate gradient magnetic fields with a maximum strength d$\boldsymbol{B}$/dt = 100 mT/m [52]. The gradient coils are usually specified by their switching rate in T/s.

The time-varying magnetic field with the switching frequency of *f* can be modeled using a sine function as shown in Equation 2.16:

$$\boldsymbol{B} = |B|\sin(2\pi f t) \qquad \textit{(Equation 2.16)}$$

$\boldsymbol{B}$ is the magnetic field vector which is time dependent and has a direction in space and $|B|$ is the amplitude, or intensity, of the magnetic field. Considering that d$\boldsymbol{B}$/dt is the switching rate, we can find the intensity of the magnetic field in the initial time using Equation 2.17:

$$|B| = \frac{d\boldsymbol{B}}{dt}\,\frac{1}{2\pi f} \qquad \textit{(Equation 2.17)}$$

As this magnetic field is time varying, it can induce an electric field in the conductive parts of the neural probes according to the Maxwell-Faraday equation, shown in Equation 2.18:

$$\oint \boldsymbol{E}.dl = -\frac{\partial}{\partial t}\iint_{s} \boldsymbol{B}.ds \qquad \textit{(Equation 2.18)}$$

The result of this induced electric field is an Eddy current which flows in the conductive parts of the probe. This current results in joule heating, also referred to as Ohmic heating, where $P \propto I^2R$, *Watts*. This explains the basic mechanism behind MRI-induced heating in implants.

C. Static Magnetic Field

In addition to induced joule heating in implants, the static field $\boldsymbol{B}_0$ can induce a torque on the implanted neural probe. The induced current generated by the gradient fields can produce a magnetic moment on the implant, and this magnetic moment, in the presence of the static magnetic field, can generate a torque via the Lorenz Force Law, $\boldsymbol{F} = \boldsymbol{v} \times \boldsymbol{B}$**.** The induced torque causes a high frequency mechanical vibration in the neural probes [50].

The magnetic moment for a volume with a non-uniform charge distribution is defined by the differential magnetic moment:

$$\boldsymbol{\mu} = r \times \boldsymbol{J} \qquad \textit{(Equation 2.19)}$$

where $\boldsymbol{\mu}$ is the magnetic moment, r is the position vector and $\boldsymbol{J}$ is the electric current density. The magnetic torque is defined by the cross product of the magnetic moment and the static magnetic field:

$$\boldsymbol{\tau} = \boldsymbol{\mu} \times \boldsymbol{B} \qquad \textit{(Equation 2.20)}$$

As mentioned before, since the current inducing this torque in the presence of the static magnetic field ($\mathbf{B_0}$) is a time-varying current, induced by the gradient magnetic field, it causes a vibration on the implant with a frequency similar to the switching frequency of the gradient coils.

2.3.11 Magnetic Perturbation and Imaging Artifacts

In temporal and special mapping of the brain, and during intracortical electrode implantation, MR imaging is essential. However, due to the magnetic susceptibility (χ) difference between the electrodes and the tissue the static magnetic field (**B_0**) around the electrodes may be distorted and visible artifacts observed. This can simply compromise the anatomical information that is obtained by the MRI scans and degrades the quality of the images taken [53], [59]. Another condition that may lead to unwanted artifacts is the high conductivity of the metallic parts used in the implants. This highly conductive materials can distort the **B_1** field around the implant resulting in artifacts. The focus of this section, however, is the artifacts caused by the magnetic susceptibility difference, $\Delta\chi$.

Table 2.1. Magnetic Susceptibility of neural implant materials and the human tissue [59].

Material	**Magnetic Susceptibility, χ_v (ppm)**
Human Tissue	-9.05
Silicon Carbide	-12.87
Silicon	-4.2
Gold	-34
Platinum	279

Magnetic susceptibility is a magnetic property of all materials, denoted by χ, that shows the degree of magnetization in materials when they are exposed to a static magnetic field (**B_0**). χ can be positive or negative depending if the magnetization vector aligns in the direction of **B_0** or opposite to it, respectively. If the magnetization vector is the same direction as **B_0**, then the material is called paramagnetic, and if the magnetization vector is opposite to the **B_0**, it is called diamagnetic

[79]. Magnetic susceptibility of human tissue and some of the materials commonly used for neural implant fabrication are listed in Table 2.1 [59].

Magnetic perturbation surrounding an arbitrarily shaped electrode placed inside a tissue-like material can be calculated using a Fourier based method explained elsewhere [59], [60]. In these mathematical models, the magnetic perturbation caused by a magnetic susceptibility difference is defined as an offset in the magnetic field from the main static magnetic field ($\mathbf{B_0}$) that the set-up is exposed to, and it is denoted by $\Delta \boldsymbol{B_z}(\boldsymbol{r})$. The z subscript in the $\Delta \boldsymbol{B_z}(\boldsymbol{r})$ term is due to the direction of $\mathbf{B_0}$ that is assumed to be in z direction. In order to find the value of $\Delta \boldsymbol{B_z}(\boldsymbol{r})$, first the magnetization needs to be calculated in space:

$$\boldsymbol{M}_z(\boldsymbol{r}) = \boldsymbol{\chi}(\boldsymbol{r}) \frac{\boldsymbol{B_0}}{\mu_0(1 + \boldsymbol{\chi}(\boldsymbol{r}))} \qquad \textit{(Equation 2.21)}$$

where $\boldsymbol{\chi}(\boldsymbol{r})$ is the magnetic susceptibility in space, $\boldsymbol{M}_z(\boldsymbol{r})$ is the magnetization in space in the z direction, and μ_0 is the magnetic permeability of free space. Then, the 3D Fourier transform of $\boldsymbol{M}_z(\boldsymbol{r})$ is used to transform to *k*-space, as shown in Equation 2.22:

$$\boldsymbol{M}_z(\boldsymbol{k}) = \mathcal{F}_{3D}\{\boldsymbol{M}_z(\boldsymbol{r})\} \qquad \textit{(Equation 2.22)}$$

Considering that β is the angle between the direction of the $\mathbf{B_0}$ and the $\boldsymbol{k}$ vector defining a point in *k*-space, the magnetic perturbation in *k*-space, $\Delta \boldsymbol{B_z}(\boldsymbol{k})$, is calculated via Equation 2.23:

$$\Delta \boldsymbol{B_z}(\boldsymbol{k}) = -\frac{\mu_0 \boldsymbol{M}_z(\boldsymbol{k})}{3} (3cos^2\beta - 1) \qquad \textit{(Equation 2.23)}$$

In equation 2.23, $cos\ \beta$ is calculated using Equation 2.24:

$$cos\beta = \frac{-k_x sin\theta + k_y cos\theta sin\psi + k_z cos\theta cos\psi}{\sqrt{{k_x}^2 + {k_y}^2 + {k_z}^2}} \qquad \textit{(Equation 2.24)}$$

In Equation 2.23, θ indicates a rotation about the y axis, and ψ about the x axis. Finally, $\Delta \boldsymbol{B_z}(\boldsymbol{r})$ is calculated in r-space after finding the inverse Fourier transform of the $\Delta \boldsymbol{B_z}(\boldsymbol{k})$ as shown in Equation 2.25.

$$\Delta \boldsymbol{B_z}(\boldsymbol{r}) = \mathcal{F}_{3D}{}^{-1}\{\Delta \boldsymbol{B_z}(\boldsymbol{k})\} \qquad \textit{(Equation 2.25)}$$

Using the above equations, the magnetic perturbation caused by the susceptibility difference can be mathematically modelled and calculated using MATLAB for any arbitrary shaped electrode placed inside a tissue-like material.

2.4 Chapter Summary

In the beginning of this chapter an overview of semiconductor materials was provided. This was followed by an overview of the wide-band-gap semiconductor, silicon carbide (SiC) as the material of interest for neural probe fabrication. Since one of the main purposes of this dissertation research was to to evaluate the magnetic resonance imaging (MRI) compatibility of monolithic cubic silicon carbide (3C-SiC) based neural implants, the theories behind this very powerful imaging technique were elaborated, which is mainly related to nuclei spin physics. Then, various magnetic fields and the hardware used to generate these magnetic fields in an MRI machine were covered. Patient safety under MRI, and the risks involved in an MRI procedure for a patient with implants along with the sources of these risks, were discussed. The volume birdcage resonator, as one of the most common coils used in MRI for generating RF signals, was covered and the specific absorption rate (SAR) with respect to the RF signals under MRI discussed. Finally, artifacts caused by a magnetic susceptibility difference under MRI was explained and a mathematical model to calculate the magnetic perturbation introduced around arbitrary shaped implants under MRI presented to predict the presence of image artifacts.

Chapter 3: Fabrication and Initial Characterization of a Monolithic Silicon Carbide Neural Probe [1]

3.1 Introduction

As mentioned in the first chapter, for an intracortical neural interface (INI) to stimulate and record neural signals reliably over many years, both the choice of probe materials and their homogeneity must be carefully taken into consideration. Crystalline silicon carbide (SiC) is a semiconductor with a short bond length that gives it high physical resilience and chemical inertness. One of the important properties of SiC is that it displays polymorphism, which results in numerous single-crystal forms with the principal polytypes being hexagonal (i.e., 4H- and 6H-SiC) and cubic (i.e., 3C-SiC). SiC has been used in both the high-power electronics and MEMS industries [30], [31]. It has also demonstrated a high degree of biological tolerance in-vitro [33], [35], [61], [120]. In addition, amorphous SiC (*a*-SiC), which provides excellent electrical insulation, has also shown good compatibility with neural cells [40], [44], [120] and has previously been used in the fabrication of several types of MEAs [39], [44]–[48]. The properties of crystalline and *a*-SiC, and the results of previous studies, indicate that SiC can address the interrelated issues of INI biocompatibility and long-term reliability. Previously, the fabrication and characterization of nearly monolithic MEAs made from 4H-SiC, a hexagonal polytype of crystalline SiC, with *a*-

[1] This chapter was published in micromachines (MDPI), under an open access Creative Common CC BY license. Any part of the article may be reused without permission provided that the original article is clearly cited. (Beygi, M., Bentley, J. T., Frewin, C. L., Kuliasha, C. A., Takshi, A., Bernardin, E. K., ... & Saddow, S. E. (2019). Fabrication of a Monolithic Implantable Neural Interface from Cubic Silicon Carbide. Micromachines, 10(7), 430.)

SiC insulation was reported [36]. However, the manufacture of these devices, as well as their release from the bulk 4H-SiC wafer, made these devices difficult to fabricate and quite costly.

In this chapter, the design and fabrication of a Michigan-style 3C-SiC neural probe on a silicon-on-insulator (SOI) wafer for ease of manufacture is reported. The probe is composed of 3C-SiC, which was epitaxially grown on a SOI wafer. A heavily doped n-type (n^+) 3C-SiC film was grown on a moderately doped p-type 3C-SiC layer, forming a p-n junction. The n^+ layer was used to form the electrode traces and recording sites, eliminating the need for metallic conductive traces and recording sites that are in direct contact with the CNS tissue. The p-n junction structure provides substrate isolation between the conductive traces. A thin film of *a*-SiC was deposited via plasma-enhanced chemical vapor deposition (PECVD) on the probe to provide insulation from the external environment. The oxide buried in the SOI wafer served as a sacrificial layer, allowing the SiC probe to be released from the wafer with a selective wet etch process. This new fabrication approach, based on the demonstrated all-SiC probe design, eliminates residual stresses typically found in similar devices consisting of stacks of heterogeneous films. It is expected that this approach will enhance the long-term material stability of implantable neural probes in the CNS, therefore increasing device reliability over many years. However, now that the manufacture of the probes has been demonstrated, follow-on studies in laboratory animals is required to support this hypothesis.

3.2 Materials and Methods

The all-SiC neural probe was developed using variations of standard silicon semiconductor micromachining processes. This started with the epitaxial growth of a 3C-SiC film on a SOI wafer [30], followed by patterning of the 3C-SiC epitaxial films via thin film contact photolithography

techniques. This was followed by the subsequent etching of the electrode traces and recording sites using a deep-reactive ion etching (DRIE) process, deposition of a conformal *a*-SiC film via PECVD, the opening of windows in the *a*-SiC film via RIE (recording and wire-bonding sites) and a final probe definition etch through the buried oxide layer via another DRIE process. The final step was the release of the finished device from the substrate SOI wafer by wet etching the buried oxide layer. The fabrication steps and the details of each step is presented in Appendix 1.

The thickness of the doped epitaxial films was measured using cross-section scanning electron microscopy (SEM) and the composition was verified through energy-dispersive X-ray spectroscopy (EDS). No sulfur -peak was observed in the EDS spectrum, indicating that the device surface was free of chemical residue from the etch processes (Figure 3.1 (a,b)). Raman spectroscopy and X-ray photoelectron spectroscopy were utilized to assess the 3C-SiC and *a*-SiC film quality, respectively (Figure 3.1 (c,d,e)). A commercial connector (Nano Strip, Omnetics Connector Corporation, Minneapolis, MN, USA) was used to make the electrical connections to the probe. Planar single-ended test microelectrodes were fabricated from the same epiwafer material as the implants for ease of electrical testing. Cyclic voltammetry (CV) and electrochemical impedance spectroscopy (EIS) in a phosphate buffered saline (PBS) solution, as well as p-n junction isolation and leakage current tests, were conducted on the test microelectrodes to electrically characterize the fabricated probes.

3.2.1 Epitaxial Growth of 3C-SiC on SOI

A 100 mm diameter SOI ((100) Si-oriented) wafer, with an ~26 μm silicon film on top of an ~2 μm buried thermal oxide layer, was used for fabrication of the all-SiC neural probes reported here. The growth process started with epitaxial growth of an ~8 μm thick p-type 3C-SiC film on

the SOI wafer, followed by an ~2 μm heavily n-type (n^+) film, using a hot-wall reactor (LPE Epitaxial Technology, Baranzate, Italy) [121]. Heavy doping of semiconductors results in semi-metallic performance, which is the case for the n^+ 3C-SiC layer. For this to be achieved, a n^+ doping density of ~10^{19} dopants/cm^3 is required. Hydrogen (H_2) was used as a carrier gas [31], ethylene (C_2H_4) as the carbon precursor, and trichlorosilane ($SiHCl_3$) as the silicon precursor gas. The epitaxial growth temperature was set to ~1370 °C with a process pressure of ~75 Torr. The C:Si ratio was kept between 0.8 and 1.2 throughout the epitaxial growth process. Aluminum and nitrogen were the p and n dopants, respectively, and were introduced during the epitaxial growth process [122], [123]. The doping level of the top n^+ 3C-SiC film was measured with a LEI 2017b Mercury (Hg) Probe (Lehighton Electronics, Inc., Lehighton, PA, USA) [36].

3.2.2 Fabrication of All-SiC Neural Probe

The fabrication process sequence is shown in Figure 3.2. First, the epiwafer with the SiC films was cleaned in a solvent and then a RCA bath. It was then dipped in hydrofluoric acid (HF, 49%, J. T. Baker, Inc., Phillipsburg, NJ, USA) diluted in water (50:1) to remove any oxide that may have formed on top of the epitaxial 3C-SiC layer, followed by a DI water rinse and N_2 dry. Next, the wafer surface was functionalized with HMDS (Hexamethyldisilazane; Microchemicals GmBH, Ulm, Germany) and a 15–18 μm layer of AZ 12XT-20PL positive photoresist (Microchemicals GmBH) was spun on top at 1500 rpm (masks shown in Appendix A). After a soft-bake at 110 °C for 3 min, the photoresist was patterned by UV exposure (110 mJ/cm^2) with a Quintel Mask Aligner and then baked at 90 °C for 1 min. The wafers were re-hydrated at ambient condition for 2 h and then developed with AZ300 developer (Microchemicals GmBH). The patterned photoresist was thick enough to allow for a ~3 μm deep etch of the epitaxial film using

an Adixen AMS 100 DRIE. This process used oxygen (O_2) at 10 sccm and sulfur hexafluoride (SF_6) at 90 sccm. The pressure inside the chamber was set to 5.7 mTorr and the sample holder temperature was set to −20 °C. The sample holder power was kept at 550 W, while the source RF power was 1800 W. This process formed the traces and electrode sites on the probes.

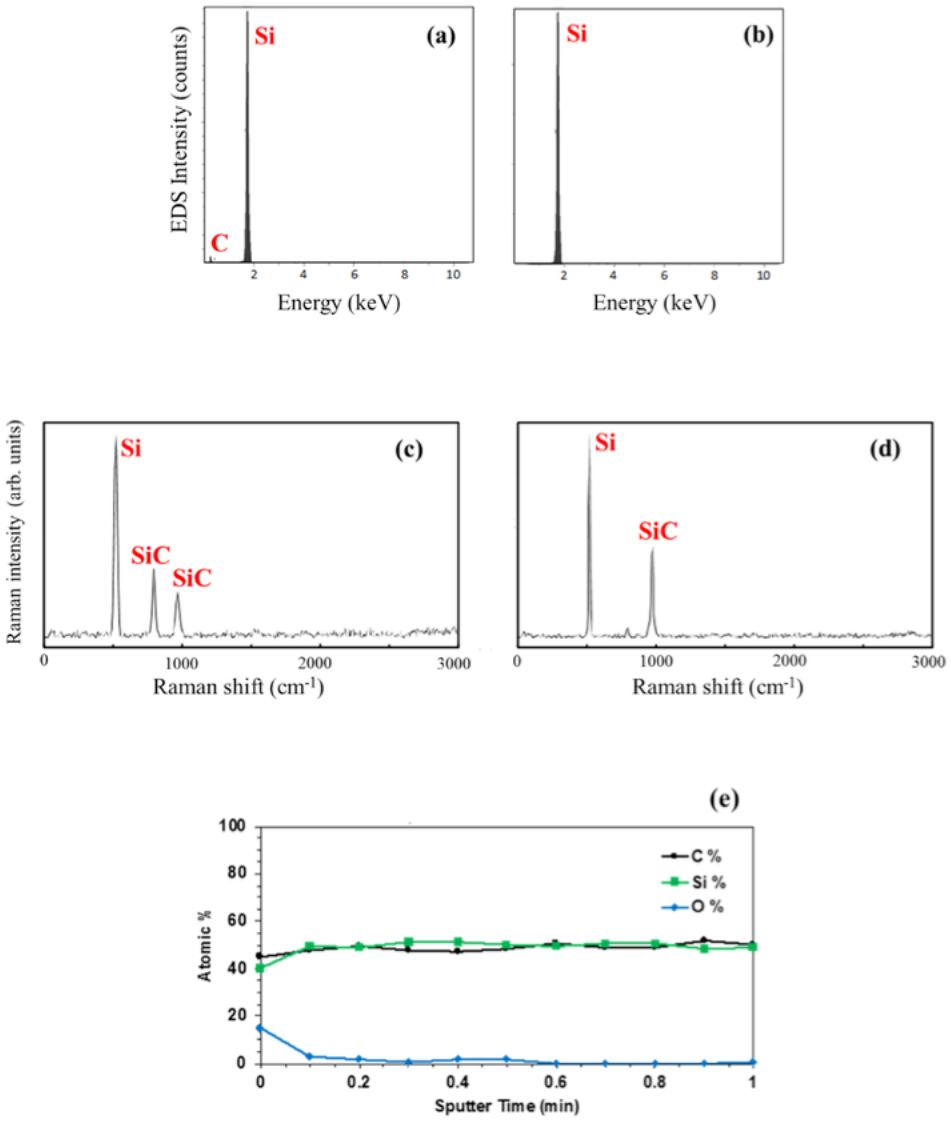

Figure 3.1. Quality assessment of the grown 3C-SiC film and the deposited *a*-SiC film. (a) Shows the EDS results for the top 3C-SiC epi layer which has both C and Si. (b) Shows the EDS results for the Si layer in SOI wafer that contains just Si. (c) The Raman spectrum showing the peaks for the 3C-SiC film grown on the SOI wafer. The surface of the film contains defects. (d) The Raman spectrum for the 3C-SiC film without defects. (e) XPS results showing the composition of *a*-SiC in various depths of the deposited film [161].

A ~250 nm layer of *a*-SiC was deposited on the sample using PECVD (Unaxis 790, PlasmaTherm, Saint Petersburg, FL, USA) at the University of Florida [ref]. Methane (CH_4) and silane (SiH_4, 5% in He) were used as the reactive gases to produce the *a*-SiC with flow rates of 200 sccm and 300 sccm, respectively. Helium (He), with a flow rate of 700 sccm, was used as the carrier gas. The RF power was set to 200 W, substrate temperature to 300 °C, and pressure to 1100 mTorr [34], [36]. Following photoresist patterning using AZ 15nXT-450 CPS negative photoresist (Microchemicals GmbH), a reactive ion etch (RIE) step (PlasmaTherm 700) was run for 210 s to open windows in the *a*-SiC film for the electrode and contact pad sites. Tetrafluoromethane (CF_4) and O_2, at 37 sccm and 13 sccm, respectively, were used as the process gases. The power was set to 200 W and the chamber pressure to 50 mTorr. In order to package the probes for electrical testing, metal bonding pads were formed on one end of the traces (for the implants this is located on a tab that would reside outside the skull of the animal during in-vivo testing). A 20 nm titanium (Ti) film, followed by a 200 nm gold (Au) film, was deposited without breaking vacuum in an electron beam evaporator and patterned using a lift-off process. Thermal annealing was performed to create an ohmic contact at the interface between the semiconductor and metal in a rapid thermal processor at 650 °C for 10 min [124]. This process sequence formed the contact pads for the commercial connector, which was used to connect the electrodes to external electronics.

The last step of the fabrication process was probe release. The same DRIE etch recipe that was used for formation of the traces was employed in an etch-through process to define the probes, except that the duration was increased to 15 minutes in order to ensure a complete through-etch of the 3C-SiC epitaxial films and top silicon layer. A scrap piece of the epiwafer was cleaved and cross-section SEM used to determine the 3C-SiC epilayer and Si device layer thickness so that proper etch depth and mask thickness were selected. After removing the photoresist, the etch depth

was measured using a contact profilometer (Dektak 150, Veeco, Plainview, NY, USA). The probes were released via wet etch of the sacrificial oxide layer with HF (49%). They were then carefully removed from the HF solution, rinsed with DI water, and dried with N_2. To remove the backside silicon, the probes were soaked inside a KOH bath for 20 min. The residual Si was removed during this process and thin semi-transparent probes were remained in the solution.

3.2.3 P-N Junction Isolation and Leakage Evaluation

Since p-n junctions were formed between the n^+ and p epitaxial films, back-to-back diodes are present between adjacent traces, which provides substrate isolation. This isolation was evaluated by measuring the forward and reverse blocking voltages of test structures consisting of p-n diodes and n-p-n junctions formed between adjacent traces that were built on the 3C-SiC wafer. A Keithley 2400 SourceMeter (Tektronix, Inc., Beaverton, OR, USA) was used to generate current-voltage (I-V) plots for adjacent traces to observe these voltages. The voltage was increased from −10 V to +10 V at a rate of 0.1 V/s for the diodes and n-p-n junctions, and the observed currents recorded. The forward voltage was estimated using a semi-logarithmic current scale I-V plot [125]. The breakdown voltage occurs when the current rapidly increases during application of negative voltage. The root mean square (rms) of the current amplitude between breakdown and forward potentials for the diodes was defined as reverse leakage current [36]. The threshold current for defining the breakdown voltages was 10 µA.

3.2.4 Electrochemical Characterization of All-SiC Probes

Electrochemical characterization of the 3C-SiC electrodes was performed via CV and EIS evaluation. A three-electrode setup was used with a potentiostat (VersaSTAT 4, AMETEK, Inc.,

Berwyn, PA, USA) to adjust the voltage between the working and counter electrodes in the presence of a reference electrode. CV provided information on the charge transfer properties of the electrode-electrolyte interface and on the presence of electrochemical reactions and their reversibility. Potential limits of −600 mV and +800 mV, which is the electrochemical water window for platinum (Pt), were chosen for CV evaluation because this allowed for direct comparison of our measurements with previously published results [44], [48], [126], [127]. EIS provided complex impedance measurements (both magnitude and phase) at frequencies of interest, which were used to evaluate the performance of the n^+ 3C-SiC conductor traces and electrodes.

Planar test microelectrodes fabricated alongside the neural probes on the same wafer were used for CV and EIS measurements [36], [128]. The measurements were performed at room temperature in PBS with a pH of 7.40 ± 0.01, which was adjusted with hydrochloric acid (HCl). The PBS was composed of 137 mMol NaCl, 2.7 mMol KCl, and 10 mMol Na_2HPO_4. The gas levels in the PBS were ambient and no bubbling was done. The counter electrode was Pt and the reference electrode were Ag|AgCl. EIS measurements were performed from 0.1 Hz to 1 MHz with a rms voltage of 10 mV. The current was recorded 12 times per decade and three repetitions were averaged. CV measurement was initiated from an open circuit potential, swept to −600 mV, and increased to +800 mV at a rate of 50 mV/s. This cycle was repeated three times and results were averaged. Charge values were calculated from the CV I-V curve via numerical integration with the trapezoidal method, trapz, in MATLAB (MathWorks, Natick, MA, USA).

3.3 Results

3.3.1 Epitaxial 3C-SiC Films

A cross-sectional SEM view of the wafer, which allows for accurate estimation of film thickness (n^+- and p-SiC, Si device film, and buried oxide), is shown in Figure 3.3 (a). This figure highlights the various layers and the approximate thickness of each layer on the wafer used for the fabrication.

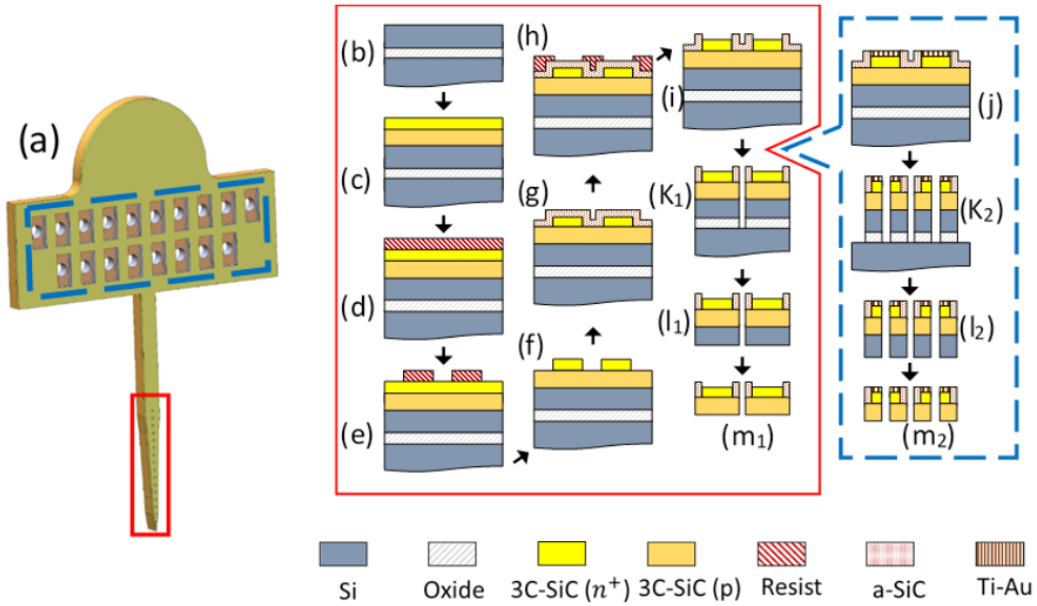

Figure 3.2. The all-SiC fabrication process flow. (a) A rendering of the Michigan-style 3C-SiC probe. The process flow inside the red rectangle shows the cross-section at the electrode sites while the blue rectangle provides the cross-section at the contact pads on the tab. (b) Starting SOI wafer, (c) ~8 µm of p-type 3C-SiC was grown on top, followed by ~2 µm of heavily n-type (n+) 3C-SiC. (d) The wafer was coated with photoresist and (e) patterned via photolithography. (f) DRIE process was used to form the conductive n+ mesas and (g) a thin *a*-SiC insulating layer was deposited on top via PECVD. (h) Photoresist was then patterned with photolithography and (i) the *a*-SiC was etched to form windows for the electrode sites using a RIE process. (j) After the *a*-SiC windows were opened, a layer of titanium, followed by gold, was deposited on the contact pads and thermally annealed. A deep DRIE etch through both epi layers and the oxide was performed to (k1) define the probes and (k2) form through-holes in the contact pads. (l1, l2) The oxide layer was etched in HF (49%) to release the probes. (m1, m2). The probes were soaked inside KOH solution to remove the residual silicon from the SOI device layer.

The two epitaxial 3C-SiC films were measured, and their combined thickness determined to be ~10 µm. The SOI Si device layer (~26 µm), as well as the thin (~2 µm) buried oxide layer, are also visible in this figure. The epitaxial n^+ film in the center of the wafer was quite rough with a mean surface roughness of ~244 nm and smoother near the wafer edge with a mean surface roughness of ~21 nm. Figure 3.3 (b) shows surface morphology of the smooth n^+ layer, which was taken using a DI AFM (Dimension 3100). Although rough in the wafer center (Figure 3.3 (c)), the surface roughness was low enough for thick layers of photoresist to properly cover the entire surface for the subsequent fabrication steps. However, this roughness would be expected to impact device electrical performance, particularly p-n diode leakage current.

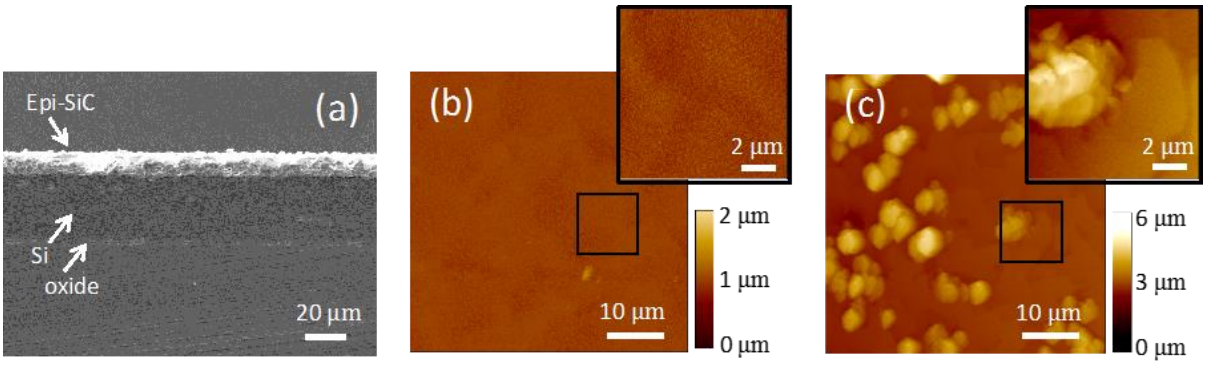

Figure 3.3. Analysis of epitaxial SiC results. (a) Cross-section SEM micrograph of the 3C-SiC epi films on SOI. (b) AFM image (tapping mode) of the 3C-SiC epiwafer specular region on the wafer periphery that shows typical 3C-SiC surface morphology (mean roughness of ~21 nm). (c) AFM image (tapping mode) of the rough surface of the same epiwafer (center) (mean roughness of ~244 nm). The devices were fabricated from the center of the wafer.

3.3.2 Fabricated All-SiC Neural Probe

Epitaxial growth of single crystalline 3C-SiC with different types of doping enables realization of a nearly monolithic probe from homogeneous SiC material. The all-SiC probe is a Michigan-style, planar neural probe with 16 electrodes for recording and stimulating neurons. The connector tab has 18 metallic pads (approximately 0.8 mm by 0.4 mm) with through holes to which

a commercial Omnetics connector is bonded. Two extra pads provide connections for the return and reference electrode wires. The diameter of the electrode sites is ~15 μm and width of the traces is ~10 μm. Figure 3.4 shows the optical and SEM micrographs of a free-standing probe.

The probe's shank, which contains the traces and electrode sites, is shown in Figure 3.4 (b). This figure shows a scanning electron micrograph of the electrode sites, which have *a*-SiC windows on top to allow contact with the extracellular environment. The traces and electrode sites are mesas formed from the n^+ 3C-SiC film. There are no metallic components on the shank, which is a homogeneous structure consisting entirely of SiC. The pads, which are shown in Figure 3.4 (c), contain titanium and gold layers in order to provide ohmic connections to external electronic devices via the Omnetics connector. However, since the metallic pads are not in direct contact with brain tissue, the issues regarding delamination of metallic parts and compatibility with CNS tissue are not a concern.

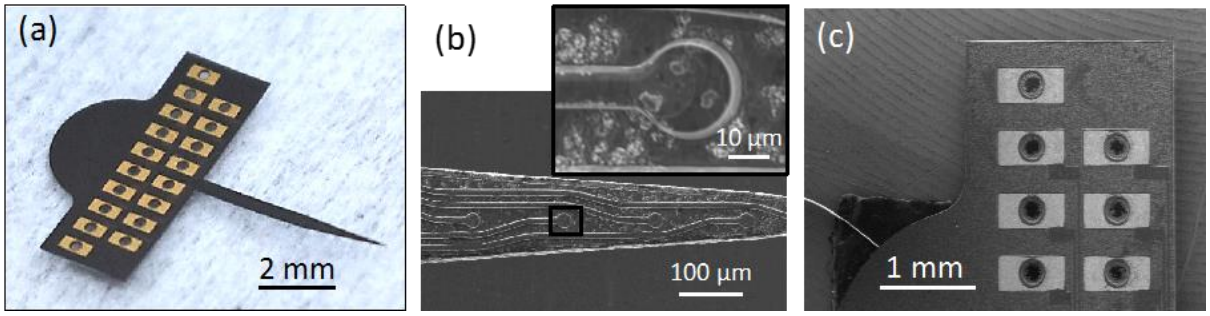

Figure 3.4. Physical characterization of the completed neural probe. (a) Optical image of a freestanding all-SiC probe after release. (b) SEM image of the shank tip showing four of the electrode sites and a magnified image of a single electrode site (inset). (c) SEM image of some of the metal contact pads with through holes. The shank is 5.1 mm long and the length of the tapered portion is 2.4 mm. The tab is 6.64 mm wide and 2.3 mm long, excluding the semi-circular top portion. The surface roughness of the electrode sites is shown in Figure 3.3 (c).

3.3.3 Electrical and Electrochemical Characterization

The doping density of the top n^+ 3C-SiC film was determined by measuring the capacitance voltage profile of the Schottky contact at 1 MHz and the net charge concentration, N_D-N_A, was estimated to be ~10^{19} cm^{-3}. A similar measurement was also performed on the p-type epitaxial film exposed after DRIE processing and N_A- N_D was estimated to be ~10^{16} cm^{-3}. These measurements indicate the feasibility of p-n junction formation between two epi films and high electrical conductivity of the top semi-metallic n^+ film that formed the traces and electrode sites. EIS was performed to confirm this expectation.

As shown in Figure 3.5 (a), current-voltage (I-V) measurements on individual diode structures had a rectifying effect due to the diode formed between the n^+- and p-type epitaxial films. In order to measure turn-on and breakdown voltages and the reverse leakage current, the I-V plot for four diodes on the same wafer was measured. The averaged turn-on voltage for these four diodes was determined to be ~1.4 V, with an average leakage current less than 8 μA_{rms}. In addition, Figure 3.5 (a) also contains a current-voltage curve, obtained from measurements on one of the IDEs, showing isolation between adjacent traces.

CV curves for four test microelectrodes of the same surface area (491 μm^2) in 7.4 pH PBS are shown in Figure 3.5 (b). The upper (+800 mV) and lower (−600 mV) boundaries for the potential were based on the electrochemical window for Pt in water. The shape of the hysteresis cycle showed that the anodic and cathodic currents were charge balanced, with no indication of faradaic current resulting from oxidation or reduction reactions between +800mV and −600 mV. However, the phase behavior of the electrode-electrolyte interface (Figure 3.5 (d)) only supports a capacitive-dominant mechanism at higher frequencies (e.g., −61.2 ± 3.7° at 1 kHz), while at lower frequencies the phase indicates a faradaic current (e.g. −30.3 ± 4.9° at 100 Hz), which contrasts

with earlier results from 4H-SiC microelectrodes [36]. The average anodic charge storage capacity (CSC) was 15.4 ± 1.46 mC/cm^2 (mean ± standard deviation) and the cathodic CSC was 15.2 ± 1.03 mC/cm^2. The average anodic charge per phase was 75.4 ± 5.06 nC and the average cathodic charge per phase was 74.8 ± 5.06 nC.

Figure 3.5 (c) and 3.5 (d) show the EIS results for the same four test microelectrodes. As expected, the impedance magnitude was found to increase with decreasing frequency. At a frequency of 1 kHz, the impedance was 165 ± 14.7 kΩ (mean ± standard deviation). The electrode-electrolyte interface was determined to be predominately capacitive, as indicated by the negative phase angles for higher frequencies (i.e. >1 kHz).

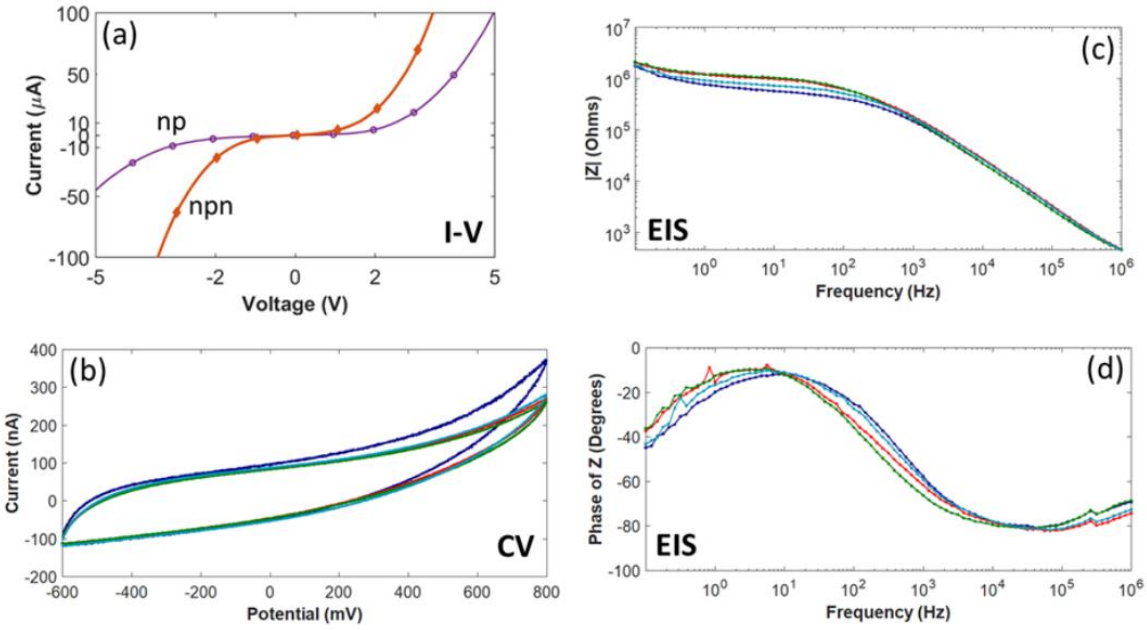

Figure 3.5. All-SiC p-n diode and n-p-n junction characterization and electrochemistry for four test microelectrodes with an area of 491 μm^2. (a) I-V measured from a p-n diode and a n-p-n junction between adjacent traces fabricated on the same wafer used for probe fabrication. (b) The cyclic voltammetry curves swept between +800 mV and −600 mV with a scan rate of 50 mV/s. (c) EIS Impedance (Z) magnitude (~165 kΩ @1kHz) and (d) impedance phase angles. The curve for each microelectrode (b-d) is the average of three replicates.

3.4 Discussion

A monolithic SiC neural probe has been fabricated from epitaxial 3C-SiC films grown on SOI wafers. A combination of ethylene (C_2H_4) and trichlorosilane ($SiHCl_3$) were used as precursor gasses in the epitaxial process. This produced a varying surface morphology with mean surface roughness of approximately ~21 nm (specular, edge region) to ~244 nm (rough, center region) [129]. It is possible this surface roughness contributed to complications in the fabrication process, such as with photolithographic patterning, and may have had an effect on the mechanical properties of the grown films to the detriment of probe function [130]. It is suspected that this contributed to the higher than desired leakage current (less than 8 μA_{rms}). By optimizing various parameters in the epitaxial process, such as gas composition and flow rates, temperature, and pressure [122], [129], the process can be improved to reduce this surface roughness. Additionally, post-processing steps, such as mechanical or chemo mechanical polishing (CMP), can be added to further improve the surface morphology; particularly to reduce surface roughness [31].

A major issue with the previous 4H-SiC probes was the difficulty in releasing the probe [36]. Essentially, much of the 4H-SiC substrate would have to be removed, and there was no effective etch stop to prevent over-etching. In order to effectively solve this issue, we used SOI wafers to provide an effective release layer by the simple process of wet etching the oxide. However, the SOI wafer used here possessed a relatively thick layer of silicon that remained on the backside of the probes, which was removed later via KOH soaking. This thick silicon layer can cause residual stress, due to mismatches in the coefficients of thermal expansion and lattice parameters [131] at the interface between the SiC films and silicon, resulting in bowing or bending of the probes. The SOI wafer used in this work had an ~20 um thick top silicon layer and this may have been the cause of the bowing of the shank and some warping in the connector tab. The shank

should be straight for a proper insertion trajectory into the neural tissue. Also, in order to maximize contact at the connector interface, the tab containing the contact pads should be as planar as possible. Using a SOI wafer with a thin silicon device layer may resolve this deformation problem and will be used in future all-SiC devices.

Epitaxial 3C-SiC thin films are ceramic-like materials with, relative to neural tissue, a high elastic modulus, measured to be 424 ± 44 GPa using microsample tensile testing [132]and 433 ± 50 GPa using nanoindentation [133]. Defects can reduce the value the Young's modulus of 3C-SiC [134] and doping may affect this value as well [135]. There is a trend towards utilizing softer materials, such as polymers, for implantable neural interfaces due to their potential to improve the interaction with neural tissue [136]–[138]. By decreasing the Young's modulus of the neural probe closer to the values of neural tissues, the harmful shear and normal stress applied from the shank to the tissue should decrease. However, it is really device stiffness, which includes cross-sectional area, rather than just device modulus, that seems to matter the most [139]. Additionally, use of these softer materials introduce challenges with fabrication processes, scaling to higher channel-count systems, particularly with respect to interconnects, and can lead to insertion difficulties. Once implanted, these materials face challenges with material stability and device reliability [140]. The hard, chemically inert nature, and ease of micromachining with traditional silicon processes means SiC neural probes may suffer less from these limitations. Clearly, long-term in vivo studies in an animal model are needed to assess the performance of the all-SiC INI and are planned.

It has been demonstrated that once the implanted structure size is reduced to subcellular scale, i.e. less than ~10 um, the foreign body response and associated neuron death is greatly reduced in a rat model [141], [142]. With traditional silicon probes, reducing size increases the occurrence of probe fracture at high stress regions [143]. SiC is a much more robust material, with

a reduced tendency to fracture at these desired smaller sizes, while maintaining the mechanical strength needed for proper penetration of neural tissue [44], [61]. Therefore, SiC is an excellent material for developing a high electrode density neural interface, allowing for further reduction in size while greatly minimizing risk of fracture.

The heterogeneous composition of implanted neural interfaces that utilize metallic materials as electrode sites or conductive traces may increase the risk of delamination in chronic implantation, specifically, at regions under higher stress [143]. Delamination usually occurs at the interface between metal and semiconductor materials due to residual stress in the thin films. A homogeneous material composition can eliminate this residual stress, reducing the risk of delamination at the interfaces between different materials in the probe by eliminating them.

3C-SiC is a wide-band-gap semiconductor with a high band energy of ~2.2 eV. This results in a higher turn-on voltage at the junction between n^+- and p-type SiC. This higher turn-on voltage provides a wider voltage range to stimulate neurons while isolating individual channels via n-p-n junctions supporting simultaneous multichannel microstimulation and recording, as might be necessary for implementing a closed-loop system. The turn-on voltage for p-n junctions built from Si is ~0.7 V, which is low compared to ~1.4 V for SiC and limits proper isolation via a n-p-n junction configuration. However, the higher leakage current in our all-SiC films may negatively affect the final device's functionality. Surface roughness is known to be associated with the density of crystal defects, thus a higher defect density may cause higher leakage current [129]. It is believed that the high surface roughness in this work, an indication of poor crystallinity, in conjunction with a high number of defects, may be the cause of the observed high leakage current. For reference, in our 4H-SiC devices with specular surface morphology, the leakage current was nA versus μA reported here [36]. A lower surface roughness via an optimized epitaxial growth

process would be expected to improve both the mechanical properties and the leakage current [144].

The EIS results revealed that the doped, semi-metallic 3C-SiC conductors have impedance values approaching those of metals commonly used in implantable microelectrodes, such as gold, platinum, or tungsten, as well as highly doped polysilicon [145], [146]. The average impedance for a surface area of 491 μm^2 was approximately 75% lower (165 kΩ vs. 675 kΩ at 1kHz) than previously reported for our 4H-SiC electrodes [36].

Both the charge balanced CV cycles and the negative phase angles from EIS measurements support a dominant capacitive charge transfer mechanism for 1 kHz and higher frequencies at the electrode-electrolyte interface, but faradaic currents may be present at lower frequencies. This differs from capacitive electrode materials like titanium nitride (TiN) [147], which has a phase closer to 90 ° at lower frequencies [148]. Compared to values previously reported for 4H-SiC, the charge values calculated from CV measurements reported here were approximately two orders of magnitude higher, with the average charge storage capacity (anodic: 15 mC/cm^2 vs. 0.41 mC/cm^2; cathodic: 15 mC/cm^2 vs. 0.19 mC/cm^2) and an average charge per phase (anodic: 75 nC vs. 2.0 nC; cathodic: 75 nC vs. 1.0 nC) using a Pt electrochemical window (−600 mV to +800 mV). It is possible that the greater surface roughness accounts for this large difference in electrochemical properties. It is also possible that there were more faradaic reactions at lower frequencies leading to more oxidation and reduction at the surface, which may be linked to defect sites in the SiC.

Current neural probe technology built from materials like silicon suffer from long-term reliability issues that reduces their lifetime considerably, resulting in loss of recording and microstimulation function when chronically implanted. This limits their use in medical applications for humans. Device-based modalities could become a more common alternative to

pharmaceuticals for treatment of neurological trauma or disease if the issue of long-term reliability in implantable neural interfaces is properly addressed. After further refinement of the design and optimization of the material processing, the performance of the all-SiC neural probe will be evaluated with chronic in-vivo experiments in rodent models to investigate its long-term safety and effectiveness in neural tissue. There is accumulating evidence [36], [40], [41], [44], [46]–[48], [149] that SiC could be an appropriate material for the greatly needed implantable neural interface that functions for the lifetime of the recipient.

3.5 Chapter Summary

In this chapter the fabrication and initial electrical characterization of an all-SiC neural probe was presented. The SiC neural probe was fabricated from p- and n^+-type 3C-SiC epilayers grown on SOI wafers. First, a moderately p-type 3C-SiC film was grown on a SOI wafer, followed by a layer of n^+-type 3C-SiC. The surface morphology of the top n^+ epilayer was measured. Neural probes with sixteen traces, electrode sites, and other test structures were patterned on the 3C-SiC epilayers via MEMS microfabrication processes. Metallic traces were absent from the shank of the probe, and instead a semi-metallic n^+ layer was formed into traces and electrode sites. A thin layer of *a*-SiC film was deposited on top of the epilayers to serve as an insulator. The probes were harvested using dissolution of the buried oxide layer in the SOI handle wafer to provide ease of manufacture. The backside silicon layer remaining after release of the probes was removed via KOH soaking. Adjacent traces were electrically isolated through a n-p-n junction. After completion of device fabrication, the performance of the n-p-n junctions was evaluated through current-voltage measurements and the turn-on voltage was determined to be ~1.4 V. Electrical measurements showed satisfactory p-n junction performance, but leakage current needs to be

improved via higher quality 3C-SiC epitaxial films. In addition, initial electrochemical characterization work with 491 μm^2 surface area test microelectrodes demonstrated good impedance, charge storage capacity, and charge per phase values. These results support the feasibility of neural stimulation and recording with the fabricated all-SiC neural probe. However, further studies are necessary to demonstrate the acute recording and stimulation capability and chronic stability of the fabricated SiC neural probes, and, consequently, in vitro accelerated aging and in vivo studies in a rodent model are planned and will be reported in the future.

Chapter 4: Silicon Carbide MRI Compatibility

4.1 Introduction

In this chapter, the magnetic resonance imaging (MRI) compatibility of the cubic silicon carbide (3C-SiC) is studied via finite element method (FEM) simulations, $\mathbf{B_0}$ perturbation simulations, and MRI experiments to validate the simulation results. The MRI compatibility of 3C-SiC is compared to other materials commonly used for neural implants such as platinum (Pt) and silicon (Si). Hereby, a comparative study with respect to MRI induced $\mathbf{B_0}$ perturbation or image artifacts, and MRI induced heating is presented to compare the MRI compatibility of 3C-SiC neural implants to the other mentioned materials. This chapter is structured as follow; first an introduction about MRI compatibility of neural implants is presented that covers metallic and semiconductor materials used for fabricating these neural implants. Next, the experimental and the simulation methods are explained which includes the simulation of $\mathbf{B_0}$ perturbation caused by magnetic susceptibility (χ) variations via the Fourier based method discussed in Chapter 2. Then FEM simulations to calculate the induced heat and specific absorption rate (SAR) under 7 T MRI excitation, as well as the design and implementation of a birdcage coil used for 7 T MRI, is presented along with the microfabrication of the samples used for the MRI experiments, Finally MRI experiments using the fabricated samples placed inside a tissue gel phantom under 7 T MRI machine for small laboratory animals in the Moffit Cancer Center (MCC) is presented and compared to simulated data. Lastly the results, conclusion and discussion are provided.

As mentioned in the previous chapters, 3C-SiC is a wide band gap semiconductor that has been proven to have a high compatibility with the neural tissue [61]. SiC has a specific molecular

structure with covalent bonding between silicon and carbon atoms. The length of this bonding is very short and this is gives SiC an extremely high chemical and mechanical stability [29]. SiC also has several polytypes and one amorphous structure which gives it a wide range of physical properties. The mechanical, chemical and electrical properties of SiC, as well as its high biocompatibility, have made SiC an attractive material for fabricating neural implants [39]–[41], [43], [44], [150].

The utilization of neuromodulation in the treatment of neurological disorders, such as chronic pain, Parkinson's disease, tremors and dystonia, has been growing during the past decade [151]. For many of these treatments, MRI is used as a modality to map the region of interest for implants inside the body and to monitor the post-operation/treatment condition. In addition, MRI is one of the common noninvasive diagnostic tools that gives high-contrast images of soft tissue while avoiding the use of ionizing radiation. For these reasons, being able to apply this powerful imaging technique to patients with implanted devices enables to use of this powerful diagnostic tool. Thus, the medical community is in need of neural implants that can remain in-body during MRI scans. Unfortunately, 'MRI compatible' implants have been of limited use as the maximum static magnetic field ($\mathbf{B_0}$) they may be used with is limited to 1.5 T for the most cases [50].

There are certain complications occurring when an implant with conductive or magnetic material is placed in an MRI machine. Patient safety and complication in post-implantation monitoring are the concerns that considerably limit the use of conductive and magnetic materials for fabricating neural implants [57]. A neural implant can interact with the static magnetic field ($\mathbf{B_0}$), gradient magnetic fields ($d\mathbf{B}/d\mathbf{x}$), and radio frequency (RF) fields ($\mathbf{B_1}$) in an MRI machine. This interaction between the electromagnetic fields and the neural implant can damage the surrounding tissue by induced mechanical vibrations and induced heat as reported in [49], [50],

[65], [151]–[153]. It can also reduce the quality of the images by introducing artifacts through implant interaction with $\mathbf{B_0}$ and, thus, complicates the interpretation of the images [53], [57], [154]–[156]. One last issue is the precision with which a neurosurgeon can place a neural implant and, at 1.5 T the resolution is on the order of cm which is insufficient for placing probes with precision in the brain. Figure 4.1 shows a comparison between a 7 T and 1.5 T MRI image illustrating the importance of MRI compatible neural implants for human use.

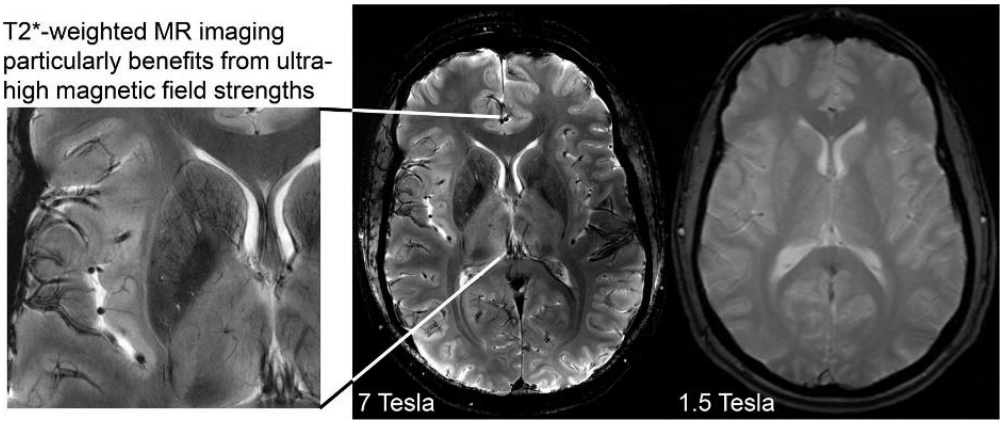

Figure 4.1. Comparison of a 7 Tesla (left) and 1.5 Tesla (right) MRI brain scan. This illustrates the need for higher $\mathbf{B_0}$ MRI imaging due to the significantly higher resolution available to the neurosurgeon during probe placement in the brain [157]. Taken from [157] through an open access article (permission is not required for non-commercial use).

In order to develop an implanted that possesses a higher level of compatibility with MRI magnetic fields in the brain, several approaches have been reported in the literature. In a recent study [53], glassy carbon (GC) microelectrodes were introduced that experimentally showed less artifacts, lower displacement and lower interaction with RF fields. In order for the GC electrodes to reduce their interaction with the RF field, the conductivity of the material was kept low, in the range of 6,803 S/m, in comparison with the platinum (Pt) which is 9.43×10^6 S/m. In addition, due to the negative magnetic susceptibility of GC in the range of χ = -1.2 ppm, it is believed that the artifacts caused by the magnetic susceptibility difference is minimized [53]. In another work,

in order to reduce the magnetic coupling between the penetrating electrodes and RF fields, the electrodes were coated with high dielectric materials [151], thus the RF energy was substantially reduced inside the dielectric material. Reported approaches to develop a more MRI compatible neural implant are mainly based on low electrical conductivity materials, materials with magnetic susceptibility compatible with tissue, and the shielding of electrodes with high dielectric materials or conductive coils [58], [64], [66], [75], [158]–[160]. Although many of the reported works have shown an improvement in MRI compatibility, neural implants that possess mechanical and chemical robustness, high compatibility with tissue, and MRI compatibility are absent.

In our previous work [161], we developed a monolithic Michigan style neural probe from cubic silicon carbide (3C-SiC). The *all*-SiC neural probe was monolithically fabricated from 3C-SiC, except on the contact pads that contained gold (Au). This fabrication method can potentially reduce the chance of delamination of the probe films inside the tissue environment. It also eliminates any metallic parts that come into contact with tissue thus increasing the tissue compatibility and decreasing the electric conductivity of the shank part of the probe. In addition, due to the high thermal conductivity of 3C-SiC (3.6-3.7 W/cm-K depending on the polytype while for Si this value is 1.49 W/cm-K, and for pure copper it is ~ 3.8 W/cm-K), and its tissue-compatible magnetic susceptibility (-12.87 ppm for SiC and -9.05 ppm for human tissue), SiC has an intrinsic advantage over conventional probe materials. When one considers the ability to form relatively high-resistivity conductive traces, in comparison with metals, neural probes fabricated monolithically from 3C-SiC may reduce the magnetic perturbation caused by magnetic susceptibility differences and decrease the heat generated by MRI induced currents on the neural probe conductive traces.

In this work, the magnetic compatibility of 3C-SiC, in comparison with Pt and Si, is studied. The focus of the current work is mainly on the artifacts caused by the magnetic susceptibility difference and the induced heat under MRI excitation. Multiple FEM simulations developed in ANSYS Multiphysics, and a Fourier based method for artifact measurement in MATLAB, as well as MRI experiments with fabricated devices inside polyacrylic acid (PAA) tissue phantoms, are utilized to study the MRI compatibility of 3C-SiC neural implants.

4.2 Materials and Methods

In order to evaluate the MRI compatibility of 3C-SiC neural implants, we took advantage of several FEM simulations, the Fourier-based method to estimate the image artifacts caused by magnetic susceptibility differences, and finally multiple MRI experiments to measure the artifacts of the samples and the temperature rise caused by electromagnetic coupling. Throughout this work, the MRI compatibility measurements for various materials used for the simulations, and the experiments, are limited to artifacts under MRI excitation caused by susceptibility differences, and the induced heat and SAR caused by electromagnetic coupling between the conductive parts of the samples and $\mathbf{B_1}$. The other possible scenarios, such as displacement and vibration under MRI, will be addressed in future works. In addition, artifacts surrounding the *all*-SiC Michigan style probe [161] is compared to a silicon based neural probe [14] as a reference to better determine the difference between artifacts caused by the two different technologies.

4.2.1 Sample Microfabrication

Various samples were fabricated for this study to compare artifacts and induced heating under 7 T MRI excitation. This includes 3C-SiC and Si samples with various doping type and

concentration, and platinum (Pt) metal on various substrates. The samples were fabricated using two different designs depending on whether they were used for artifact or induced heat assessments. The samples used for artifact measurements were basically a rectangular shape base electrode (15 mm × 4 mm) representing stimulating and recording electrodes used in neural probes. Other sets of samples were fabricated on various substrates with the similar dimensions as the base electrode, but this time with three parallel single-ended electrodes of various length (8 mm, 6 mm and 4 mm) on the substrate (masks shown in Appendix C). This design was chosen to study the effect of electrode length on both the artifacts and the resulting induced heat. It also helped us to determine how the electromagnetic coupling between the electrodes can influence the SAR distribution surrounding each electrode. In addition, since the electrodes were not large enough to produce enough of a measurable heat rise under 7T MRI excitation, a pair of extended stainless-steel wires (40 mm long) was attached to the electrodes to measure the induced heating. These measurements were used to verify the FEM simulations results. The SAR and the heat measurements using the FEM simulations proved to provide a better picture of the electromagnetic interactions between the electrodes and the $\mathbf{B_1}$ under MRI in the current study as the temperature resolution of the fiber-optic probes was insufficient to measure accurately volumetric heating in the tissue phantom.

Several samples were fabricated from various materials or a combination of materials. Using a combination of various materials during the experiments we were able to recognize, first, the effect of each material and, second, the effect of multiple stacks of materials in generating artifacts. The samples fabricated for the MRI experiments are shown in Figure 4.2. These samples are as follows.

(1) ~2 μm Heavily doped n-type (n^+) 3C-SiC epi-film on ~8 μm low doped p-type (p) 3C-SiC epi-film (n^+/p) on a silicon on insulator (SOI) substrate.

(2) ~2 μm Heavily doped p-type (p^+) 3C-SiC epi-film on ~8 μm low doped n-type (n) 3C-SiC epi-film (p^+/n) on a similar silicon on insulator (SOI) substrate.

(3) ~2 μm Heavily doped n-type (n^+) 3C-SiC epi-film on ~8 μm low doped p-type (p) 3C-SiC epi-film (n^+/p) on a p-type Si substrate.

(4) Sample (1) after etching away the oxide film in hydrofluoric acid (HF, 49%, J. T. Baker, Inc., Phillipsburg, NJ, USA) diluted in water (50:1) and etching away the remaining Si from the sample using potassium hydroxide (KOH) which results in a free-standing n^+/p 3C-SiC base electrode.

(5) Sample (2) after etching away the oxide film in hydrofluoric acid (HF, 49%, J. T. Baker, Inc., Phillipsburg, NJ, USA) diluted in water (50:1) and etching away the remaining Si from the sample using potassium hydroxide (KOH) which results in a free-standing p^+/n 3C-SiC base electrode.

(6), (7), (8) ~ 1 μm Pt film deposited on a polyimide (PI) film, n-type Si substrate, and p-type Si substrate, respectively.

(9), (10), (11) PI film, n-type Si substrate, and p-type Si substrate, respectively.

(12) ~100 nm Pt deposited on an n-type Si substrate and microfabricated into three parallel electrodes with pads and recording sites. Two 40 mm PFA-coated stainless-steel (coated diameter of 330 µm) were also soldered on the pads.

- *3C-SiC Sample Microfabrication*

Fabrication details are provided in our previous work [161]. To summarize, the 3C-SiC epitaxial layers (n^+ and p) was grown on three substrates, two of which were 100 mm diameter

SOI ((100) Si-oriented) wafer, and the other wafer was a p-type Si (100) wafer. Then, n- and p-type 3C-SiC films were grown on the substrates using a hot-wall reactor (LPE Epitaxial Technology Center, Catania, Italy). Hydrogen (H_2) and ethylene (C_2H_4) were used as carrier and carbon (C) precursor gases, respectively. Trichlorosilane ($SiHCl_3$) was used as the Si precursor gas.

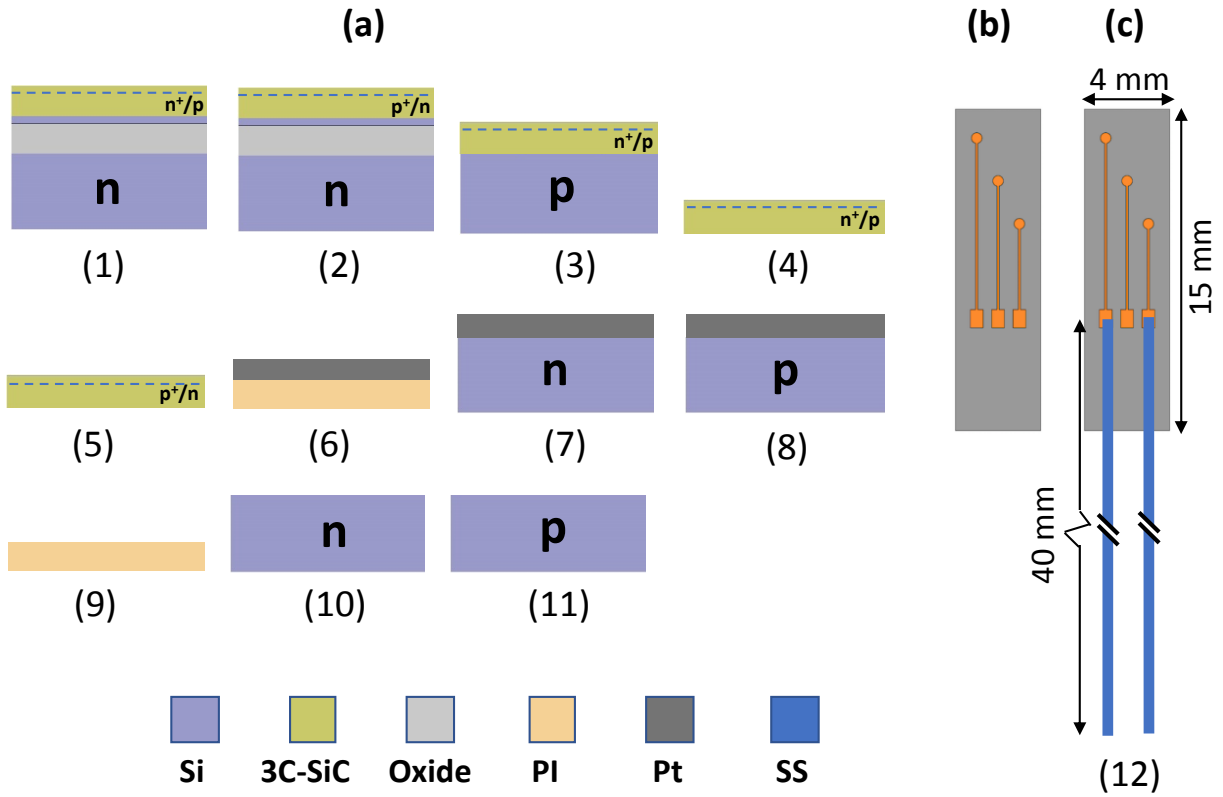

Figure 4.2. Samples fabricated for the MRI experiments. (a) cross section of the samples fabricated for the experiments measure artifacts. Each number is related to the number of the sample given in the section 4.2.1. Si stands for silicon, 3C-SiC for cubic silicon carbide, PI for polyimide, Pt for platinum and SS for stainless-steel. (b) illustrates top view of sample with triple electrodes (8 mm, 6 mm and 4 mm) used for SAR measurements. (c) Shows the sample used for heat measurement under MRI with two 40 mm extended PFA-Coated stainless-steel wires (coated diameter of 330 µm).

Aluminum (Al) and nitrogen (N_2) were added to the process as the p and n dopants, respectively. The doping density of n^+ on the n^+/p wafers, and p^+ on the p^+/n wafer was ~10^{19} dopants/cm^3. Finally, three wafers were diced into 15 mm × 4 mm pieces used as the base electrodes. Extra fabrication steps were necessary to release the n^+/p and p^+/n 3C-SiC films from the SOI wafers. First, samples (1) and (2) were soaked inside a HF (49%) bath for a few hours until the epitaxial films were released from the substrate. However, a thin layer of Si remained on the backside of the films. In order to etch this thin layer of Si from the backside of the samples, they were soaked in hot KOH. Figure 4.3 shows cross-section SEM micrographs of the 3C-SiC samples before and after the oxide and silicon etches.

- *Platinum Sample Microfabrication*

Platinum was deposited on various substrates: PI, n-type and p-type Si. Various substrates were selected to verify the substrate's influence on MRI artifacts surrounding the Pt electrodes. Nevertheless, in the case of neural probes Pt is deposited on another substrate. This substrate is either Si or a polymer film such as PI [53].

An ~1 μm thick Pt film was deposited via ebeam evaporation on two (2) p-type and n-type Si substrates. Using a 4-probe configuration, the resistivity of the p-type and n-type Si substrates was measured. The resistivity of the p-type substrate was ~9 Ω-cm and this value for the n-type substrate was ~0.5 Ω-cm. Prior to Pt deposition a very thin (20 nm) layer of titanium (Ti) was deposited in the same sputtering chamber which acts as an adhesion layer for Pt [162]. The base electrodes were ready after this step in the process. Another set of samples were fabricated with triple Pt electrodes on the substrate. Using a lift-off photolithography process, the Pt was patterned into the triple electrodes as illustrated in Figure 4.2(b). The details of the lift-off process are explained in our previous work [161]. Another Pt sample was prepared with two (2) 40 mm

extended stainless-steel wires to increase electromagnetic coupling and induced heat (Figure 4.2 (c)).

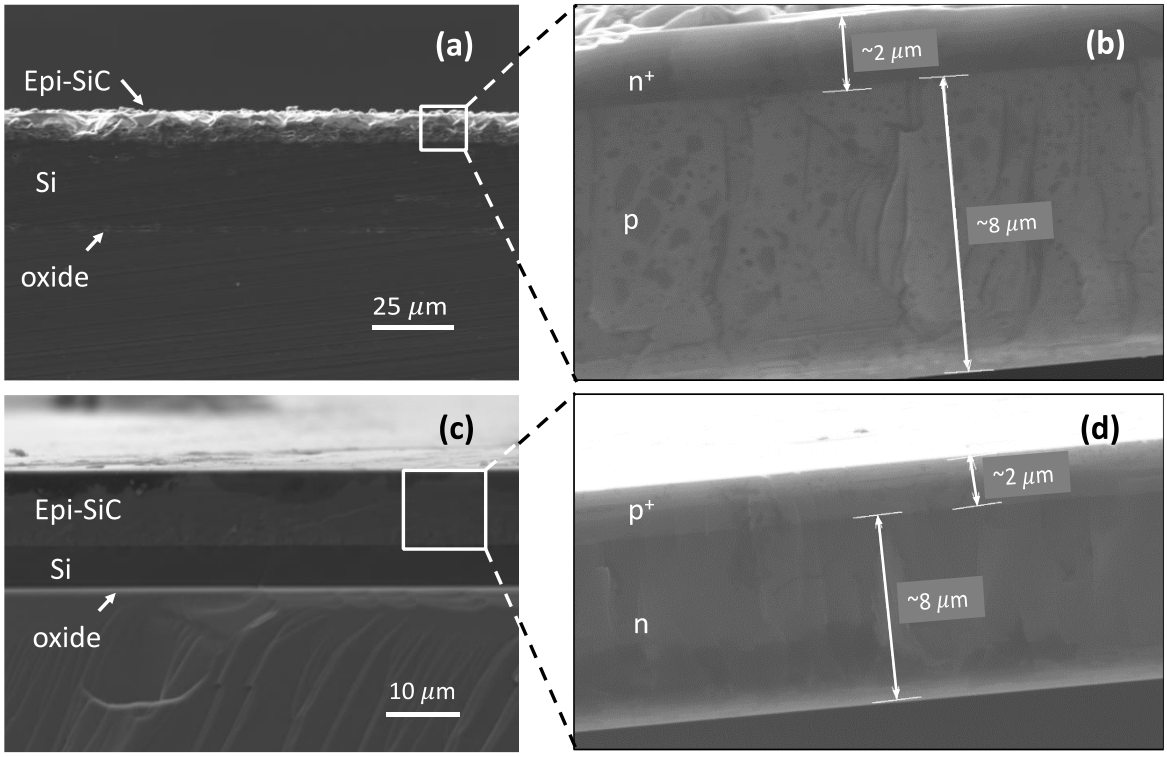

Figure 4.3. Cross section SEM micrographs of the 3C-SiC samples. (a) Cross section view of the n^+/p 3C-SiC on SOI substrate. (b) Free-standing n^+/p sample after etching oxide in HF and Si in KOH solution. (c) Cross section view of the p^+/n 3C-SiC on SOI substrate. (d) Free-standing p^+/n sample.

4.2.2 Birdcage Coil Implementation for 7 T Small Animal MRI

A transmitter/receiver resonator coil that can allow for imaging at ~300 MHz was developed for the MRI experiments. As the birdcage coil is a common resonator coil used for volume imaging [163], this design was chosen for the current work. The length of the birdcage was 150 mm so that it enclosed a full wavelength of the RF signals at ~300 MHz inside a dielectric material (PAA phantom with dielectric constant $\varepsilon_r = \sim 52$). With this length the maximum electromagnetic

coupling happens between the conductive parts inside the coil and the RF signals. In order to have a homogeneous RF field inside the coil and an acceptable SNR at this length, the effective length of the rungs should be shorter. The effective length can be shortened by splitting the rungs and placing capacitors between them. This realizes a hybrid, or band-pass, coil configuration. As a rule of thumb, the length of the rungs may not exceed $\lambda/20$ in order to have an acceptable SNR [109]. Another important factor in designing a coil is the number of the capacitors that is required to build a coil. An optimized design was a hybrid coil with rungs split into two by capacitors. The diameter of the designed coil was 70 mm and it consisted of 12 rungs. The number of the rungs, and the diameter, were optimum values to achieve high SNR values and field homogeneity inside the coil.

Power was fed into the coil through a quadrature configuration on the top end ring. In a quadrature configuration, two ports are physically 90º apart and have a 90º phase difference. Through this configuration a circularly polarized RF field was generated. Impedance matching was performed using a balanced matching circuit with a variable capacitor. Tuning of each channel was also obtained by two variable capacitors placed at 180º and 270º around the top end ring. The details of the implemented coil are presented in Table 4.1.

In order to find values for the capacitors, initially an online application (BirdcageBuilder [164]) was used that estimated the values of the capacitors. Since these values were not accurate, a more accurate model was defined using ANSYS HFSS (19.2, Ansys, Inc. Canonsburg, PA) and Advanced Design System (ADS, 2019, Keysight Technologies, Santa Rosa, CA). First electromagnetic simulations were performed in HFSS and a 36-port S-parameter matrix was imported to ADS. The capacitors and the matching circuits were added to the design with the ideal capacitor and the values calculated using BirdcageBuilder.

A considerable offset was observed in the power reflection and isolation (S_{11}, S_{22} and S_{21}) and the resonance frequency comparing to the values expected. Then using an optimization method in ADS, the values for the capacitors were extracted.

Table 4.1. Birdcage coil resonator specifications for a 7 T small animal bore MRI system.

Coil type	12-leg Band-pass Birdcage Coil
Leg capacitors	1.5 pF
End-ring capacitors	17.5 pF
Tuning Cap	18.5 pF (two trimmers installed on the ports)
ESR Resistance	0.05-0.07 Ω
Matching components	20 pF capacitor & 123.5 nH Inductor
Frequency	~ 300 MHz
Dimensions	Coil-diameter = 70 mm, Length = 150 mm, Leg-width = 6.35 mm (0.25" copper tape), Port-width = 2 mm

However, because we used ideal capacitors, we expected a large offset between the simulation results and experiments. In order to compensate for these mismatches, the ideal capacitors were replaced with realistic capacitor models (Modelithics, Inc, Tampa, FL). Then the coil was built with the dimensions and capacitor values presented in Table 4.1. Figure 4.4 shows both the resonator coil model and the implemented coil.

4.2.3 Modeling and Simulations

As discussed earlier, in the current work different computer simulations were used to both predict the artifacts surrounding various samples and compare them, and also to calculate the specific absorption rate (SAR, W/Kg) and, consequently, any induced heat surrounding the

samples. In this section, details of the Fourier-based simulations used to predict the magnetic perturbation caused by the magnetic susceptibility difference ($\Delta\chi$) between the sample and the tissue phantom (PAA), and the finite element analysis (FEM) simulations to calculate the SAR and the induced heating, are elaborated.

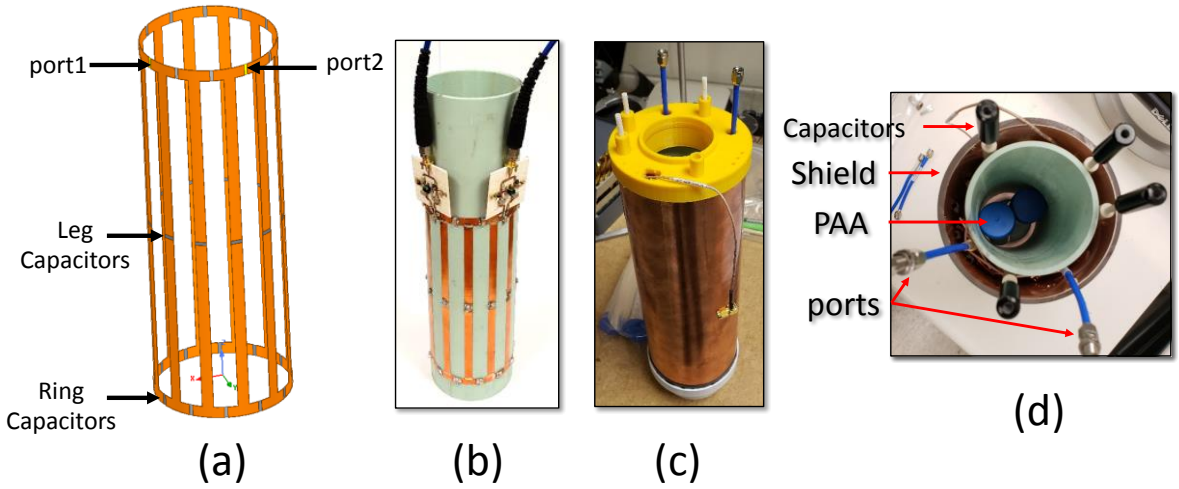

Figure 4.4. The 300 MHz birdcage coil resonator designed and built for MRI experiments. (a) The model used in HFSS for s-parameter calculation. Locations of the ports, the end-ring capacitors and the rung capacitors are indicated with arrows. (b) The implemented resonator without the RF shield. Here the two matching circuits, implemented using surface mount non-magnetic capacitors and inductors, are shown. (c) Fabricated coil with two power ports, two variable capacitors for matching and two for tuning. (d) The top view of the coil without the upper cap. The PAA tubes were used as loads to tune and match the coil using a network analyzer, pre-MRI experiment.

- *Magnetic Perturbation Simulations*

As explained in Section 2.3.11, a Fourier-based method was used and formulated in MATLAB (R2017b, MathWorks, Natick, MA) to predict image artifacts caused by $\Delta\chi$ (MATLAB codes are presented in Appendix D). The MATLAB codes were written based on the method reported in [59], [60]. For simulation purposes, the following were used: Pt film on Si substrate, 3C-SiC free-standing sample, and Si substrates (n-type and p-type). The background material in

which the samples were placed in was the PAA tissue phantom. The magnetic susceptibility of these materials was provided in Table 2.1 (Chapter 2). These were the main materials whose artifacts were observed via experiments under 7 T MRI excitation. Using these simulations, $\mathbf{B_0}$ perturbation caused by each material of interest was predicted. The magnetic interaction between a stack of layers was not captured in these simulations, but rather they were experimentally measured. By combining the simulation and experimental results, one can better understand the artifacts patterns occurring in MRI experiments. The experiments also helped verify and validate the numerical models, a very important point as direct measurement of minute temperature rise in the tissue phantom was not possible due to resolution limits of available temperature probes.

In these simulations, $\mathbf{B_0}$ was set to 7 T, the field of view (FOV) was 256 × 256 × 256 pixels, length and width of the samples were 150 mm and 40 mm, respectively, and the voxel size was 1 mm × 1 mm × 1 mm. More details about implementation of the codes and variables can be found elsewhere [165].

- *Finite Element simulations*

One essential benefit of simulations is to control all aspects of a physical phenomenon which is often not possible during actual experiments. In the current work, the goal of these simulations was to compare the SAR distribution surrounding the various materials under 7 T MRI excitation. However, since the length of the samples are short in comparison with the wavelength of the RF fields inside the tissue phantom, the electromagnetic coupling consequently was reduced which, as a result, decreases the induced heating effect. The induced heat is thus expected to be very low and not measurable during actual experiments. Although low in intensity, the heat may increase dramatically if the length of the samples becomes comparable to the wavelength of the

RF signals inside the MRI. This can also be modelled using FEM simulations after validation of the numerical models.

ANSYS HFSS (19.2, Ansys, Inc., Canonsburg, PA) was used to perform FEM electromagnetic simulations. Via these simulations the electromagnetic coupling between the $\mathbf{B_0}$ field and the Pt and 3C-SiC samples was modelled. For simulation purposes, a high-pass birdcage resonator with 16 legs was placed around a 70 mm diameter and 150 mm long cylinder, tuned at ~300 MHz as designed previously in HFSS. The Pt and 3C-SiC samples (Figure 4.2 (b), (c)) were placed inside a tube using a 3D printed polyacrylic acid (PLA) holder. The tube was filled with the PAA tissue phantom. This was also modelled in ANSYS HFSS as illustrated in Figure 4.5. The electromagnetic simulation error was set to $\Delta S < 0.01$, which guarantees negligible errors in the calculation of Maxwell's equations. After mesh generation, each part of the model was individually inspected to ensure a good quality mesh. The simulations were run on the advanced computing resources at the University of South Florida which provided 5 × 64 GB of RAM and 24 CPU cores (2x Intel® Xeon® CPU E5-2650 v4 @ 2.20GHz). The electromagnetic simulations were done in ~3 hours.

Another FEM electromagnetic simulation without the sample was done to validate the simulation results using the experiments under a 7 T horizontal magnet (Agilent-Technologies) and Bruker electronics (BioSpec AV3HD). The results of the electromagnetic simulations were then connected to thermal simulations in ANSYS Workbench™ and ANSYS Mechanical™ to measure the temperature rise inside the tube and compare it with the experimental results to validate the simulations.

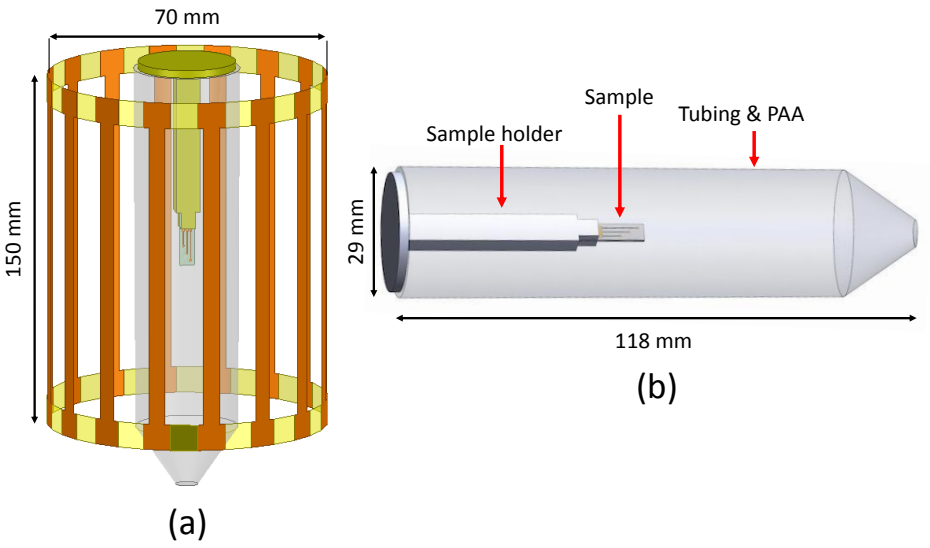

Figure 4.5. Illustration of the models used in ANSYS HFSS for electromagnetic and thermal simulation. (a) High-pass birdcage designed for the simulations. This birdcage resonator has 16 rungs and tuned to ~300 MHz. (b) shows the sample tube that is filled with the PAA tissue phantom and a 3D-printed PLA holder that holds the sample inside the tubing.

4.3 MRI Experiments

In order to validate the computer simulations, multiple experiments were designed for a 7 T MRI machine for small laboratory animals (7 T horizontal magnet (Agilent-Technologies) and Bruker electronics (BioSpec AV3HD)) in the Moffit Cancer Center. Two different sets of experiments were conducted to measure both any image artifacts and induced heating under MRI excitation. The experiments were performed using the samples fabricated as described in the previous sections which were inserted into a saline gel (i.e., PAA) used as a human tissue phantom. In the following sections, the recipe to make the phantom, and the two sets of MRI experiments, are elaborated upon.

- *Saline Gel Phantom Preparation*

As mentioned earlier, a saline gel was used as the tissue phantom that simulates the electrical, thermal and magnetic properties of human brain tissue. In order to accurately achieve

the properties of human tissue, the synthesis was exactly and carefully followed according to the relevant standards [56]. The phantom was made by mixing polyacrylic acid (PAA, Sigma-Aldrich, St. Louis, MO, USA) and pure NaCl (reagent grade, purity >99%) dissolved in distilled water. The ratio of NaCl and water was set to 1.32 g/L, while the value for PAA and water was 10 g/L. The electrical conductivity of the phantom can be adjusted by changing the ratio of NaCl to water, and by changing the ratio of PAA to water the dielectric constant of the phantom may be changed. The electrical conductivity and dielectric constant of the mixture were measured using a network analyzer (Keysight, Santa Rosa, CA, USA) and a dielectric probe. The setup used to measure the electrical properties of the phantom is shown in Figure 4.6. The measured electrical conductivity of the phantom at 25 ºC and a frequency of 300 MHz was $\sigma \approx 0.5$ S/m and its relative dielectric constant was $\varepsilon_r \approx 70$. According to the applicable standards [56] this recipe should result in a diffusivity of 1.3×10^{-7} m^2/s and a heat capacity of 4,150 J/Kg-C, which are the thermal properties of the human tissue. 500 mL of this phantom was made, carefully stirred and refrigerated in a sealed container for future use. Each time before use, the phantom was carefully stirred to remove any lumps inside the mixture.

- *MRI Experiments to Measure Image Artifacts*

Multiple samples were fabricated to measure image artifacts under 7 T MRI scans as mentioned in Section 4.2.1. The apparatus used for image artifact measurement is shown in Figure 4.7. The setup consisted of a plastic tube that was filled with the PAA saline gel. A 3D-printed polylactic acid (PLA) holder was used to place the sample inside the plastic tube. The holder was glued to the screw cap of the tube. The sample was also glued to the holder. The cap was carefully tightened, checked for the absence of air bubbles, and the tube was placed inside the MRI bore for the experiments. The samples were tested individually in each MRI scan.

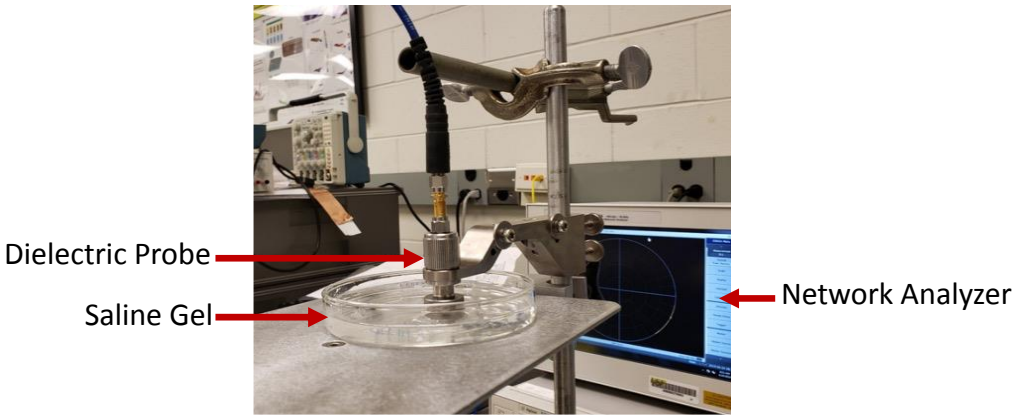

Figure 4.6. The setup used to measure the electrical conductivity and dielectric constant of the tissue phantom. The saline gel phantom was made by mixing polyacrylic acid (PAA) and pure NaCl (reagent grade, purity >99%) dissolved in distilled water. The ratio of NaCl and water was set to 1.32 g/L and the ratio for PAA and water was 10 g/L. The measured electrical conductivity of the phantom at 25 ºC and 300 MHz was $\sigma \approx 0.5$ S/m and its relative dielectric constant $\varepsilon_r \approx 70$.

The following MRI sequence was used for image artifact measurement. A similar sequence was used for all the samples tested for image artifacts, while the location of the tubes was carefully inspected to ensure consistent placement in the coil during measurement. T2 axial and coronal images of the devices was obtained with a RARE (Rapid Acquisition with Relaxation Enhancement) sequence with TR/TE 2220/32ms, 9 slices, with the slice thickness of 0.3 mm. The FOV of the sequence was 35 mm × 35 mm and with 256 × 256 pixels.

- *MRI Experiments to Measure Induced Heat*

Another set of MRI experiments was designed to measure the induced heat surrounding the test samples. As mentioned earlier, for these experiments samples with three electrodes were used. However, the induced heat was very low and measuring it very difficult. For this reason, two extended SS wires were soldered to the electrodes to increase the physical length of the electrodes and, thus, the RF field electromagnetic coupling to the electrodes inside the MRI tool.

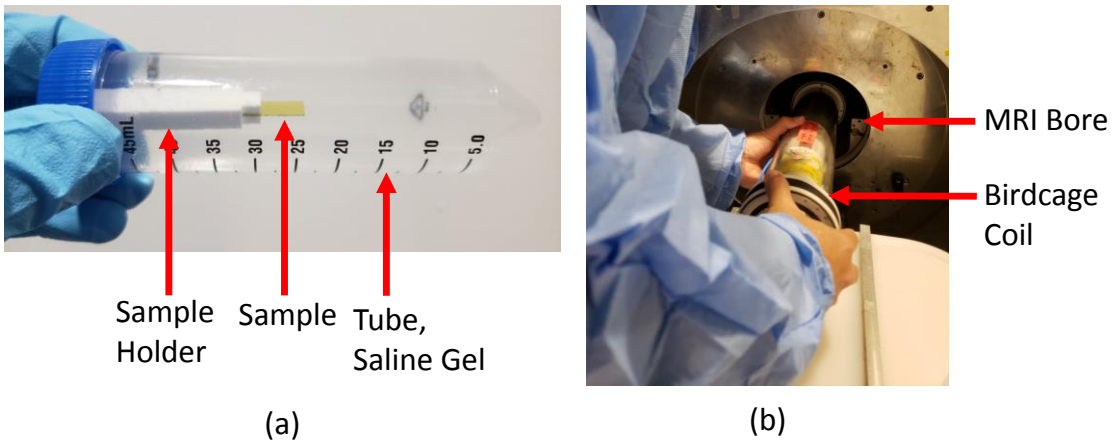

Figure 4.7. Apparatus used to measure image artifacts under MRI excitation. (a) Plastic tube filled with saline gel phantom and the sample with 3D-printed polylactic acid (PLA) holder used to hold the sample in place. The holder was glued to the screw cap and the sample to the PLA holder. (b) Coil insertion into the MRI bore used for all MRI experiments.

Overall, accurate measurement of induced heating is very laborious as there are multiple factors that might influence heat generation and distribution inside the MRI [56], [151]. For this reason, FEM simulation is an alternative strategy that offers higher precision observation of the relevant physical phenomena and, if validated by a simple experimental setup, very complex problems can be analyzed using this method. Therefore, in the current work, we took advantage of accurate electromagnetic and thermal numerical simulations to predict the SAR (W/Kg) distribution surrounding the electrodes. In addition, two MRI experiments were conducted to validate these simulations and to predict the expected maximum temperature rise in the sample with the highest electrical conductivity (i.e., Pt). The thermal and electrical properties of the materials used for these simulations and experiments are presented in Table 4.2.

The setup that was used to measure the induced heating was very similar to the one used for image artifact measurement, except the holder was designed to encompass two fiber-optic temperature sensors (SA Instruments, Inc., Stony Brook, NY, USA) One of the fiber-optic sensors

was in the vicinity of the longest of the three electrodes on the sample to measure the temperature rise surrounding the tip region and the other sensor was placed further away from the sample, closer to the inner wall of the plastic tube, to measure the temperature rise inside the PAA saline gel phantom. The setup used to measure the temperature inside the plastic tube is shown in Figure 4.8.

Table 4.2. Properties of materials used to calculate MRI induced heating.

Material	**Electric Conductivity ($\times 10^6$ S/m)**	**Thermal Conductivity (W/m-K)**
Human Tissue	0.5×10^{-6}	0.4
Doped SiC (~10^{19} dopants/cm^3)	~ 0.17	360
Doped Si (~10^{18} dopants/cm^3)	~ 0.1	148
Platinum	9.3	71

The following MRI sequence was used for these experiments. Each scan was 15 minutes long so as to give enough time for heat accumulation. The T2 axial and coronal images of the devices were obtained with a RARE (Rapid Acquisition with Relaxation Enhancement) sequence with TR/TE 425/12 ms, 11 slices, with the slice thickness of 0.5 mm. The FOV of the sequence was 30 mm × 30 mm and with 256 × 256 pixels.

4.4 Results

In this section, S-parameter values for the birdcage coil, the simulated and experimental results indicating image artifacts for the various samples, and the simulated and experimental results showing the induced heat and SAR for the various samples tested and simulated are elaborated. Although the birdcage coil built in this work was not ultimately utilized in the

experiments due to insufficient SNR, the experimental results are presented for the future improvement. Furthermore, the simulated and experimental results specifying the difference between MRI compatibility of the materials used are compared.

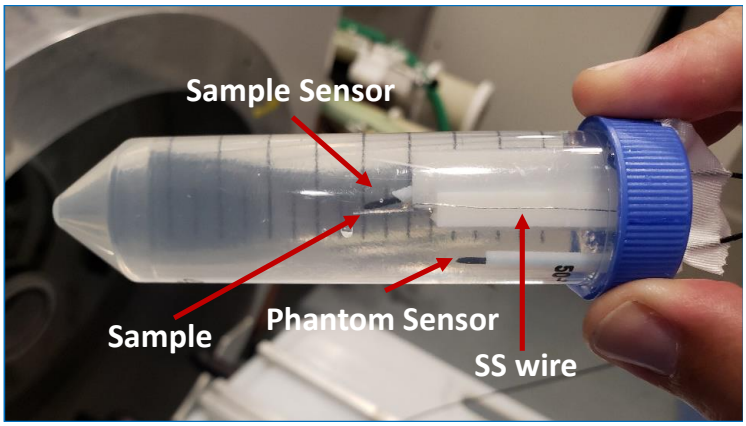

Figure 4.8. Photograph of the sample and holder used to measure the temperature rise surrounding a Pt sample with 3 electrodes and two extended stainless-steel (SS) wires soldered to the electrodes. Two fiberoptic temperature sensors were used for temperature measurement. One placed in the vicinity of the long electrode on the sample to measure the temperature rise at the tip and the other further away from the sample, closer to the inner wall of the plastic tube, to measure the temperature rise inside the PAA-saline gel phantom.

4.4.1 Birdcage Coil

As discussed earlier in this chapter, the birdcage coil designed was a 16-rung hybrid birdcage tuned at ~300 MHz for use in the 7 T MRI machine for small laboratory animals. Before the coil was tested in the MRI machine, the S-parameter characteristics for both loaded and unloaded conditions was measured. Two plastic phantom tubes, similar to the ones used for the MRI experiments, were filled with the saline gel and used as loads to tune and match the resonator coil, as shown in Figure 4.4 (d). First, the frequency response of the coil was simulated in HFSS and ADS. Using this method, power reflection and isolation between ports were simulated and the

S-parameter plotted as shown in Figure 4.9. These plots show 9 resonance frequencies, one of which is the resonance of the end-rings. The other 8 resonances belong to loops that the rungs are built from. The last resonance frequency is the end-ring resonance and the one before this resonance frequency is the actual resonance frequency which was set to 300 MHz. Therefore, this particular resonance frequency needs to have very low power reflection (i.e., $S_{11} \leq 20$ dB) and also very low transmitted power between two ports to be able to isolate the ports at the frequency of interest.

After tuning and matching the resonance frequency of interest in software, and after the optimum capacitor values were calculated, the coil was built. To test for reflected power and port isolation, a network analyzer was used. The test was done with and without saline gel loads to fine-tune the loaded and unloaded coil, respectively. S-parameters for reflected power for the two ports (S_{11}, S_{22}) are shown in Figure 4.10.

As shown in Figure 4.10, a load can distort resonance coil tuning and matching at the frequency of interest. The resonance frequency was not exactly 300 MHz, as prior tests had shown a ~1.5 MHz offset when the coil was placed inside the MRI bore. This frequency offset could be due to coupling of the coil with the MRI magnets. The offset was observed even when a copper shield was used around the coil. Thus the coil was re-tuned and re-matched prior to use in the MRI machine.

4.4.2 Image Artifacts

Image artifacts reduce image quality during MRI analysis and may be caused by interactions between the sample and the B_0 and B_1 fields. The samples prepared previously were placed inside the 7 T MRI machine and the coronal and sagittal images from the samples were

obtained. The image artifacts can extend a noticeable distance in all the directions surrounding the sample. They can be either dark or bright depending if $\Delta\chi$,which is the difference between the tissue phantom magnetic susceptibility and the sample magnetic susceptibility, is less than zero or greater than zero. Also, other phenomenon may play a role in determining the severity and contrast of image artifacts, such as the interaction between the sample conductive parts and B_1 field. This may lead to B_1 distortion surrounding the sample.

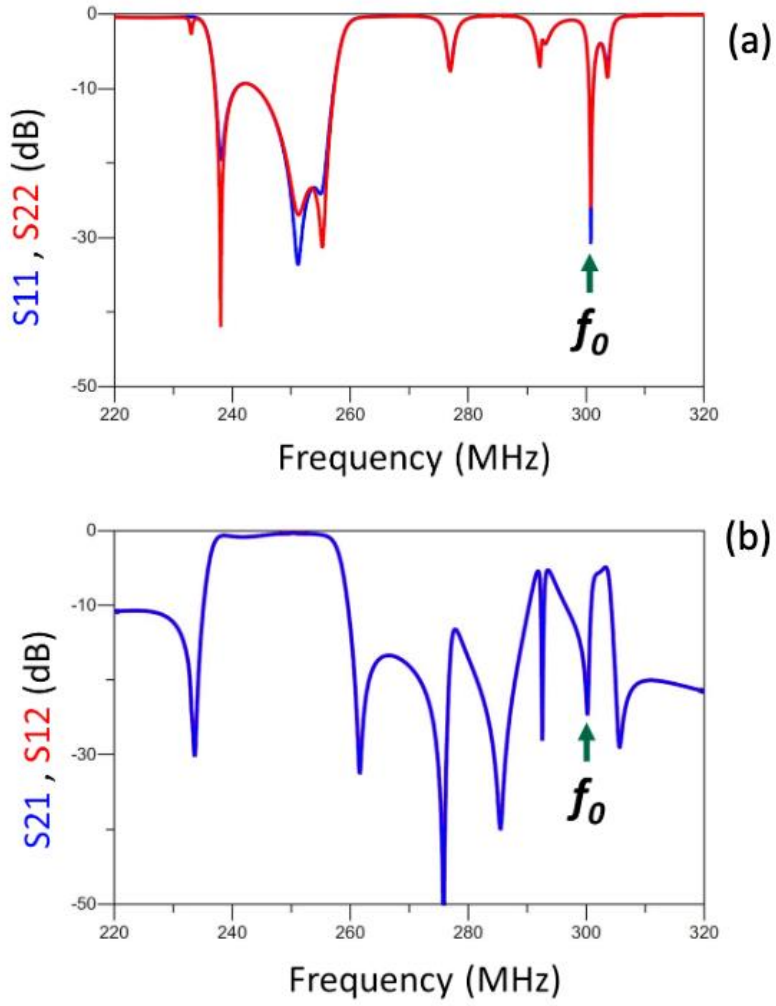

Figure 4.9. Simulated S-parameters using HFSS and ADS showing the power reflection (S_{11} and S_{22}) and isolation (S_{21}, S_{12}) between two ports on the RF coil. In these plots f_0 shows the main resonance frequency of the hybrid birdcage coil. (a) Reflected power of the two ports indicating that the ports are nearly symmetric. (b) Transmitted power between the ports. At f_0 , the reflected power (S_{11}) is below -25 dB which is suitable for the birdcage resonator.

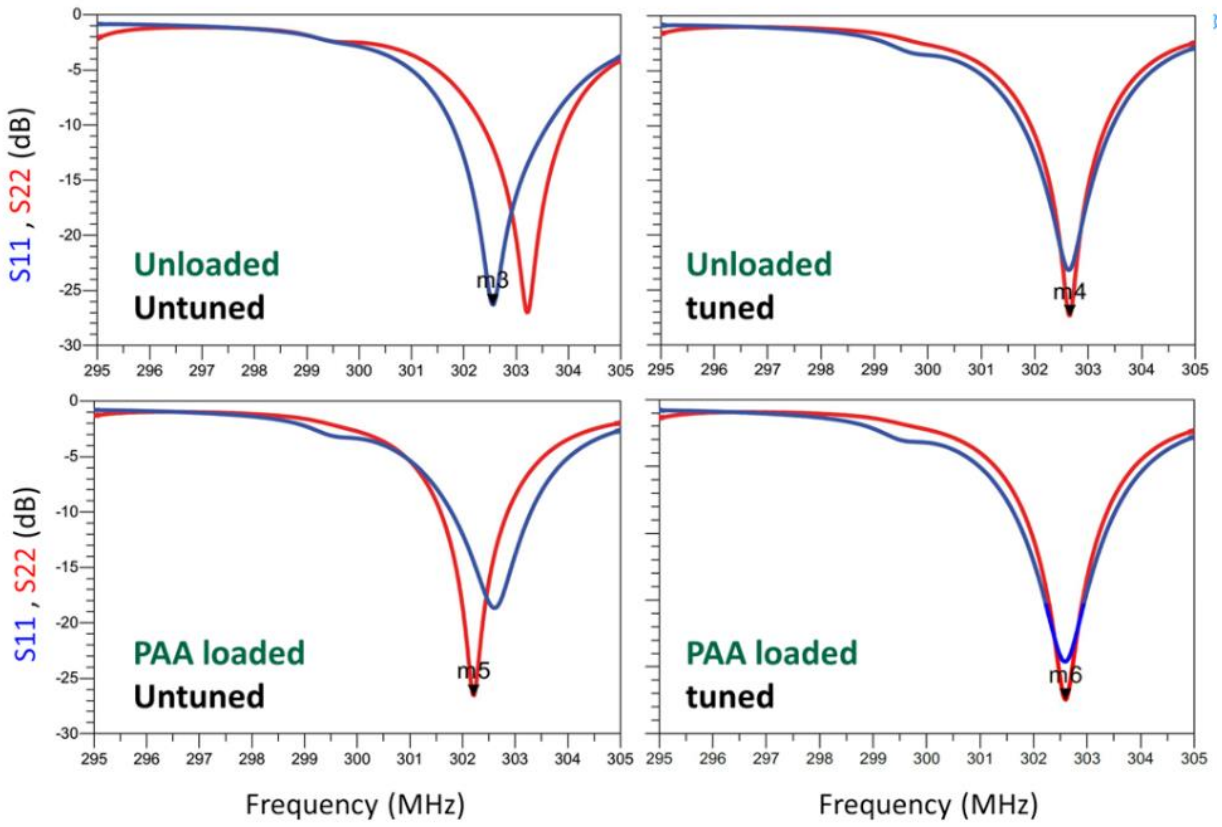

Figure 4.10. Measured S-parameters indicating reflected power at the resonance frequency of interest. The resonance was not accurately set at 300 MHz, due to frequency offset caused by magnetic coupling inside the MRI bore. Two saline gel (PAA) tubes were used as loads in order to tune and match the coil prior to use in the MRI tool. (a) Reflected power values for the two ports in the unloaded coil before tuning. (b) Reflected power in the unloaded coil after tuning and matching with a 50-Ω impedance load. (c) Tuned and matched coil after loading with saline gel (PAA). (d)Tuned and matched loaded coil.

Fortunately, the influence of these two phenomena can be distinguished via numerical simulations. The simulations, then, can be compared to the MRI experimental data for a better understanding of the interactions involved. The Fourier-based simulation results that estimate B_0 field perturbation due to $\Delta\chi$ are shown in Figure 4.11. The results indicate a shift in the B_0 field. As expected, regarding the χ for SiC in comparison with Pt and Si, the 3C-SiC sample displayed

a lower amount of B_0 field distortion surrounding the sample while Pt displayed the highest. The minimum ΔB_0 was ~ -0.3 μT in 3C-SiC and the maximum ΔB_0 was ~100 μT in the Pt sample.

The Results of the MRI experiments are presented in Figure 4.12. As observed in this figure, all the materials, except the 3C-SiC, showed an extended image artifact surrounding the samples. The 3C-SiC samples were almost invisible in the MRI images as seen in the figure. The image artifacts covered the whole device and distorted the shape of the sample. However, for the silicon substrates the severity of the image artifacts was also related to the doping type and also concentration. This can be seen for the p-type Si substrate, which did not show any extended image artifacts caused by magnetic field distortion. This will be discussed more in the discussion section.

4.4.3 Induced Heat and SAR

As mentioned previously, in order to estimate induced sample heating we must take advantage of FEM simulations. This is because the samples are small in size, resultin in a minute temperature rise. However, as the size of the samples becomes larger and larger (relatively large in comparison to the wavelength inside the dielectric material), so does the SAR and induced heating. Therefore, these results can be used as a reference that compares the SAR and induced heating in the materials of interest despite their small dimension.

In order to validate the simulations, the temperature inside the saline gel phantom (no samples present) was measured using the fiberoptic temperature probes. Then, these results were compared with the simulation results for this setup. While the value of the measured B_0 at the isocenter of the coil with the saline gel load was ~29 μT, this value in the simulations was ~20 μT. This can be due to a different coil used for the simulations and the experiments and also the quality

of the simulation mesh. The measured and estimated results for the temperature rise for an MRI scan duration of 15 minutes is presented in Figure 4.13.

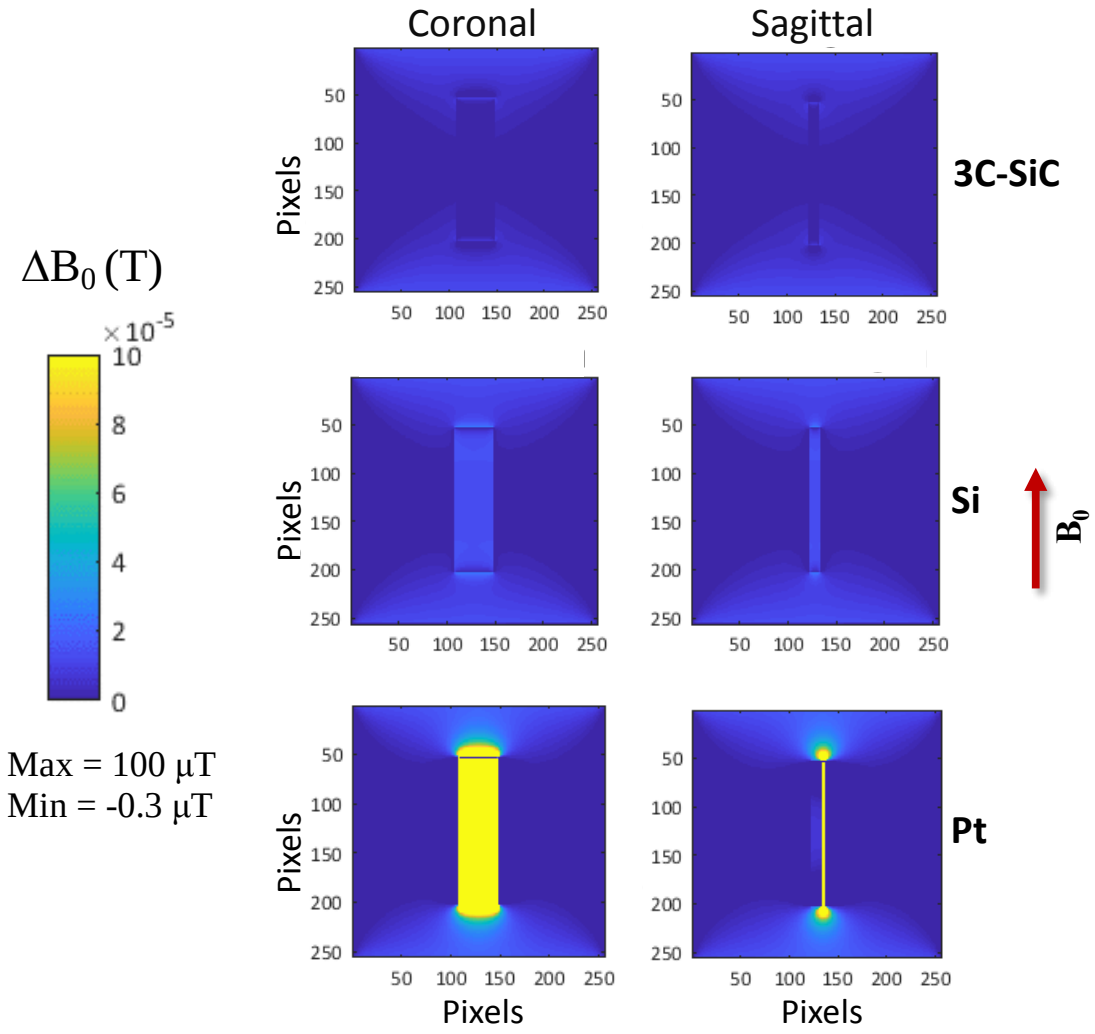

Figure 4.11. The results of the Fourier-based simulations to calculate the image artifacts caused by magnetic susceptibility difference ($\Delta\chi$) between the saline gel phantom and the material used for the experiments. Two coronal and sagittal views of each sample are presented. The red arrow shows the direction of the static magnetic field (B_0). The minimum and maximum magnetic field shift caused by $\Delta\chi$ in the materials used for these simulations were ~ -0.3 μT and ~ 100 μT, respectively. The lowest simulated B_0 field distortion was observed in 3C-SiC material and the highest in Pt. This is due to the negligible $\Delta\chi$ between the saline gel phantom and the 3C-SiC material.

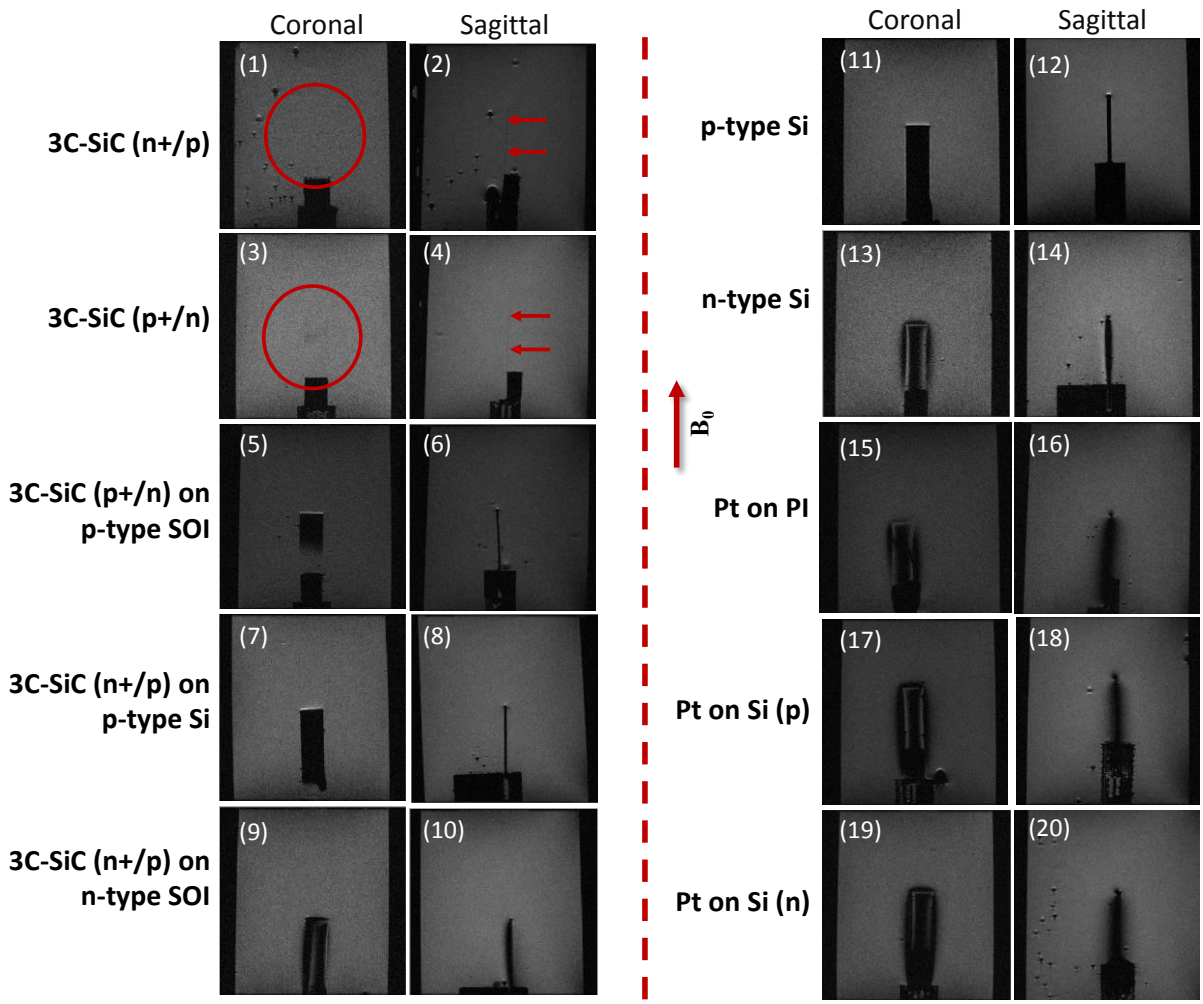

Figure 4.12. 7 T MRI experimental scan images indicating the intensity of the image artifacts in the samples previously developed. The direction of the B_0 filed is shown with the arrow in this figure. (1) shows the coronal view of the 3C-SiC sample (n^+/p). This was a free-standing sample released after HF and KOH etching, therefore there was no Si substrate on this sample. As seen, this thin sample (~10 µm) was almost invisible in the scans. This is also true for the sagittal view of the similar sample (2). Similarly, the 3C-SiC sample (n^+/p) did not display any footprint in the scans (3,4). The image artifacts were minimum for all 3C-SiC samples grown on p-type Si substrates (5-8). However, all of these samples were visible in the MRI scans when the Si substrate remained on the sample. On the other hand, 3C-SiC samples grown on n-type Si created image artifacts when the Si substrate remained on the sample (9,10). Opposite to the p-type Si substrate (11,12) that did not show any image artifacts, the n-type Si substrate generated a comparatively high image artifact (13,14). All the Pt samples showed severe image artifacts, regardless of the substrate that they had deposited on (15-20).

The initial temperature of the phantom was 27.4 ºC and, after 15 minutes of MRI exposure, the temperature in the middle of the tube, where the sample was attached in the other experiments, increased to 29.1 ºC. By way of comparison the estimated value from FEM simulation was 29.08 ºC, as shown in Figure 4.13 (b).

The next set of simulations were performed to estimate the SAR distribution around each electrode for the three electrode samples. The results for the FEM simulations indicating the SAR_{1mg} distribution in two Pt and 3C-SiC samples are shown in Figure 4.14.

As expected and shown in Figure 4.14, the highest SAR_{1mg} values occurred at the sample extremities where the electric current flows out of the electrodes. However, the hot spot area in the 3C-SiC sample showed less intensity comparing to the Pt sample. While the estimated SAR_{1mg} was very low in both cases, if the size of the electrodes are scaled up the SAR_{1mg} values also increase. The SAR_{1mg} value for 3C-SiC showed ~30% reduction comparing to the Pt sample. This value is reduced further if the thermal conductivity of materials is taken into account.

One of the MRI experiments performed to measure the induced heating was on the Pt sample with the extended SS wires. The main purpose of this measurement was to measure the temperature rise in the sample and connect the measured temperature rise to the estimated simulated SAR values. The Pt sample was chosen for this measurement as Pt was expected to induce more heating than 3C-SiC. The Pt induced enough heat so that the fiberoptic probes were able to measure the temperature rise accurately. In addition, another set of FEM electromagnetic simulations were conducted on the same Pt sample to connect the measured data to the simulation. Similar simulations were performed on the 3C-SiC sample with extended SS wires to compare the results with the Pt sample. The results are illustrated in Figure 4.15. As expected the difference in the maximum temperature rise for the Pt and 3C-SiC samples was negligible (Figure 4.15 (a,b)).

The negligible difference in the temperature rise occurred because the highest amount of electromagnetic coupling happened in the SS wires, as they were longer than the electrodes (and identical SS wires were soldered to both samples).

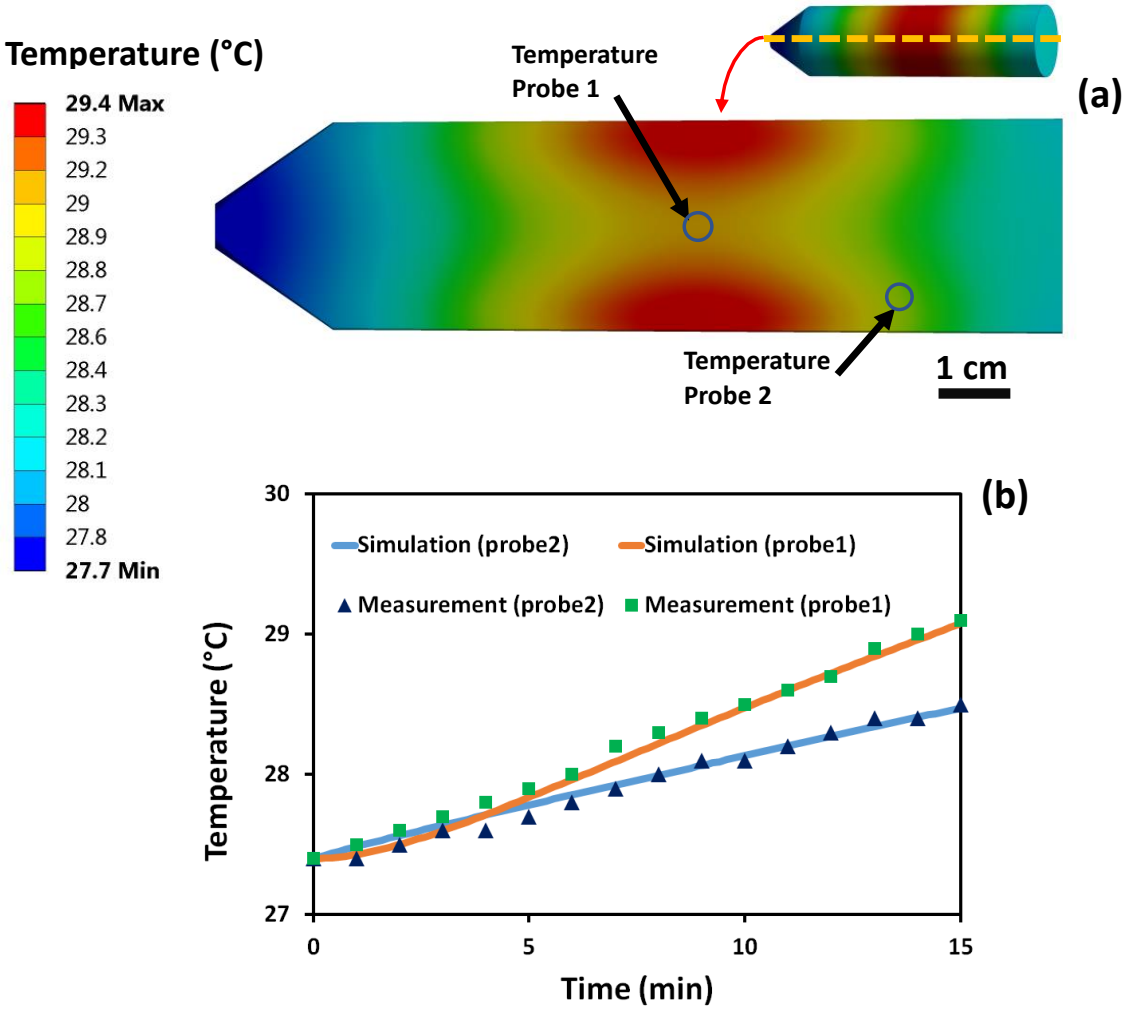

Figure 4.13. Measured and simulated gel phantom temperature rise without any samples present. (a) Cross section view of the simulated tube temperature profile after 15 min of exposure to ~300 MHz RF field excitation. (b) Measured and simulated temperature profiles at probe 1 (probe tip) and probe2 (tissue phantom) locations. Initial temperature 27.4 ºC, and after 15 min exposure to MRI scan it increased to 29.1 ºC at probe 1 location and to 28.5 ºC at probe 2 location. Estimated FEM simulated value at probe 1 location 29.08 ºC and at probe 2 location 28.47 ºC which is in a very good agreement with experimental results.

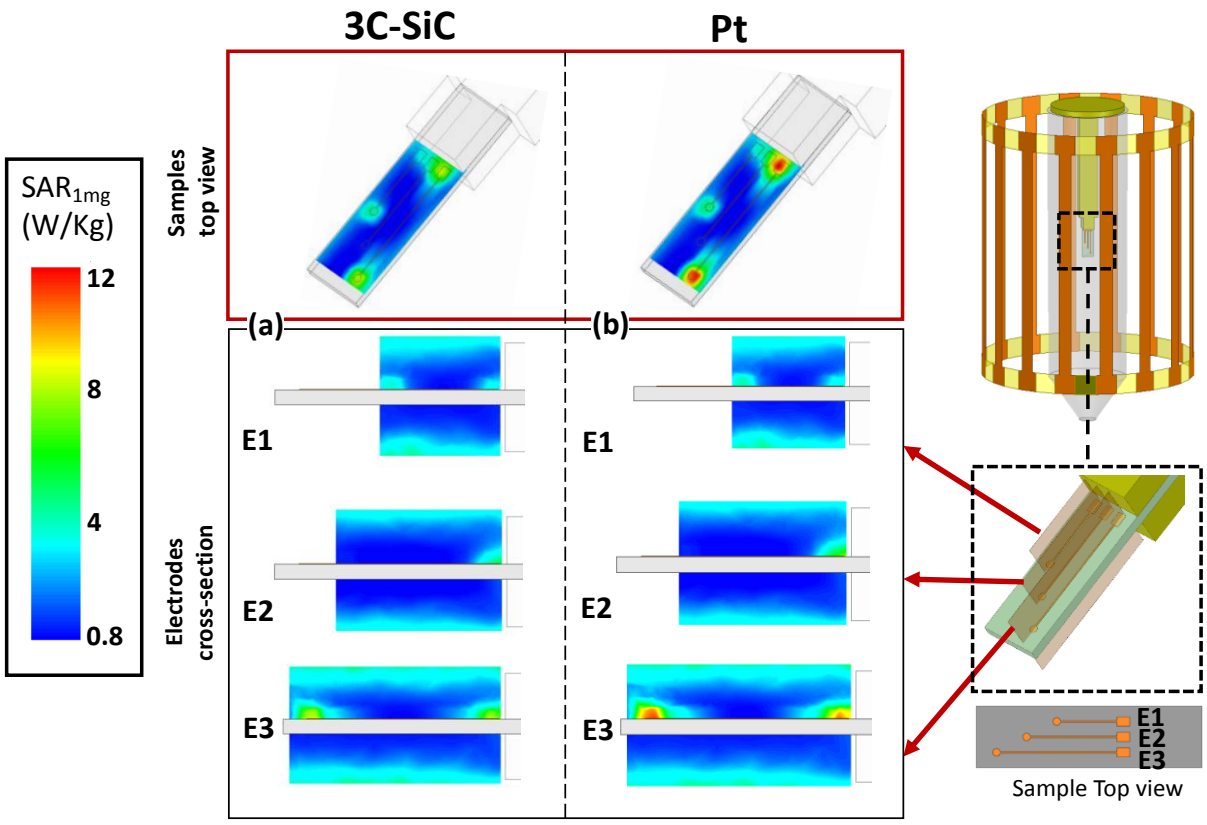

Figure 4.14. Estimated SAR_{1mg} around the three Pt and 3C-SiC electrode samples. E1 stands for the shortest electrode, E2 for the middle electrode, and E3 for the longest electrode. (a) Estimate SAR_{1mg} results for 3C-SiC via FEM electromagnetic simulations in ANSYS HFSS. Both the top view and cross-section view for each electrode is illustrated. The maximum estimated SAR for the 3C-SiC sample appeared at the tip of the longest electrode (SAR_{1mg} ~8 W/Kg) while the averaged B_1 at the coil isocenter was ~20 µT. (b) Estimated SAR_{1mg} distribution the Pt sample. Maximum SAR_{1mg} estimated to be ~12 W/Kg and occurred at the tip of the longest electrode. These results indicate a ~30% reduction in the maximum SAR_{1mg} for 3C-SiC comparing to Pt.

The temperature measurement at the tip of the E3 electrode on the Pt sample is shown in Figure 4.15 (c). This plot shows the normalized temperature rise, that is, the difference between the temperature measured with probe1 in Figure 4.13 (a) and the temperature measured with the probe2. In addition, the temperature measurement results for the saline gel, when no sample was present, are also shown in this plot. A higher slope for the wired-Pt sample indicates a faster increase in temperature during the time of MRI exposure.

4.4.4 3C-SiC Neural Probe under 7 T MRI

For this experiment the fabricated 3C-SiC probe was glued to the PLA holder and placed inside the plastic tube along with the saline gel phantom. The same MRI sequence used for measuring the image artifacts was used in this case. The setup and the sagittal and coronal images of the probe are shown in Figure 4.16.

4.5 Discussion and Summary

In this chapter, the magnetic resonance compatibility of single crystalline cubic silicon carbide (3C-SiC) probes was evaluated. In this work, it was hypothesized that a brain implant fabricated monolithically from 3C-SiC material may remarkably improve MRI compatibility of these implants. Most importantly, the 3C-SiC implants may allow for an increase in the standard B_0 intensity which would permit the use of implants in 7 T MRI tools. Therefore, in order to evaluate the MRI compatibility of 3C-SiC neural implants, a 7 T MRI machine for small laboratory animals was used in this work. Silicon, of various doping type and concentration, and platinum were used as reference materials to compare the MRI compatibility of 3C-SiC material to. The MRI compatibility criteria in this work was limited to the severity of image artifacts surrounding the samples and induced heating and SAR distribution under MRI scans. Various samples were fabricated from 3C-SiC, Si, Pt and Polyimide (PI). Si and PI were mainly used as the substrate to deposit Pt on, while Si and SOI were used to grow thin epitaxial films of 3C-SiC on.

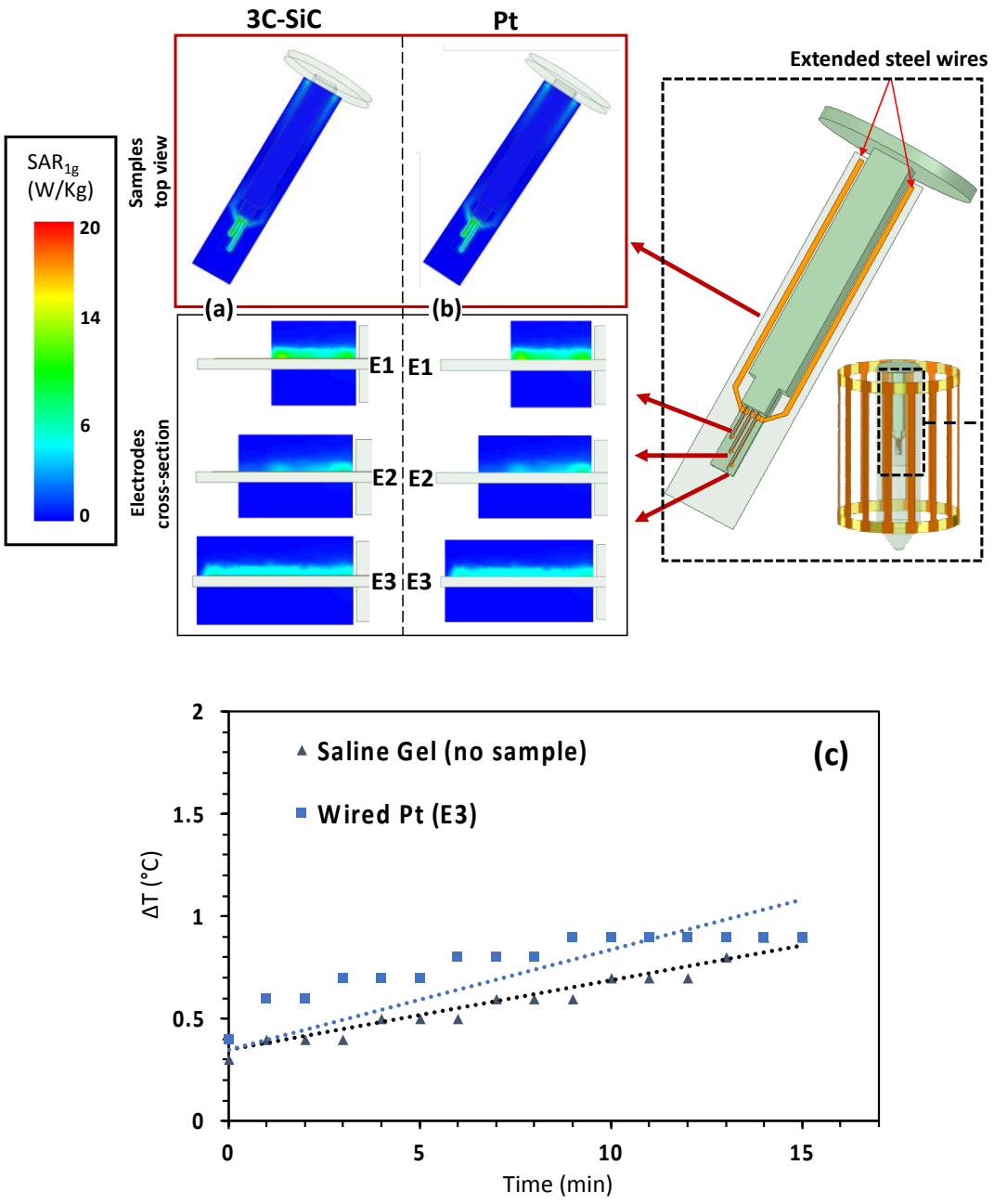

Figure 4.15. Temperature measurement and FEM electromagnetic simulation results for the samples with extended SS wires. (a) SAR_{1g} for the 3C-SiC sample with extended SS wires. (b) SAR_{1g} for the Pt sample with extended SS wires. The maximum SAR_{1g} values for the two samples were approximately identical as the highest amount of electromagnetic coupling happened in the SS wires, as they were longer than the electrodes. (c) Measured temperature at the tip of the E3 electrode on the Pt sample. Plot shows the normalized temperature rise, that is, the difference between the temperature measured with the probe1 and probe2. Temperature measurement for the saline gel, when no sample was present, are also shown.

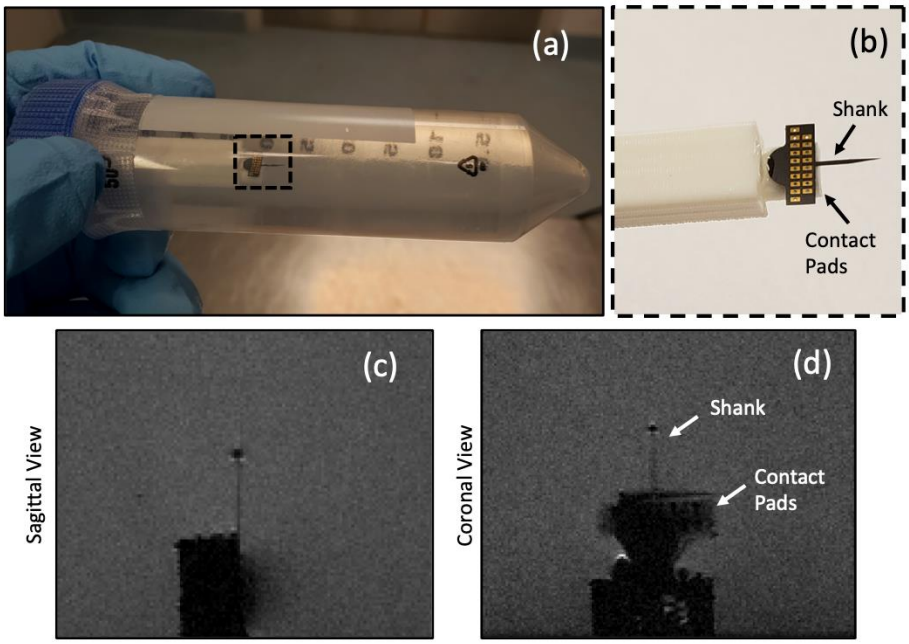

Figure 4.16. MRI scans of the fabricated 3C-SiC probe under 7 T MRI scanning. The same MRI sequence used for image artifact analysis was used in this experiment. (a) Photograph of experimental setup consisting of PLA holder, plastic tube, saline gel phantom and the neural probe. (b) A close-up image of the 3C-SiC neural probe glued on the PLA holder. (c) sagittal view of the neural probe under 7 T MRI. The tip of the probe showed a circular image artifact. (d) coronal view of the neural probe. The shank generated less image artifacts than the pads, due to the metallic pads which would be outside of the brain during probe use and is not an issue.

A plastic tube filled with saline gel phantom, consisting of a mixture of PAA, pure NaCl, and distilled water, was used as the human brain tissue phantom for MRI evaluation. The samples were tested under MRI scanning to observe any image artifacts generated by each sample and the corresponding induced heating. Electromagnetic and thermal numerical simulations, based on finite element method (FEM) in ANSYS Multiphysics, as well as Fourier-based susceptibility induced B_0 field shifts formulated in MATLAB, were used to estimate the SAR distribution, induced heating and magnetic field perturbation (image artifacts) surrounding the samples. Finally, the fabricated 3C-SiC neural probe presented in Chapter X was tested in a 7 T small animal MRI machine at the Moffit Cancer Center to measure the image artifacts surrounding the probe.

In addition, a hybrid birdcage resonator transmitter/receiver coil for the 7 T small animal MRI was designed, fabricated and tested. Although electromagnetic and circuit simulations, along with S-parameters tests using a network analyzer showed acceptable RF performance, low SNR within the MRI coil was observed. Therefore this coil was not used for the actual MRI experiments. The main purpose of implementing the coil was to perfectly align the simulations with the experimental setup for this work. This was necessary since commercial coils contain proprietary design features that are both unknown to the user and very complicated to replicate. Despite these challenges measured and simulated results showed adequate agreement to support our hypothesis that 3C-SiC neural probes are compatible with 7 T MRI tools and likely worth further technical development.

The birdcage coil used for the MRI experiments was a commercial birdcage coil (Bruker) for laboratory mice. To support the presented simulations, another birdcage coil was designed that was of a different design but produced similar MRI scan images to the actual coil. This implies that the B field distributions were logically similar thus allowing for reasonable comparison of simulated and experimental data. In order to ensure both birdcage coils resulted in similar SAR distributions in the saline phantom, the B_1 field map in the isocenter of the coil, when loaded with the phantom, was measured and simulated. In HFSS, the input power driving each port was adjusted so that the same B_0 field map was obtained. In addition, the induced heating inside the phantom (without the sample) was measured in two locations and the results were compared with their corresponding simulations. The measured and simulated induced heating were within 2% of each other. After tuning the commercial coil using the measured temperature and B_1 map, the extracted values were fed back into the electromagnetic and thermal FEM simulations to achieve the closest possible fit to the data.

As mentioned earlier, the phantom that was used in this work was made of polyacrylic acid (PAA) and purified NaCl (>99%) dissolved in distilled water. The ratio for PAA/water and NaCl/water was followed from a standard model [56]. This phantom mimicked the thermal, electrical and magnetic properties of human brain tissue. Although the phantom was carefully stirred during the process to avoid lumps and air bubbles, very tiny air bubbled were formed during the MRI scans in some of the samples. It was suspected that these bubbles were formed due to imperfect sealing that was used for a few of the samples. However, it is believed that the formation of a few little bubbles did not influence the final results as they were observed to be further away from the samples and out of the field of view (and distant from the temperature probes).

In order to estimate the image artifacts caused by any magnetic susceptibility difference ($\Delta\chi$) between the samples and the tissue phantom, single layer substrate samples were used in simulations correspoinding to the experiments in which a combination of materials were used in fabricating the samples. This approach narrowed down the affect of the material $\Delta\chi$ in generating the image artifacts from a single material. Combining the simulated and the experimental results, one can have a better understanding of the role of each material in the formation of any image artifacts in each fabricated sample.

One of the observations during this work was the difference in magnetic field perturbation in p-type and n-type silicon. The experiments in the current work indicated that the magnetic susceptibility of silicon, and consequently the extent to which it caused magnetic field perturbation and image artifacts under MRI, is highly dependent on their doping type. As observed in the experimental results shown in Figure 4.12 p-type Si induced less image artifacts while n-type Si displayed severe image artifacts under MRI. The magnetic susceptibility of Si, and its dependence to the doping type and concentration, was reported in other works [80], [81], [166]. However, this

dependence on the doping concentration and type was not observed in epitaxially grown thin 3C-SiC films used in these experiments. One reason for this can be due to the very thin nature of the film which causes less image artifacts as reported elsewhere [59]. The reason why it was possible for the 3C-SiC samples to be fabricated very thin (~10 μm) was because of the monolithic fabrication method that is only possible in 3C-SiC because of its high mechanical strength, flexibility and chemical stability.

The induced heat in the current work was estimated using Multiphysics finite FEM simulations, yet some experimental measurements were done to validate the simulation results. Induced sample heating, specifically in the 3C-SiC samples, was expected to be lower than the sensitivity range of the fiberoptic thermometer probes. Therefore the measurements focused solely on temperature rise differences between the samples since absolute measurement was not possible. At the same time, validation of the simulations needed to be done to ensure the accuracy of the simulated data. For this reason, the focus of the temperature measurement during the MRI experiments was in fact restricted to measuring the increased temperature inside the phantom at certain locations and comparing them with simulations. In addition, a temperature measurement trial was performed on the Pt sample with the extended SS wires to measure the increased temperature in the case of the longest of three electrodes (i.e., worst-case scenario). As seen in Figure 4.14, the simulated results indicated a meaningful difference in the SAR distribution between the Pt and 3C-SiC samples. The simulations predicted a ~30% lower maximum SAR for 3C-SiC comparing to Pt. Although both samples experienced very low amounts of SAR, in the case of a longer electrode this difference was more evident and thus this was used to validate the simulation.

Another important point observed during the MRI experiments was the image artifacts measured for the fabricated all-3C-SiC neural probe. The probe showed very little footprint inside the 7 T MRI scans. However, the tip of the probe had visible dark image artifacts which might be caused by the sharp point of the tip. The effect of the shape and sharp points in creating image artifacts has been studied elsewhere [59] where it is believed that sharp points can increase image artifacts under MRI. However, one of the reasons that the probe showed some visibility during MRI imaging was believed to be due to the very thin (~27μm) Si substrate film that remained on the probe backside. Once the Si was etched away the 3C-SiC neural probe was virtually transparent at 7 T which is a highly significant result.

Chapter 5: Conclusion and Future Work

5.1 Conclusion

In this dissertation, the fabrication and electrical characterization of an all-SiC neural probe was presented. The SiC neural probe was fabricated from p- and n^+-type 3C-SiC epilayers grown on SOI wafers. First, a moderately doped p-type 3C-SiC film was grown on an SOI wafer, followed by a layer of heavily doped, and thus semi-metallic, n^+-type 3C-SiC. The surface morphology of the top n^+ epilayer was measured. The measurement showed a relatively rough surface with a mean surface roughness ranging from ~21 nm to ~244 nm depending on the substrate that the 3C-SiC epi-films were grown on. Neural probes with sixteen traces, electrode sites, and other test structures were patterned on the 3C-SiC epilayers via MEMS microfabrication processes. Metallic traces were absent from the shank of the probe, and instead the semi-metallic n^+ layer was used to form conductive traces and electrode sites. A thin layer of *a*-SiC was deposited on top of the conductive traces to serve as an insulator. The probes were harvested using dissolution of the buried oxide layer of the SOI handle wafer to provide ease of manufacture. The backside silicon layer remaining after release of the probes was removed via KOH etching. Adjacent traces were electrically isolated through a built-in n-p-n junction. After completion of device fabrication, the performance of the n-p-n junctions were evaluated through current-voltage measurements and the corresponding diode turn-on voltage was determined to be ~1.4 V. Electrical measurements showed satisfactory p-n junction performance, but the observed leakage current needs to be improved via higher quality 3C-SiC epitaxial films. In addition, initial electrochemical characterization work with 491 μm^2 surface area test planar single-ended microelectrodes

demonstrated good impedance, charge storage capacity, and charge per phase values. These results support the feasibility of neural stimulation and recording with the fabricated all-SiC neural probe. However, further studies are necessary to demonstrate the acute recording and stimulation capability and chronic stability of the fabricated SiC neural probes, and, consequently, in-vitro accelerated aging and in-vivo studies in a rodent model are planned and will be reported in the future.

The magnetic resonance imaging (MRI) compatibility of 3C-SiC was evaluated via numerical simulation and experiments under a 7 T MRI for small laboratory animals using a human brain tissue phantom. First, it was believed that a brain implant fabricated monolithically from 3C-SiC can remarkably improve the MRI compatibility of these implants. Most importantly, the 3C-SiC implants may increase the standard B_0 intensity that is allowed to be used with commercial MRI compatible implants which would allow for use up to 7 T. To perform this evaluation study, silicon of various doping type and concentration, and platinum were used as reference materials to compare the MRI compatibility of 3C-SiC with. Various samples were fabricated from 3C-SiC, Si, Pt and PI (polyimide). Mainly, Si and PI were used as the substrate to deposit Pt, and also Si and SOI to grow thin epitaxial films of 3C-SiC on. A plastic tube filled with saline gel phantom, a mixture of PAA, pure NaCl, and distilled water, was used as the tissue phantom for MRI tests. The samples were tested under MRI to measure any image artifacts generated by each sample and any induced heating. Electromagnetic and thermal simulations, based on the finite element method (FEM) in ANSYS Multiphysics, and Fourier-based susceptibility induced B_0 field shifts formulated in MATLAB, were used to estimate the SAR distribution, induced heating and any magnetic perturbation (image artifacts) surrounding the samples. Finally, the fabricated 3C-SiC neural probe was tested under MRI excitation (short scans) to measure image artifacts surrounding

the probe. It was concluded that a monolithic 3C-SiC implant can remarkably decrease image artifacts caused by the magnetic susceptibility difference between the tissue and the implant. It also can reduce the SAR and induced heating caused by the conductive parts in the implant via reduced RF coupling. This was proved through FEM simulations as well as multiple MRI experiments. The MRI compatibility of the 3C-SiC neural implant should not be demonstrated using laboratory animals which is planned for the near future.

5.2 Future Work

The future work mainly focuses on improving the fabricated neural probe and implanting it in laboratory animals to record and stimulate the nervous system to access the recording/stimulating functionality of the fabricated devices. In addition, modeling and simulation may be used to improve our understanding of the electrochemical tests and also thin film growth methods

5.2.1 Epitaxial Growth Improvement and Current Leakage Reduction

To fabricate the 3C-SiC neural probe reported here, a combination of ethylene (C_2H_4) and trichlorosilane ($SiHCl_3$) were used as precursor gasses in the epitaxial process. As mentioned before, this produced a varying surface morphology with mean surface roughness of approximately ~21 nm (specular, edge region) to ~244 nm (rough, center region). It is possible that this surface roughness contributed to complications in the fabrication process, such as with photolithographic patterning, and may have had an effect on the mechanical properties of the grown films to the detriment of probe function. It is suspected that this contributed to the higher than desired leakage current (less than 8 μA_{rms}). By optimizing various parameters in the epitaxial process, such as gas

composition and flow rates, temperature, and pressure, the process can be improved to reduce this surface roughness. Additionally, post-processing steps, such as mechanical or chemo-mechanical polishing (CMP), can be added to further improve the surface morphology; particularly to reduce surface roughness. The higher leakage current in the 3C-SiC films, compared to the results reported by Bernardin et al [ref] in 4H-SiC, may negatively affect the final device's functionality. Surface roughness is known to be associated crystal defects; thus, a higher defect density may cause higher leakage current. It is believed that the high surface roughness in this work, an indication of poor crystallinity, in conjunction with a high number of defects, may be the cause of the observed higher than expected leakage current. As mentioned, a lower surface roughness via an optimized epitaxial growth process would be expected to improve both the mechanical properties and the leakage current.

In order to improve the all-SiC performance on 3C-SiC, new epitaxial wafers were kindly provided by Dr. Francesco La Via of the IMM-CNR, Catania Section, Catania Sicily (IT). These are presenting under fabrication by Chenyin Feng in our group and preliminary IV electrical testing of pn diodes is showing improved performance. We therefore hope that the next generation of 3C-SiC neural probes will display lower leakage current than those reported here. More importantly a new probe design will be used so that the probes may be more easily packaged for in-vitro and in-vivo testing.

5.2.2 MRI In-vivo Experiments

In order to evaluate the MRI compatibility of the fabricated 3C-SiC neural probes, these probes can be implanted inside a rat or mouse brain in any of the intracortical regions. In fact, these neural probes will be ultimately implanted inside rodent brain. The same animal that is

implanted can be tested for MRI compatibility under MRI scans. It is believed that brain inhomogeneity, as well as the animal body inside the MRI, may affect image artifact distributions. In addition, depending on which part of the brain the probe is implanted in may generate a different image artifact distribution and lead to more complications. The most important outcome of this portion of future work would be post-MRI tissue histology to assess the degree of tissue damage resulting from MRI scans with respect to a control implant. Only after these experiments are conducted will the hypothesis that all-SiC probes constructed of 3C-SiC are compatible with 7 T MRI fields will be proven. Fortunately, full-packaged and functional neural probes are not required for this step and it is hoped that these in-vivo experiments will be conducted as soon as practicable.

5.2.3 MRI Compatible DBS from 3C-SiC Material

One of the main applications for an MRI compatible neural implant is deep brain stimulation (DBS). The DBS electrodes are larger than intracortical electrodes, and consequently are more prone to MRI induced heating and tissue damage. As MRI is broadly used in pre- and post-surgery evaluations for DBS placement, developing an MRI compatible DBS is very important. 3C-SiC is an excellent candidate for developing an MRI compatible DBS as well, as a monolithic 3C-SiC implant not only showed a high compatibility to MRI in this work, but also its mechanical and chemical stability, and biocompatibility can increase the lifetime of DBS implants [167]. The MRI compatibility of the proposed DBS can be evaluated using the simulations introduced in this work and MRI experiments as studied in the current work.

5.2.4 Electrochemical Modeling of 3C-SiC Neural Interface

Modelling and simulations help us better understand physical phenomena happening during a specific process. Throughout this work we used FEM simulations to model induced heating in proximity to implants under MRI and also to estimate any image artifacts under MRI. Electrochemical simulations which model the physics happening at the interface between neurons and electrodes can be used to predict the charge storage capacity in a capacitive interface as well as the electrochemical impedance of an interface between an electrode and neurons. In particular, this modeling can be done using fluid dynamics equations and can be simulated in a FEM simulation platform such as ANSYS Fluent.

References

[1] M. O. Krucoff, S. Rahimpour, M. W. Slutzky, V. R. Edgerton, and D. A. Turner, “Enhancing nervous system recovery through neurobiologics, neural interface training, and neurorehabilitation,” *Front. Neurosci.*, vol. 10, no. DEC, 2016.

[2] M. A. Lebedev and M. A. L. Nicolelis, “Brain-machine interfaces: past, present and future,” *Trends Neurosci.*, vol. 29, no. 9, pp. 536–546, 2006.

[3] T. C. Zhang and W. M. Grill, “Modeling deep brain stimulation: Point source approximation versus realistic representation of the electrode,” *J. Neural Eng.*, vol. 7, no. 6, 2010.

[4] Akram, Harith, Stamatios N. Sotiropoulos, Saad Jbabdi, Dejan Georgiev, Philipp Mahlknecht, Jonathan Hyam, Thomas Foltynie et al. "Subthalamic deep brain stimulation sweet spots and hyperdirect cortical connectivity in Parkinson's disease." Neuroimage 158 (2017): 332-345.

[5] A. Prochazka, “Neurophysiology and neural engineering: A review,” *J. Neurophysiol.*, vol. 118, no. 2, pp. 1292–1309, 2017.

[6] Öztürk, Sevgi, Ismail Devecioğlu, Mohammad Beygi, Ahmet Atasoy, Şenol Mutlu, Mehmed Özkan, and Burak Güçlü. "Real-time performance of a tactile neuroprosthesis on awake behaving rats." IEEE Transactions on Neural Systems and Rehabilitation Engineering 27, no. 5 (2019): 1053-1062.

[7] M. Y. Rotenberg and B. Tian, “Bioelectronic devices: Long-lived recordings,” *Nat. Biomed. Eng.*, vol. 1, no. 3, p. 48, 2017.

[8] A. Verkhratsky, O. A. Krishtal, and O. H. Petersen, “From Galvani to patch clamp: The development of electrophysiology,” *Pflugers Arch. Eur. J. Physiol.*, vol. 453, no. 3, pp. 233–247, 2006.

[9] J. M. Delgado, “Permanent implantation of multilead electrodes in the brain.,” *Yale J. Biol. Med.*, vol. 24, no. 5, pp. 351–358, 1952.

[10] T. N. 4. Hubel, D.H.; Wiesel, “No Title,” *J. Physiol.*, no. 160, pp. 106–154, 1962.

[11] R. A. Normann, P. K. Campbell, and W. P. Li, “Silicon based microstructures suitable for intracortical electrical stimulation (visual prosthesis application),” pp. 714–715 vol.2, 2003.

[12] C. PK, J. KE, H. RJ, H. KW, and N. RA, “A silicon-Based, Three-Dimensional Neural Interface: Manufacturing Processes for an Intracortical Electrode Array,” *IEEE Transactions on Biomedical Engineering*, vol. 38. pp. 758–768, 1991.

[13] Wise KD, Angell JB, and Starr A, “Integrated Circuit Approach To Extracellular Microelectrodes,” no. 3, pp. 238–247, 1969.

[14] R. J. Vetter, J. C. Williams, J. F. Hetke, E. A. Nunamaker, and D. R. Kipke, “Chronic neural recording using silicon-substrate microelectrode arrays implanted in cerebral cortex,” *IEEE Trans. Biomed. Eng.*, vol. 51, no. 6, pp. 896–904, 2004.

[15] C. Xie, J. Liu, T. M. Fu, X. Dai, W. Zhou, and C. M. Lieber, “Three-dimensional macroporous nanoelectronic networks as minimally invasive brain probes,” *Nat. Mater.*, vol. 14, no. 12, pp. 1286–1292, 2015.

[16] A. Thukral, F. Ershad, N. Enan, Z. Rao, and C. Yu, “Soft Ultrathin Silicon Electronics for Soft Neural Interfaces: A Review of Recent Advances of Soft Neural Interfaces Based on Ultrathin Silicon,” *IEEE Nanotechnol. Mag.*, vol. 12, no. 1, pp. 21–34, 2018.

[17] K. Scholten and E. Meng, “Materials for microfabricated implantable devices: A review,” *Lab Chip*, vol. 15, no. 22, pp. 4256–4272, 2015.

[18] G. Hong and C. M. Lieber, “Novel electrode technologies for neural recordings,” *Nat. Rev. Neurosci.*, vol. 20, no. 6, pp. 330–345, 2019.

[19] R. S. Oakes, M. D. Polei, J. L. Skousen, and P. A. Tresco, “An astrocyte derived extracellular matrix coating reduces astrogliosis surrounding chronically implanted microelectrode arrays in rat cortex,” *Biomaterials*, vol. 154, pp. 1–11, 2018.

[20] Eles, James R., Alberto L. Vazquez, Noah R. Snyder, Carl Lagenaur, Matthew C. Murphy, Takashi DY Kozai, and X. Tracy Cui. "Neuroadhesive L1 coating attenuates acute microglial attachment to neural electrodes as revealed by live two-photon microscopy." Biomaterials 113 (2017): 279-292.

[21] Wellman, Steven M., James R. Eles, Kip A. Ludwig, John P. Seymour, Nicholas J. Michelson, William E. McFadden, Alberto L. Vazquez, and Takashi DY Kozai. "A materials roadmap to functional neural interface design." Advanced functional materials 28, no. 12 (2018): 1701269.

[22] B. Gunasekera, T. Saxena, R. Bellamkonda, and L. Karumbaiah, “Intracortical recording interfaces: Current challenges to chronic recording function,” *ACS Chem. Neurosci.*, vol. 6, no. 1, pp. 68–83, 2015.

[23] M. Jorfi, J. L. Skousen, C. Weder, and J. R. Capadona, “Progress towards biocompatible intracortical microelectrodes for neural interfacing applications,” *J. Neural Eng.*, vol. 12, no. 1, 2015.

[24] Barrese, James C., Naveen Rao, Kaivon Paroo, Corey Triebwasser, Carlos Vargas-Irwin, Lachlan Franquemont, and John P. Donoghue. "Failure mode analysis of silicon-based intracortical microelectrode arrays in non-human primates." Journal of neural engineering 10, no. 6 (2013): 066014.

[25] M. HajjHassan, V. Chodavarapu, and S. Musallam, "NeuroMEMS: Neural probe microtechnologies," *Sensors*, vol. 8, no. 10, pp. 6704–6726, 2008.

[26] E. Meng and R. Sheybani, "Insight: Implantable medical devices," *Lab Chip*, vol. 14, no. 17, pp. 3233–3240, 2014.

[27] G. Jiang, "Design challenges of implantable pressure monitoring system," *Front. Neurosci.*, vol. 4, no. FEB, pp. 2–5, 2010.

[28] M. S. Chae, Z. Yang, and W. Liu, *Implantable Neural Prostheses 2: Techniques and Engineering Approaches*. 2010.

[29] S. E. Saddow, *Silicon carbide biotechnology: a biocompatible semiconductor for advanced biomedical devices and applications*. Elsevier, 2012.

[30] P. M. Sarro, "Silicon carbide as a new MEMS technology," *Sensors Actuators, A Phys.*, vol. 82, no. 1, pp. 210–218, 2000.

[31] M. Wijesundara and R. Azevedo, *Silicon carbide microsystems for harsh environments*, vol. 22. Springer Science & Business Media, 2011.

[32] Dai, Wen, Le Lv, Jibao Lu, Hao Hou, Qingwei Yan, Fakhr E. Alam, Yifan Li et al. "A paper-like inorganic thermal interface material composed of hierarchically structured graphene/silicon carbide nanorods." ACS nano 13, no. 2 (2019): 1547-1554.

[33] C. Coletti, M. J. Jaroszeski, A. Pallaoro, A. M. Hoff, S. Iannotta, and S. E. Saddow, "Biocompatibility and wettability of crystalline SiC and Si surfaces," *Annu. Int. Conf. IEEE Eng. Med. Biol. - Proc.*, no. Di, pp. 5849–5852, 2007.

[34] Saddow, S. E., C. L. Frewin, M. Nezafati, A. Oliveros, S. Afroz, J. Register, M. Reyes, and S. Thomas. "3C-SiC on Si: A bio-and hemo-compatible material for advanced nano-bio devices." In 2014 IEEE 9th Nanotechnology Materials and Devices Conference (NMDC), pp. 49-53. IEEE, 2014.

[35] Kotzar, Geoffrey, Mark Freas, Phillip Abel, Aaron Fleischman, Shuvo Roy, Christian Zorman, James M. Moran, and Jeff Melzak. "Evaluation of MEMS materials of construction for implantable medical devices." Biomaterials 23, no. 13 (2002): 2737-2750.

[36] E. K. Bernardin, C. L. Frewin, R. Everly, J. Ul Hassan, and S. E. Saddow, “Demonstration of a robust all-silicon-carbide intracortical neural interface,” *Micromachines*, vol. 9, no. 8, pp. 1–18, 2018.

[37] Phan, Hoang-Phuong, Yishan Zhong, Tuan-Khoa Nguyen, Yoonseok Park, Toan Dinh, Enming Song, Raja Kumar Vadivelu et al. "Long-Lived, Transferred Crystalline Silicon Carbide Nanomembranes for Implantable Flexible Electronics." ACS nano 13, no. 10 (2019): 11572-11581.

[38] S. M. Won, E. Song, J. Zhao, J. Li, J. Rivnay, and J. A. Rogers, “Recent Advances in Materials, Devices, and Systems for Neural Interfaces,” *Adv. Mater.*, vol. 30, no. 30, pp. 1–19, 2018.

[39] C. L. Frewin, C. Locke, L. Mariusso, E. J. Weeber, and S. E. Saddow, “Silicon carbide neural implants: In vivo neural tissue reaction,” *Int. IEEE/EMBS Conf. Neural Eng. NER*, pp. 661–664, 2013.

[40] Knaack, Gretchen L., Daniel G. McHail, German Borda, Beomseo Koo, Nathalia Peixoto, Stuart F. Cogan, Theodore C. Dumas, and Joseph J. Pancrazio. "In vivo characterization of amorphous silicon carbide as a biomaterial for chronic neural interfaces." Frontiers in neuroscience 10 (2016): 301.

[41] Knaack, Gretchen L., Hamid Charkhkar, Stuart F. Cogan, and Joseph J. Pancrazio. "Amorphous silicon carbide for neural interface applications." In Silicon Carbide Biotechnology, pp. 249-260. Elsevier, 2016.

[42] Vomero, Maria, Elisa Castagnola, Juan S. Ordonez, Stefano Carli, Elena Zucchini, Emma Maggiolini, Calogero Gueli et al. "Incorporation of Silicon Carbide and Diamond- Like Carbon as Adhesion Promoters Improves In Vitro and In Vivo Stability of Thin- Film Glassy Carbon Electrocorticography Arrays." Advanced Biosystems 2, no. 1 (2018): 1700081.

[43] Lei, Xin, Sheryl Kane, Stuart Cogan, Henri Lorach, Ludwig Galambos, Philip Huie, Keith Mathieson, Theodore Kamins, James Harris, and Daniel Palanker. "SiC protective coating for photovoltaic retinal prosthesis." Journal of neural engineering 13, no. 4 (2016): 046016.

[44] Deku, Felix, Christopher L. Frewin, Allison Stiller, Yarden Cohen, Saher Aqeel, Alexandra Joshi-Imre, Bryan Black, Timothy J. Gardner, Joseph J. Pancrazio, and Stuart F. Cogan. "Amorphous silicon carbide platform for next generation penetrating neural interface designs." Micromachines 9, no. 10 (2018): 480.

[45] Diaz-Botia, C. A., L. E. Luna, Maysamreza Chamanzar, C. Carraro, P. N. Sabes, R. Maboudian, and Michel M. Maharbiz. "Fabrication of all-silicon carbide neural interfaces." In 2017 8th International IEEE/EMBS Conference on Neural Engineering (NER), pp. 170-173. IEEE, 2017.

[46] F. Deku, Y. Cohen, A. Joshi-Imre, A. Kanneganti, T. J. Gardner, and S. F. Cogan, “Amorphous silicon carbide ultramicroelectrode arrays for neural stimulation and recording,” *J. Neural Eng.*, vol. 15, no. 1, 2018.

[47] F. Deku, A. Ghazavi, and S. F. Cogan, “Neural interfaces based on amorphous silicon carbide ultramicroelectrode arrays,” *Bioelectron. Med.*, vol. 1, no. 3, pp. 185–200, 2018.

[48] Diaz-Botia, C. A., L. E. Luna, R. M. Neely, M. Chamanzar, C. Carraro, J. M. Carmena, P. N. Sabes, R. Maboudian, and M. M. Maharbiz. "A silicon carbide array for electrocorticography and peripheral nerve recording." Journal of neural engineering 14, no. 5 (2017): 056006.

[49] L. Golestanirad, L. M. Angelone, M. I. Iacono, H. Katnani, L. L. Wald, and G. Bonmassar, “Local SAR near deep brain stimulation (DBS) electrodes at 64 and 127 MHz: A simulation study of the effect of extracranial loops,” *Magn. Reson. Med.*, vol. 78, no. 4, pp. 1558–1565, 2017.

[50] J. A. Nyenhuis, S. M. Park, R. Kamondetdacha, A. Amjad, F. G. Shellock, and A. R. Rezai, “MRI and implanted medical devices: Basic interactions with an emphasis on heating,” *IEEE Trans. Device Mater. Reliab.*, vol. 5, no. 3, pp. 467–479, 2005.

[51] E. Neufeld, S. Kühn, G. Szekely, and N. Kuster, “Measurement, simulation and uncertainty assessment of implant heating during MRI,” *Phys. Med. Biol.*, vol. 54, no. 13, pp. 4151–4169, 2009.

[52] J. P. Hornak, “The basics of MRI, 2008,” *URL http//www.cis.rit.edu/htbooks/mri/index.html*, vol. 68, 2008.

[53] Nimbalkar, Surabhi, Erwin Fuhrer, Pedro Silva, Tri Nguyen, Martin Sereno, Sam Kassegne, and Jan Korvink. "Glassy carbon microelectrodes minimize induced voltages, mechanical vibrations, and artifacts in magnetic resonance imaging." Microsystems & nanoengineering 5, no. 1 (2019): 1-11.

[54] R. C. Hartwell and F. G. Shellock, “MRI of cervical fixation devices: Sensation of heating caused by vibration of metallic components,” *J. Magn. Reson. Imaging*, vol. 7, no. 4, pp. 771–772, 1997.

[55] Nordbeck, Peter, Ingo Weiss, Philipp Ehses, Oliver Ritter, Marcus Warmuth, Florian Fidler, Volker Herold et al. "Measuring RF- induced currents inside implants: impact of device configuration on MRI safety of cardiac pacemaker leads." Magnetic Resonance in Medicine: An Official Journal of the International Society for Magnetic Resonance in Medicine 61, no. 3 (2009): 570-578.

[56] ASTM F2182-11a, Standard Test Method for Measurement of Radio Frequency Induced Heating On or Near Passive Implants During Magnetic Resonance Imaging, ASTM International, West Conshohocken, PA, 2011, www.astm.org

[57] Erhardt, Johannes B., Erwin Fuhrer, Oliver G. Gruschke, Jochen Leupold, Matthias C. Wapler, Jürgen Hennig, Thomas Stieglitz, and Jan G. Korvink. "Should patients with brain implants undergo MRI?." Journal of neural engineering 15, no. 4 (2018): 041002.

[58] G. Bonmassar, K. Fujimoto, and A. J. Golby, "PTFOS: Flexible and Absorbable Intracranial Electrodes for Magnetic Resonance Imaging," *PLoS One*, vol. 7, no. 9, 2012.

[59] F. M. Martinez-Santiesteban, S. D. Swanson, D. C. Noll, and D. J. Anderson, "Magnetic field perturbation of neural recording and stimulating microelectrodes," *Phys. Med. Biol.*, vol. 52, no. 8, pp. 2073–2088, 2007.

[60] J. P. Marques and R. Bowtell, "Application of a fourier-based method for rapid calculation of field inhomogeneity due to spatial variation of magnetic susceptibility," *Concepts Magn. Reson. Part B Magn. Reson. Eng.*, vol. 25, no. 1, pp. 65–78, 2005.

[61] S. E. Saddow, C. L. Frewin, M. Reyes, J. Register, M. Nezafati, and S. Thomas, "3C-SiC on Si: A biocompatible material for advanced bioelectronic devices," *ECS Trans.*, vol. 61, no. 7, pp. 101–111, 2014.

[62] S. Oh, Y. C. Ryu, G. Carluccio, C. T. Sica, and C. M. Collins, "Measurement of SAR-induced temperature increase in a phantom and in vivo with comparison to numerical simulation," *Magn. Reson. Med.*, vol. 71, no. 5, pp. 1923–1931, 2014.

[63] Golestanirad, Laleh, Maria Ida Iacono, Boris Keil, Leonardo M. Angelone, Giorgio Bonmassar, Michael D. Fox, Todd Herrington et al. "Construction and modeling of a reconfigurable MRI coil for lowering SAR in patients with deep brain stimulation implants." Neuroimage 147 (2017): 577-588.

[64] P. A. Bottomley, A. Kumar, W. A. Edelstein, J. M. Allen, and P. V. Karmarkar, "Designing passive MRI-safe implantable conducting leads with electrodes," *Med. Phys.*, vol. 37, no. 7, pp. 3828–3843, 2010.

[65] F. G. Shellock, "Radiofrequency energy-induced heating during MR procedures: A review," *J. Magn. Reson. Imaging*, vol. 12, no. 1, pp. 30–36, 2000.

[66] D. Li, X. Ji, J. Zheng, C. Pan, J. Chen, and W. Kainz, "A Novel Design of Implantable Esophageal Stent to Reduce the MRI RF-Induced Heating," *IEEE Trans. Electromagn. Compat.*, vol. 59, no. 3, pp. 805–812, 2017.

[67] J. M. Allen, P. A. Bottomley, W. A. Edelstein, and P. V. Karmarkar, "MRI and RF compatible leads and related methods of operating and fabricating leads," vol. 1, no. 60, 2008.

[68] L. Golestanirad, B. Keil, L. M. Angelone, G. Bonmassar, A. Mareyam, and L. L. Wald, "Feasibility of using linearly polarized rotating birdcage transmitters and close-fitting receive arrays in MRI to reduce SAR in the vicinity of deep brain simulation implants," *Magn. Reson. Med.*, vol. 77, no. 4, pp. 1701–1712, 2017.

[69] L. M. Angelone, J. Ahveninen, J. W. Belliveau, and G. Bonmassar, "Analysis of the role of lead resistivity in specific absorption rate for deep brain stimulator leads at 3T MRI," *IEEE Trans. Med. Imaging*, vol. 29, no. 4, pp. 1029–1038, 2010.

[70] S. M. Park, R. Kamondetdacha, A. Amjad, and J. A. Nyenhuis, "MRI safety: RF-induced heating near straight wires," *INTERMAG ASIA 2005 Dig. IEEE Int. Magn. Conf.*, vol. 41, no. 10, p. 622, 2005.

[71] C. D. Smith, A. V. Kildishev, J. A. Nyenhuis, K. S. Foster, and J. D. Bourland, "Interactions of magnetic resonance imaging radio frequency magnetic fields with elongated medical implants," *J. Appl. Phys.*, vol. 87, no. 9, pp. 6188–6190, 2000.

[72] W. R. Nitz, A. Oppelt, W. Renz, C. Manke, M. Lenhart, and J. Link, "On the heating of linear conductive structures as guide wires and catheters in interventional MRI," *J. Magn. Reson. Imaging*, vol. 13, no. 1, pp. 105–114, 2001.

[73] C. Y. Liu, K. Farahani, D. S. K. Lu, G. Duckwiler, and A. Oppelt, "Safety of MRI-guided endovascular guidewire applications," *J. Magn. Reson. Imaging*, vol. 12, no. 1, pp. 75–78, 2000.

[74] M. E. Ladd, H. H. Quick, P. Boesiger, and G. C. Mckinnon, "RF heating of actively visualized catheters and guidewires," *Proc. Intl. Soc. Mag. Reson. Med. 6*, p. 473, 1998.

[75] C. J. Yeung, R. C. Susil, and E. Atalar, "RF safety of wires in interventional MRI: Using a safety index," *Magn. Reson. Med.*, vol. 47, no. 1, pp. 187–193, 2002.

[76] J. M. Henderson, J. Thach, M. Phillips, K. Baker, F. G. Shellock, and A. R. Rezai, "Permanent neurological deficit related to magnetic resonance imaging in a patient with implanted deep brain stimulation electrodes for Parkinson's disease: Case report," *Neurosurgery*, vol. 57, no. 5, p. 1063, 2005.

[77] T. Kimoto and J. A. Cooper, *Fundamentals of silicon carbide technology: growth, characterization, devices and applications*. John Wiley & Sons, 2014.

[78] Brady, M. F., W. H. Brixius, G. Fechko, R. C. Glass, D. Henshall, Jason R. Jenny, R. T. Leonard et al. "Status of large diameter SiC crystal growth for electronic and optical applications." In Materials Science Forum, vol. 338, pp. 3-8. Trans Tech Publications Ltd, 2000.

[79] J. H. Duyn and J. Schenck, “Contributions to magnetic susceptibility of brain tissue,” *NMR Biomed.*, vol. 30, no. 4, pp. 1–37, 2017.

[80] M. P. Sarachik, D. R. He, W. Li, M. Levy, and J. S. Brooks, “Magnetic properties of boron-doped silicon,” *Phys. Rev. B*, vol. 31, no. 3, pp. 1469–1477, 1985.

[81] H. G. Schlager and H. V. Löhneysen, “Susceptibility of local magnetic moments in phosphorus-doped silicon near the metal-insulator transition,” *Europhys. Lett.*, vol. 40, no. 6, pp. 661–666, 1997.

[82] C. L. Frewin, S. Thomas, C. Coletti, and S. E. Saddow, *In Vivo Exploration of Robust Implantable Devices Constructed From Biocompatible 3C-Sic*, Second Edi. Elsevier Inc., 2016.

[83] S. F. Cogan, “Neural Stimulation and Recording Electrodes,” *Annu. Rev. Biomed. Eng.*, vol. 10, no. 1, pp. 275–309, 2008.

[84] K. W. Böer and U. W. Pohl, *Semiconductor physics*. Springer, 2018.

[85] S. Tiwari, *Compound semiconductor device physics*. Academic press, 2013.

[86] Sze, *Physics of Semiconductor Devices Physics of Semiconductor Devices*, vol. 10. 1995.

[87] S. J. Moss and A. Ledwith, *Chemistry of the Semiconductor Industry*. Springer Science & Business Media, 1989.

[88] E. F. Schubert, *Doping in III-V semiconductors*. E. Fred Schubert, 2015.

[89] A. K. Jonscher, *Semiconductor physics*, vol. 283, no. 5749. 1980.

[90] J. R. Hook and H. E. Hall, “Solid state physics 2nd Edition.” John Wiley & Sons Ltd, 2001.

[91] I. Tighineanu, S. Langa, H. Föll, and V. Ursachi, *Porous III-V Semiconductors*. Ştiinţa, 2005.

[92] S. E. Saddow and A. Agarwal, *Advances in silicon carbide processing and applications*. Artech House, 2004.

[93] G. Ziegler, P. Lanig, D. Theis, and C. Weyrich, “Single crystal growth of SiC substrate material for blue light emitting diodes,” *IEEE Trans. Electron Devices*, vol. 30, no. 4, pp. 277–281, 1983.

[94] J. W. Palmour, J. A. Edmond, H. S. Kong, and C. H. Carter Jr, “Silicon carbide and related materials,” in *Inst. of Phys. Conf Proc. 137 (IOP Publishing, 1994)*, 1994, pp. 499–502.

[95] D. J. Larkin, P. G. Neudeck, J. A. Powell, and L. G. Matus, "Site- competition epitaxy for superior silicon carbide electronics," *Appl. Phys. Lett.*, vol. 65, no. 13, pp. 1659–1661, 1994.

[96] U. Forsberg, Ö. Danielsson, A. Henry, M. K. Linnarsson, and E. Janzén, "Aluminum doping of epitaxial silicon carbide," *J. Cryst. Growth*, vol. 253, no. 1–4, pp. 340–350, 2003.

[97] A. N. Dula, J. Virostko, and F. G. Shellock, "Assessment of MRI issues at 7 T for 28 implants and other objects," *Am. J. Roentgenol.*, vol. 202, no. 2, pp. 401–405, 2014.

[98] J. Husband and A. Padhani, "Recommendations for cross-sectional imaging in cancer management," *R. Coll. Radiol. London*, 2006.

[99] D. Dormont, D. Seidenwurm, D. Galanaud, P. Cornu, J. Yelnik, and E. Bardinet, "Neuroimaging and deep brain stimulation," *Am. J. Neuroradiol.*, vol. 31, no. 1, pp. 15–23, 2010.

[100] D. I. Hoult and B. Bhakar, "NMR signal reception: Virtual photons and coherent spontaneous emission," *Concepts Magn. Reson. An Educ. J.*, vol. 9, no. 5, pp. 277–297, 1997.

[101] R. K. Harris, "Nuclear Magnetic Resonance Spectroscopy, Pitman Pub," *INC, London*, 1983.

[102] A. D. Carrington, "McLachlan Introduction To Magnetic Resonance Chapman and Hall," *London. 350s*, 1967.

[103] R. O. Louro, "Introduction to biomolecular NMR and metals," in *Practical Approaches to Biological Inorganic Chemistry*, Elsevier, 2013, pp. 77–107.

[104] T. D. W. Claridge, *High-resolution NMR techniques in organic chemistry*, vol. 27. Elsevier, 2016.

[105] T. C. Farrar, "Introduction to Pulse NMR Spectroscopy." Farragut Press Chicago, 1987.

[106] G. D. Jackson, R. I. Kuzniecky, and G. S. Pell, "Principles of magnetic resonance imaging," *Magn. Reson. Epilepsy Neuroimaging Tech. 2nd ed. London Elsevier*, pp. 17–28, 2005.

[107] "MRI: A Guided Tour." [Online]. Available: https://nationalmaglab.org/.

[108] S. S. Hidalgo- Tobon, "Theory of gradient coil design methods for magnetic resonance imaging," *Concepts Magn. Reson. Part A*, vol. 36, no. 4, pp. 223–242, 2010.

[109] J. T. Vaughan and J. R. Griffiths, *RF coils for MRI*. John Wiley & Sons, 2012.

[110] Boissoles, Patrice, and Gabriel Caloz. "Magnetic field properties in a birdcage coil." (2006).

[111] L. Axel, “Surface coil magnetic resonance imaging,” *J. Comput. Assist. Tomogr.*, vol. 8, no. 3, pp. 381–384, 1984.

[112] C. E. Hayes, W. A. Edelstein, J. F. Schenck, O. M. Mueller, and M. Eash, “An efficient, highly homogeneous radiofrequency coil for whole-body NMR imaging at 1.5 T,” *J. Magn. Reson.*, vol. 63, no. 3, pp. 622–628, 1985.

[113] Rios, Nibardo Lopez, Philippe Pouliot, Konstantinos Papoutsis, Alexandru Foias, Nikola Stikov, Frederic Lesage, Mathieu Dehaes, and Julien Cohen-Adad. "Design and construction of an optimized transmit/receive hybrid birdcage resonator to improve full body images of medium-sized animals in 7T scanner." PloS one 13, no. 2 (2018).

[114] T. Fukasawa, N. Yoneda, and H. Miyashita, “Investigation on Current Reduction Effects of Baluns for Measurement of a Small Antenna,” *IEEE Trans. Antennas Propag.*, vol. 67, no. 7, pp. 4323–4329, 2019.

[115] M. Wilcox, S. M. Wright, and M. P. McDougall, “Multi-Tuned Cable Traps for Multinuclear MRI and MRS,” *IEEE Trans. Biomed. Eng.*, vol. 9294, no. c, pp. 1–1, 2019.

[116] Cabot, Eugenia, Tom Lloyd, Andreas Christ, Wolfgang Kainz, Mark Douglas, Gregg Stenzel, Steve Wedan, and Niels Kuster. "Evaluation of the RF heating of a generic deep brain stimulator exposed in 1.5 T magnetic resonance scanners." Bioelectromagnetics 34, no. 2 (2013): 104-113.

[117] ASTM F2052-06e1, Standard Test Method for Measurement of Magnetically Induced Displacement Force on Medical Devices in the Magnetic Resonance Environment, ASTM International, West Conshohocken, PA, 2006, www.astm.org

[118] ASTM F2119-07(2013), Standard Test Method for Evaluation of MR Image Artifacts from Passive Implants, ASTM International, West Conshohocken, PA, 2013, www.astm.org

[119] C. A. Balanis, *Antenna theory: analysis and design*. John wiley & sons, 2016.

[120] D. Demarchi and A. Tagliaferro, *Carbon for sensing devices*. Springer, 2015.

[121] Zielinski, Marcin, Roxana Arvinte, Thierry Chassagne, Adrien Michon, Marc Portail, Pawel Kwasnicki, Leszek Konczewicz, Sylvie Contreras, Sandrine Juillaguet, and Hervé Peyre. "p-type doping of 4H-and 3C-SiC epitaxial layers with aluminum." In Materials Science Forum, vol. 858, pp. 137-142. Trans Tech Publications Ltd, 2016.

[122] La Via, F., A. Severino, R. Anzalone, C. Bongiorno, G. Litrico, M. Mauceri, M. Schoeler, P. Schuh, and P. Wellmann. "From thin film to bulk 3C-SiC growth: Understanding the mechanism of defects reduction." Materials Science in Semiconductor Processing 78 (2018): 57-68.

[123] M. Zimbone, M. Mauceri, G. Litrico, E. G. Barbagiovanni, C. Bongiorno, and F. La Via, “Protrusions reduction in 3C-SiC thin film on Si,” *J. Cryst. Growth*, vol. 498, no. May, pp. 248–257, 2018.

[124] S. Roy, C. Jacob, and S. Basu, “Ohmic contacts to 3C-SiC for Schottky diode gas sensors,” *Solid. State. Electron.*, vol. 47, no. 11, pp. 2035–2041, 2003.

[125] R. E. Avila, J. J. Kopanski, and C. D. Fung, “Behavior of ion-implanted junction diodes in 3C SiC,” *J. Appl. Phys.*, vol. 62, no. 8, pp. 3469–3471, 1987.

[126] D. B. McCreery, W. F. Agnew, T. G. H. Yuen, and L. Bullara, “Charge density and charge per phase as cofactors in neural injury induced by electrical stimulation,” *IEEE Trans. Biomed. Eng.*, vol. 37, no. 10, pp. 996–1001, 1990.

[127] T. L. Rose and L. S. Robblee, “Electrical stimulation with Pt electrodes. VIII. Electrochemically safe charge injection limits with 0.2 ms pulses (neuronal application),” *IEEE Trans. Biomed. Eng.*, vol. 37, no. 11, pp. 1118–1120, 1990.

[128] Bernardin, Evans, Christopher L. Frewin, Abhishek Dey, Richard Everly, Jawad Ul Hassan, Erik Janzén, Joe Pancrazio, and Stephen E. Saddow. "Development of an all-SiC neuronal interface device." MRS Advances 1, no. 55 (2016): 3679-3684.

[129] H. S. Kong, J. T. Glass, and R. F. Davis, “Growth rate, surface morphology, and defect microstructures of β—SiC films chemically vapor deposited on 6H—SiC substrates,” *J. Mater. Res.*, vol. 4, no. 1, pp. 204–214, 1989.

[130] R. Maboudian, C. Carraro, D. G. Senesky, and C. S. Roper, “Advances in silicon carbide science and technology at the micro- and nanoscales,” *J. Vac. Sci. Technol. A Vacuum, Surfaces, Film.*, vol. 31, no. 5, p. 050805, 2013.

[131] Davis, Robert F., Z. Sitar, B. E. Williams, H. S. Kong, H. J. Kim, J. W. Palmour, J. A. Edmond, J. Ryu, J. T. Glass, and C. H. Carter Jr. "Critical evaluation of the status of the areas for future research regarding the wide band gap semiconductors diamond, gallium nitride and silicon carbide." Materials Science and Engineering: B 1, no. 1 (1988): 77-104.

[132] K. M. Jackson, J. Dunning, C. A. Zorman, M. Mehregany, and W. N. Sharpe, “Mechanical properties of epitaxial 3C silicon carbide thin films,” *J. microelectromechanical Syst.*, vol. 14, no. 4, pp. 664–672, 2005.

[133] J. D. Reddy, A. A. Volinsky, C. L. Frewin, C. Locke, and S. E. Saddow, “Mechanical properties of 3C-SiC films for MEMS applications,” *MRS Online Proc. Libr. Arch.*, vol. 1049, 2007.

[134] R. Anzalone, M. Camarda, A. Canino, N. Piluso, F. La Via, and G. D’arrigo, “Defect influence on heteroepitaxial 3C-SiC Young’s modulus,” *Electrochem. Solid-State Lett.*, vol. 14, no. 4, pp. H161–H162, 2011.

[135] C. M. Su, M. Wuttig, A. Fekade, and M. Spencer, “Elastic and anelastic properties of chemical vapor deposited epitaxial 3C- SiC,” *J. Appl. Phys.*, vol. 77, no. 11, pp. 5611–5615, 1995.

[136] R. Green and M. R. Abidian, “Conducting polymers for neural prosthetic and neural interface applications,” *Adv. Mater.*, vol. 27, no. 46, pp. 7620–7637, 2015.

[137] T. Ware, D. Simon, R. L. Rennaker, and W. Voit, “Smart polymers for neural interfaces,” *Polym. Rev.*, vol. 53, no. 1, pp. 108–129, 2013.

[138] R. A. Green, N. H. Lovell, G. G. Wallace, and L. A. Poole-Warren, “Conducting polymers for neural interfaces: challenges in developing an effective long-term implant,” *Biomaterials*, vol. 29, no. 24–25, pp. 3393–3399, 2008.

[139] Stiller, Allison M., Bryan J. Black, Christopher Kung, Aashika Ashok, Stuart F. Cogan, Victor D. Varner, and Joseph J. Pancrazio. "A meta-analysis of intracortical device stiffness and its correlation with histological outcomes." Micromachines 9, no. 9 (2018): 443.

[140] K. Woeppel, Q. Yang, and X. T. Cui, “Recent advances in neural electrode–tissue interfaces,” *Curr. Opin. Biomed. Eng.*, vol. 4, pp. 21–31, 2017.

[141] T. D. Y. Kozai *et al.*, “Ultrasmall implantable composite microelectrodes with bioactive surfaces for chronic neural interfaces,” *Nat. Mater.*, vol. 11, no. 12, pp. 1065–1073, 2012.

[142] Pancrazio, Joseph J., Felix Deku, Atefeh Ghazavi, Allison M. Stiller, Rashed Rihani, Christopher L. Frewin, Victor D. Varner, Timothy J. Gardner, and Stuart F. Cogan. "Thinking small: Progress on microscale neurostimulation technology." Neuromodulation: Technology at the Neural Interface 20, no. 8 (2017): 745-752.

[143] Kozai, Takashi DY, Kasey Catt, Xia Li, Zhannetta V. Gugel, Valur T. Olafsson, Alberto L. Vazquez, and X. Tracy Cui. "Mechanical failure modes of chronically implanted planar silicon-based neural probes for laminar recording." Biomaterials 37 (2015): 25-39.

[144] H. Morkoç, S. Strite, G. B. Gao, M. E. Lin, B. Sverdlov, and M. Burns, “Large-band-gap SiC, III-V nitride, and II-VI ZnSe-based semiconductor device technologies,” *J. Appl. Phys.*, vol. 76, no. 3, pp. 1363–1398, 1994.

[145] R. Saha, N. Jackson, C. Patel, and J. Muthuswamy, “Highly doped polycrystalline silicon microelectrodes reduce noise in neuronal recordings in vivo,” *IEEE Trans. Neural Syst. Rehabil. Eng.*, vol. 18, no. 5, pp. 489–497, 2010.

[146] M. M. R. Howlader, A. U. Alam, R. P. Sharma, and M. J. Deen, “Materials analyses and electrochemical impedance of implantable metal electrodes,” *Phys. Chem. Chem. Phys.*, vol. 17, no. 15, pp. 10135–10145, 2015.

[147] Meijs, Suzan, Maria Alcaide, Charlotte Sørensen, Matthew McDonald, S. Sørensen, K. Rechendorff, A. Gerhardt, Milos Nesladek, Nico JM Rijkhoff, and Cristian Pablo Pennisi. "Biofouling resistance of boron-doped diamond neural stimulation electrodes is superior to titanium nitride electrodes in vivo." Journal of neural engineering 13, no. 5 (2016): 056011.

[148] J. D. Weiland, D. J. Anderson, and M. S. Humayun, "In vitro electrical properties for iridium oxide versus titanium nitride stimulating electrodes," *IEEE Trans. Biomed. Eng.*, vol. 49, no. 12 I, pp. 1574–1579, 2002.

[149] Joshi-Imre, Alexandra, Bryan J. Black, Justin Abbott, Aswini Kanneganti, Rashed Rihani, Bitan Chakraborty, Vindhya R. Danda et al. "Chronic recording and electrochemical performance of amorphous silicon carbide-coated Utah electrode arrays implanted in rat motor cortex." Journal of neural engineering 16, no. 4 (2019): 046006.

[150] Phan, Hoang-Phuong, Yishan Zhong, Tuan-Khoa Nguyen, Yoonseok Park, Toan Dinh, Enming Song, Raja Kumar Vadivelu et al. "Long-Lived, Transferred Crystalline Silicon Carbide Nanomembranes for Implantable Flexible Electronics." ACS nano 13, no. 10 (2019): 11572-11581.

[151] Golestanirad, Laleh, Leonardo M. Angelone, John Kirsch, Sean Downs, Boris Keil, Giorgio Bonmassar, and Lawrence L. Wald. "Reducing RF-induced heating near implanted leads through high-dielectric capacitive bleeding of current (CBLOC)." IEEE transactions on microwave theory and techniques 67, no. 3 (2019): 1265-1273.

[152] Golestanirad, Laleh, Maria Ida Iacono, Boris Keil, Leonardo M. Angelone, Giorgio Bonmassar, Michael D. Fox, Todd Herrington et al. "Construction and modeling of a reconfigurable MRI coil for lowering SAR in patients with deep brain stimulation implants." Neuroimage 147 (2017): 577-588.

[153] L. P. Panych and B. Madore, "The physics of MRI safety," *J. Magn. Reson. Imaging*, vol. 47, no. 1, pp. 28–43, 2018.

[154] S. Louis, "On the AJR Viewbox MRI : A Hairy Situation," *Image (Rochester, N.Y.)*, no. February, pp. 532–535, 2004.

[155] G. Schramm, "Review article Metal artifact correction strategies in MRI- - based attenuation correction in PET / MRI," no. July, 2019.

[156] Scherberger, H., I. Fineman, S. Musallam, D. J. Dubowitz, K. A. Bernheim, Bijan Pesaran, B. D. Corneil, B. Gilliken, and R. A. Andersen. "Magnetic resonance image-guided implantation of chronic recording electrodes in the macaque intraparietal sulcus." Journal of neuroscience methods 130, no. 1 (2003): 1-8.

[157] Ladd, Mark E., Peter Bachert, Martin Meyerspeer, Ewald Moser, Armin M. Nagel, David G. Norris, Sebastian Schmitter, Oliver Speck, Sina Straub, and Moritz Zaiss. "Pros and cons of ultra-high-field MRI/MRS for human application." Progress in nuclear magnetic resonance spectroscopy 109 (2018): 1-50.

[158] H. S. Ho, "Safety of metallic implants in magnetic resonance imaging," *J. Magn. Reson. Imaging*, vol. 14, no. 4, pp. 472–477, 2001.

[159] S. A. Mohsin, J. Nyenhuis, and R. Masood, "Interaction of medical implants with the MRI electromagnetic fields," *Prog. Electromagn. Res. C*, vol. 13, pp. 195–202, 2010.

[160] Zhao, Siyuan, Xiaojun Liu, Zheng Xu, Huaying Ren, Bing Deng, Miao Tang, Linlin Lu et al. "Graphene encapsulated copper microwires as highly MRI compatible neural electrodes." Nano letters 16, no. 12 (2016): 7731-7738.

[161] Beygi, Mohammad, John T. Bentley, Christopher L. Frewin, Cary A. Kuliasha, Arash Takshi, Evans K. Bernardin, Francesco La Via, and Stephen E. Saddow. "Fabrication of a Monolithic Implantable Neural Interface from Cubic Silicon Carbide." Micromachines 10, no. 7 (2019): 430.

[162] T. Maeder, L. Sagalowicz, and P. Muralt, "Stabilized platinum electrodes for ferroelectric film deposition using Ti, Ta and Zr adhesion layers," *Jpn. J. Appl. Phys.*, vol. 37, no. 4R, p. 2007, 1998.

[163] Doty, F. David, George Entzminger, Jatin Kulkarni, Kranti Pamarthy, and John P. Staab. "Radio frequency coil technology for small- animal MRI." NMR in Biomedicine: An International Journal Devoted to the Development and Application of Magnetic Resonance In vivo 20, no. 3 (2007): 304-325.

[164] C. Chih-Liang, C. M. Collins, S. Li, B. J. Dardzinski, and M. B. Smith, "with Desired Current Pattern and Resonant Frequency," *Concepts Magn Reson*, vol. 15, no. 2, pp. 156–163, 2002.

[165] J. G. Bouwman and C. J. G. Bakker, "Alias subtraction more efficient than conventional zero- padding in the Fourier- based calculation of the susceptibility induced perturbation of the magnetic field in MR," *Magn. Reson. Med.*, vol. 68, no. 2, pp. 621–630, 2012.

[166] Sasaki, Wataru, and Joji Kinoshita. "Piezoresistance and Magnetic Susceptibility in Heavily Doped n-Type Silicon." Journal of the Physical Society of Japan 25, no. 6 (1968): 1622-1629.

[167] C. L. Frewin, J. J. Register, S. E. Saddow, M. Reyes-Natal, and J. J. Pancrazio, "Magnetic resonant imaging safe stylus." Google Patents, 14-Aug-2018.

Appendix A: Copyright Permissions

The permissions presented here belong to the figures and tables in chapter 1 and 2.

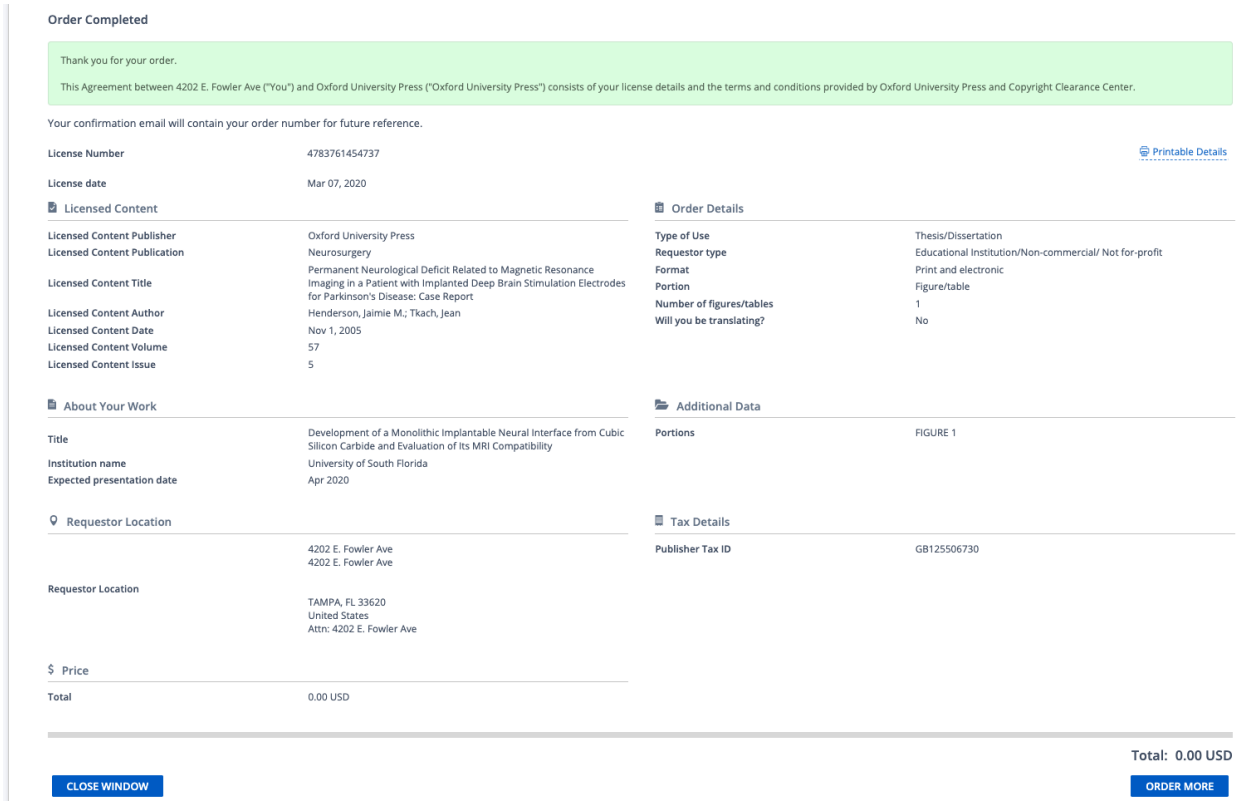

Order Completed

Thank you for your order.

This Agreement between 4202 E. Fowler Ave ("You") and Oxford University Press ("Oxford University Press") consists of your license details and the terms and conditions provided by Oxford University Press and Copyright Clearance Center.

Your confirmation email will contain your order number for future reference.

Printable Details

License Number	4783761454737
License date	Mar 07, 2020

Licensed Content

Licensed Content Publisher	Oxford University Press
Licensed Content Publication	Neurosurgery
Licensed Content Title	Permanent Neurological Deficit Related to Magnetic Resonance Imaging in a Patient with Implanted Deep Brain Stimulation Electrodes for Parkinson's Disease: Case Report
Licensed Content Author	Henderson, Jaimie M.; Tkach, Jean
Licensed Content Date	Nov 1, 2005
Licensed Content Volume	57
Licensed Content Issue	5

Order Details

Type of Use	Thesis/Dissertation
Requestor type	Educational Institution/Non-commercial/ Not for-profit
Format	Print and electronic
Portion	Figure/table
Number of figures/tables	1
Will you be translating?	No

About Your Work

Title	Development of a Monolithic Implantable Neural Interface from Cubic Silicon Carbide and Evaluation of Its MRI Compatibility
Institution name	University of South Florida
Expected presentation date	Apr 2020

Additional Data

Portions	FIGURE 1

Requestor Location

	4202 E. Fowler Ave 4202 E. Fowler Ave
Requestor Location	TAMPA, FL 33620 United States Attn: 4202 E. Fowler Ave

Tax Details

Publisher Tax ID	GB125506730

Price

Total	0.00 USD

Total: 0.00 USD

CLOSE WINDOW

ORDER MORE

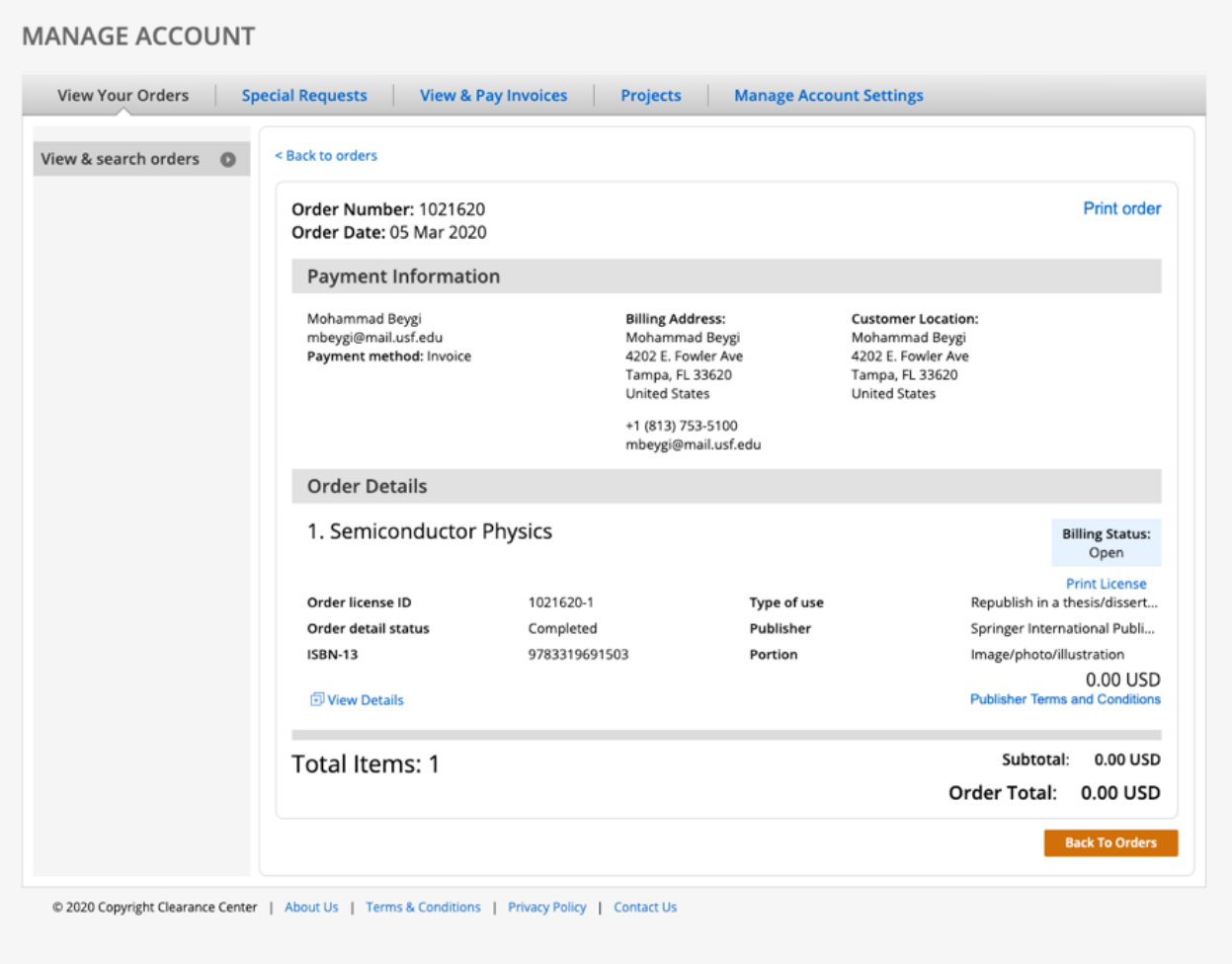
MANAGE ACCOUNT
View Your Orders
Special Requests
View & Pay Invoices
Projects
Manage Account Settings
View & search orders
< Back to orders
Order Number: 1021620
Order Date: 05 Mar 2020
Print order
Payment Information
Mohammad Beygi
mbeygi@mail.usf.edu
Payment method: Invoice
Billing Address:
Mohammad Beygi
4202 E. Fowler Ave
Tampa, FL 33620
United States
+1 (813) 753-5100
mbeygi@mail.usf.edu
Customer Location:
Mohammad Beygi
4202 E. Fowler Ave
Tampa, FL 33620
United States
Order Details
1. Semiconductor Physics
Billing Status:
Open
Print License
Order license ID 1021620-1
Order detail status Completed
ISBN-13 9783319691503
Type of use Republish in a thesis/dissert...
Publisher Springer International Publi...
Portion Image/photo/illustration
0.00 USD
View Details
Publisher Terms and Conditions
Total Items: 1
Subtotal: 0.00 USD
Order Total: 0.00 USD
Back To Orders
© 2020 Copyright Clearance Center | About Us | Terms & Conditions | Privacy Policy | Contact Us

Thank you for your order!

Dear Mohammad Beygi,

Thank you for placing your order through Copyright Clearance Center's RightsLink® service.

Order Summary

Licensee:	4202 E. Fowler Ave
Order Date:	Mar 5, 2020
Order Number:	4782640563940
Publication:	Elsevier Books
Title:	Silicon Carbide Biotechnology
Type of Use:	reuse in a thesis/dissertation
Order Total:	0.00 USD

View or print complete details of your order and the publisher's terms and conditions.

Sincerely,

Copyright Clearance Center

Tel: +1-855-239-3415 / +1-978-646-2777
customercare@copyright.com
https://myaccount.copyright.com

WILEY

Book: Physics of Semiconductor Devices, 3rd Edition
Author: Kwok K. Ng Simon M. Sze
Publisher: John Wiley and Sons
Date: Oct 1, 2006

Order Completed

Thank you for your order.

This Agreement between 4202 E. Fowler Ave ("You") and John Wiley and Sons ("John Wiley and Sons") consists of your license details and the terms and conditions provided by John Wiley and Sons and Copyright Clearance Center.

Your confirmation email will contain your order number for future reference.

License Number	4784820216235
License date	Mar 09, 2020

Licensed Content

Licensed Content Publisher	John Wiley and Sons
Licensed Content Publication	Wiley Books
Licensed Content Title	Physics of Semiconductor Devices, 3rd Edition
Licensed Content Author	Kwok K. Ng Simon M. Sze
Licensed Content Date	Oct 1, 2006
Licensed Content Pages	1

Order Details

Type of use	Dissertation/Thesis
Requestor type	University/Academic
Format	Print and electronic
Portion	Figure/table
Number of figures/tables	1
Will you be translating?	No

About Your Work

Title of your thesis / dissertation	Development of a Monolithic Implantable Neural Interface from Cubic Silicon Carbide and Evaluation of Its MRI Compatibility
Expected completion date	Apr 2020
Expected size (number of pages)	1

Additional Data

Original Wiley figure/table number(s)	Fig. 1 (3.2)

Requestor Location

	4202 E. Fowler Ave 4202 E. Fowler Ave
Requestor Location	TAMPA, FL 33620 United States Attn: 4202 E. Fowler Ave

Tax Details

Publisher Tax ID	EU826007151

$ Price

Total	0.00 USD

WILEY

Book: Fundamentals of Silicon Carbide Technology
Chapter: Index
Publisher: John Wiley and Sons
Date: Sep 26, 2014

Order Completed

Thank you for your order.

This Agreement between 4202 E. Fowler Ave ("You") and John Wiley and Sons ("John Wiley and Sons") consists of your license details and the terms and conditions provided by John Wiley and Sons and Copyright Clearance Center.

Your confirmation email will contain your order number for future reference.

License Number	4784850757707
License date	Mar 09, 2020

Printable Details

Licensed Content

Licensed Content Publisher	John Wiley and Sons
Licensed Content Publication	Wiley Books
Licensed Content Title	Index
Licensed Content Date	Sep 26, 2014
Licensed Content Pages	10

Order Details

Type of use	Dissertation/Thesis
Requestor type	University/Academic
Format	Print and electronic
Portion	Figure/table
Number of figures/tables	1
Will you be translating?	No

About Your Work

Title of your thesis / dissertation	Development of a Monolithic Implantable Neural Interface from Cubic Silicon Carbide and Evaluation of Its MRI Compatibility
Expected completion date	Apr 2020
Expected size (number of pages)	1

Additional Data

Original Wiley figure/table number(s)	Figure 2.2

Requestor Location

	4202 E. Fowler Ave 4202 E. Fowler Ave
Requestor Location	TAMPA, FL 33620 United States Attn: 4202 E. Fowler Ave

Tax Details

Publisher Tax ID	EU826007151

$ Price

Total	0.00 USD

WILEY

Book: RF Coils for MRI
Author: J. Thomas Vaughan John R. Griffiths
Publisher: John Wiley and Sons
Date: Nov 1, 2012

Order Completed

Thank you for your order.

This Agreement between 4202 E. Fowler Ave ("You") and John Wiley and Sons ("John Wiley and Sons") consists of your license details and the terms and conditions provided by John Wiley and Sons and Copyright Clearance Center.

Your confirmation email will contain your order number for future reference.

License Number	4784860101703
License date	Mar 09, 2020

Licensed Content

Licensed Content Publisher	John Wiley and Sons
Licensed Content Publication	Wiley Books
Licensed Content Title	RF Coils for MRI
Licensed Content Author	J. Thomas Vaughan John R. Griffiths
Licensed Content Date	Nov 1, 2012
Licensed Content Pages	1

Order Details

Type of use	Dissertation/Thesis
Requestor type	University/Academic
Format	Print and electronic
Portion	Figure/table
Number of figures/tables	1
Will you be translating?	No

About Your Work

Title of your thesis / dissertation	Development of a Monolithic Implantable Neural Interface from Cubic Silicon Carbide and Evaluation of Its MRI Compatibility
Expected completion date	Apr 2020
Expected size (number of pages)	1

Additional Data

Original Wiley figure/table number(s)	Figure 11.1.

Requestor Location

	4202 E. Fowler Ave 4202 E. Fowler Ave
Requestor Location	TAMPA, FL 33620 United States Attn: 4202 E. Fowler Ave

Tax Details

Publisher Tax ID	EU826007151

$ Price

Total	0.00 USD

Request Permission for use of Figures in PhD dissertation Inbox ×

Mohammad Beygi <mbeygi@mail.usf.edu> 1:01 PM (18 minutes ago)
to bmri

Dear Dr. Hornak,

I would like to use two figures in your online book (The bAsics of MRI) in my PhD dissertation. I would like to request written copyright permission for these two figures if possible.

Thanks in advance for your help.

Best regards,

--
Mohammad Beygi
Ph.D. Candidate
Electrical Engineering Department
University of South Florida
Tampa, FL, 33620
+1(813) 753-5100

Joseph Hornak <jphsch@rit.edu> 1:07 PM (12 minutes ago)
to me

Mohammad,
Thank you for asking. Yes, you have my permission to use the figures in your PhD dissertation. Please cite/credit them in the usual manner. Best wishes.
Joe

Joseph P. Hornak, Ph.D.

Professor of Chemistry & Imaging Science
Rochester Institute of Technology
Rochester, NY 14623-5604

Pros and cons of ultra-high-field MRI/MRS for human application

Author:
Mark E. Ladd,Peter Bachert,Martin Meyerspeer,Ewald Moser,Armin M. Nagel,David G. Norris,Sebastian Schmitter,Oliver Speck,Sina Straub,Moritz Zaiss

Publication: Progress in Nuclear Magnetic Resonance Spectroscopy

Publisher: Elsevier

Date: December 2018

Appendix B: *all*-SiC Probe Masks

This section shows the masks that were used to fabricate the Michigan style *all*-SiC neural probe.

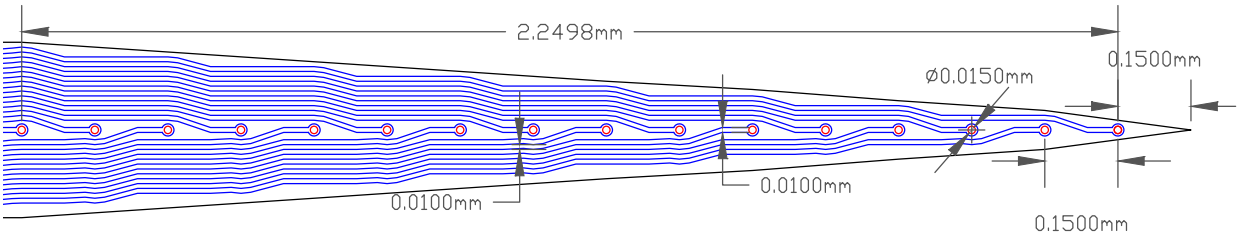

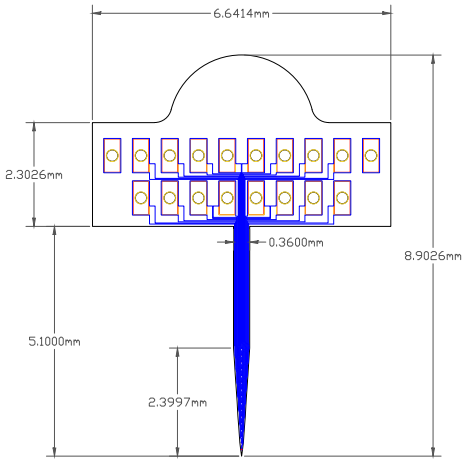

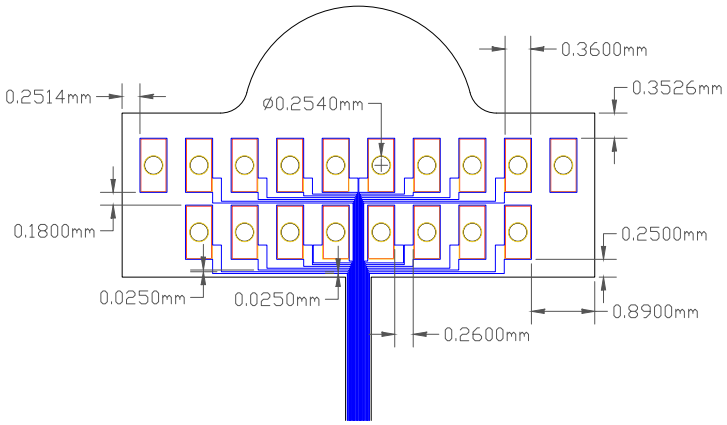

Appendix C: MRI Samples Masks

This section shows the masks that were used to fabricate the samples used for the MRI experiments.

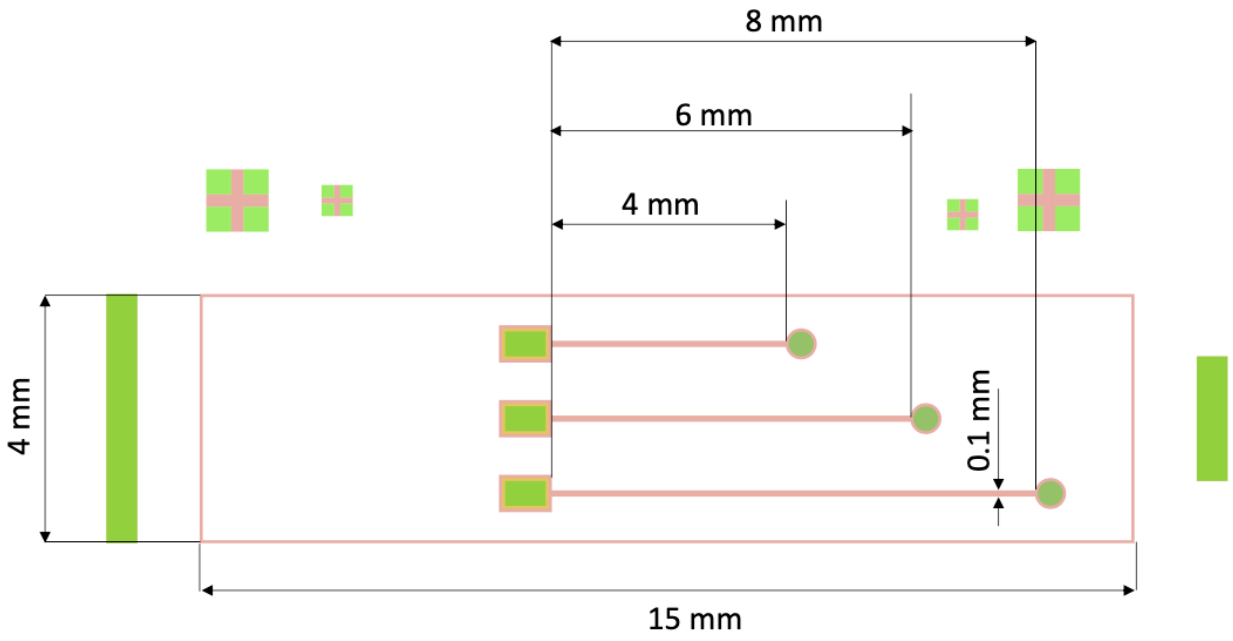

Appendix D: MATLAB Codes

This section presents the codes written in MATLAB to calculate B_0-field shift caused by magnetic susceptibility difference between the tissue phantom and the sample material which results in image artifacts under MRI.

```
%% Fourier Based Field-shift Calculation for MRI (Mo's Samples)

% calculates magnetic field shifts in various samples inside PAA phantom
%% Written 1-10-2020 by Mo Beygi (mbeygi@mail.usf.edu)

clear all; close all; clc;

%% creating a numerical phantom:

% - mimics actual sample size (width=4 mm, length=15 mm, thickness=varied)
% - with tissue-like (-9 ppm), Pt (+267 ppm), SiC (-12.87 ppm), Si (-3.24 ppm)
% susceptibility (dChi)
% - within an FOV of (256 x 256 x 256)

B0=7;
width = 40;
length = 10;
length2= 2;
thickness = 150;

N = 256;
dChiTissue = -9e-6;
dChiPt = 267e-6;
dChiSi = -3.24e-6;
dChiSiC = -12.87e-6;
voxelSize = [1 1 1];

% the sample is centric

M = round(0.5*N);
Nx =  N; Ny = N; Nz = N;
```

```
Mx =  M; My = M; Mz = M;

FOV = [Ny Nx Nz].*voxelSize;

% creating the susceptibility distribution
%-----------------------------------
%Pt on Si


dChi_3D1 = zeros(Ny, Nx, Nz);
dChi_3D1(:,:,:) = dChiTissue;

for i=(Mx-(width/2)):(Mx+(width/2))
   for j = (My-(length/2)):(My+(length/2))
      for k = (Mz-(thickness/2)):(Mz+(thickness/2))
         dChi_3D1 (i,j,k) = dChiSi;
      end
   end
end
i=0;
j=0;
k=0;

for i2=(Mx-(width/2)):(Mx+(width/2))
   for j2 = ((My+(length/2)+1)): ((My+(length/2)+1)+length2)
      for k2 = (Mz-(thickness/2)):(Mz+(thickness/2))
         dChi_3D1 (i2,j2,k2) = dChiPt;
      end
   end
end

i2=0;
j2=0;
k2=0;

%% The kernel in k-space:

kx_squared = ifftshift((-Nx/2:Nx/2-1)/FOV(2)).^2;
ky_squared = ifftshift((-Ny/2:Ny/2-1)/FOV(1)).^2;
kz_squared = ifftshift((-Nz/2:Nz/2-1)/FOV(3)).^2;
[kx2_3D,ky2_3D,kz2_3D] = meshgrid(kx_squared,ky_squared,kz_squared);
kernel = 1/3 - kz2_3D./(kx2_3D + ky2_3D + kz2_3D);
kernel(1,1,1) = 0;

%% Field shift calculations:
```

```
% with virtual zero-padding the result is:
dField_3D_noAliasing_Pt = B0*calculateFieldShift(dChi_3D1, voxelSize);

%-----------------------------------------------
%%SiC


dChi_3D2 = zeros(Ny, Nx, Nz);
dChi_3D2(:,:,:) = dChiTissue;

for i=(Mx-(width/2)):(Mx+(width/2))
   for j = (My-(length/2)):(My+(length/2))
      for k = (Mz-(thickness/2)):(Mz+(thickness/2))
         dChi_3D2 (i,j,k) = dChiSiC;
      end
   end
end
i=0;
j=0;
k=0;


%% The kernel in k-space:

kx_squared = ifftshift((-Nx/2:Nx/2-1)/FOV(2)).^2;
ky_squared = ifftshift((-Ny/2:Ny/2-1)/FOV(1)).^2;
kz_squared = ifftshift((-Nz/2:Nz/2-1)/FOV(3)).^2;
[kx2_3D,ky2_3D,kz2_3D] = meshgrid(kx_squared,ky_squared,kz_squared);
kernel = 1/3 - kz2_3D./(kx2_3D + ky2_3D + kz2_3D);
kernel(1,1,1) = 0;

%% Field shift calculations:

% with virtual zero-padding the result is:
dField_3D_noAliasing_SiC = B0*calculateFieldShift(dChi_3D2, voxelSize);

%-----------------------------------------------
%%Si


dChi_3D3 = zeros(Ny, Nx, Nz);
dChi_3D3(:,:,:) = dChiTissue;

for i=(Mx-(width/2)):(Mx+(width/2))
   for j = (My-(length/2)):(My+(length/2))
      for k = (Mz-(thickness/2)):(Mz+(thickness/2))
```

```
            dChi_3D3 (i,j,k) = dChiSi;
        end
    end
end
i=0;
j=0;
k=0;

%% The kernel in k-space:

kx_squared = ifftshift((-Nx/2:Nx/2-1)/FOV(2)).^2;
ky_squared = ifftshift((-Ny/2:Ny/2-1)/FOV(1)).^2;
kz_squared = ifftshift((-Nz/2:Nz/2-1)/FOV(3)).^2;
[kx2_3D,ky2_3D,kz2_3D] = meshgrid(kx_squared,ky_squared,kz_squared);
kernel = 1/3 - kz2_3D./(kx2_3D + ky2_3D + kz2_3D);
kernel(1,1,1) = 0;

%% Field shift calculations:

% with virtual zero-padding the result is:
dField_3D_noAliasing_Si = B0*calculateFieldShift(dChi_3D3, voxelSize);

%-----------------------------------------------


%% Displaying the results:

% setting a fixed intensity window, for good visual validation:
%intensityWindow = [min(dField_3D_noAliasing_Pt(:)), max(dField_3D_noAliasing_Pt(:))];
intensityWindow = [-3e-7, 1e-4];

scrsz = get(0,'ScreenSize'); % full screen looks better
figure('Position', scrsz, 'Units', 'normalized');
axes('Position',[0 0 1 1], 'Units','normalized');

% the results

%% Pt on Si
subplot(3,3,1);
imagesc(squeeze(dField_3D_noAliasing_Pt(:, :, Mz))',intensityWindow);axis equal tight
colorbar
%text(Nz*0.95,My,'\rightarrow','HorizontalAlignment','right','fontsize',35)
% text(Nz*0.65,My*1.1)
title('Platinum on Si - Axial',...
    'fontsize', 12);
%xlabel('axis perpendicular to B_0 \rightarrow');
```

```
% ylabel('B_0 direction \rightarrow');
axis equal tight;


% the estimated aliasing distribution
subplot(3,3,2);
imagesc(squeeze(dField_3D_noAliasing_Pt(:, Mx+(length/2)+(length2/2),
:))',intensityWindow);axis equal tight
colorbar
%text(Nz*0.95,My,'\rightarrow','HorizontalAlignment','right','fontsize',35)
%text(Nz*0.65,My*1.1,'pure aliasing','HorizontalAlignment',...
   % 'right', 'fontsize', 12)
title(strcat('Platinum on Si - Coronal'),'fontsize', 12);
%xlabel('axis perpendicular to B_0 \rightarrow');
ylabel('B_0 direction \rightarrow');
 axis equal tight;


% the final result of using virtual zero-padding:
subplot(3,3,3);
imagesc(squeeze(dField_3D_noAliasing_Pt(My, :, :))',intensityWindow);axis equal tight
colorbar
%text(Nz*0.95,My,'\rightarrow','HorizontalAlignment','right','fontsize',35)
%text(Nz*0.65,My*1.1,'cleared result','HorizontalAlignment',...
    %'right', 'fontsize', 12)
title('Platinum on Si - Sagittal','fontsize', 12);
%xlabel('axis perpendicular to B_0 \rightarrow');
ylabel('B_0 direction \rightarrow');
 axis equal tight;

 %% SiC
 subplot(3,3,4);
imagesc(squeeze(dField_3D_noAliasing_SiC(:, :, Mz))',intensityWindow);axis equal tight
colorbar
%text(Nz*0.95,My,'\rightarrow','HorizontalAlignment','right','fontsize',35)
% text(Nz*0.65,My*1.1)
title('SiC - Axial',...
    'fontsize', 12);
%xlabel('axis perpendicular to B_0 \rightarrow');
% ylabel('B_0 direction \rightarrow');
axis equal tight;


% the estimated aliasing distribution
subplot(3,3,5);
imagesc(squeeze(dField_3D_noAliasing_SiC(:, Mx, :))',intensityWindow);axis equal tight
```

```
colorbar
%text(Nz*0.95,My,'\rightarrow','HorizontalAlignment','right','fontsize',35)
%text(Nz*0.65,My*1.1,'pure aliasing','HorizontalAlignment',...
   % 'right', 'fontsize', 12)
title(strcat('SiC - Coronal'),'fontsize', 12);
%xlabel('axis perpendicular to B_0 \rightarrow');
ylabel('B_0 direction \rightarrow');
 axis equal tight;


% the final result of using virtual zero-padding:
subplot(3,3,6);
imagesc(squeeze(dField_3D_noAliasing_SiC(My, :, :))',intensityWindow);axis equal tight
colorbar
%text(Nz*0.95,My,'\rightarrow','HorizontalAlignment','right','fontsize',35)
%text(Nz*0.65,My*1.1,'cleared result','HorizontalAlignment',...
    %'right', 'fontsize', 12)
title('SiC - Sagittal','fontsize', 12);
%xlabel('axis perpendicular to B_0 \rightarrow');
ylabel('B_0 direction \rightarrow');
 axis equal tight;

 %% Si

 subplot(3,3,7);
imagesc(squeeze(dField_3D_noAliasing_Si(:, :, Mz))',intensityWindow);axis equal tight
colorbar
%text(Nz*0.95,My,'\rightarrow','HorizontalAlignment','right','fontsize',35)
% text(Nz*0.65,My*1.1)
title('Si Substrate - Axial',...
    'fontsize', 12);
%xlabel('axis perpendicular to B_0 \rightarrow');
% ylabel('B_0 direction \rightarrow');
axis equal tight;


% the estimated aliasing distribution
subplot(3,3,8);
imagesc(squeeze(dField_3D_noAliasing_Si(:, Mx, :))',intensityWindow);axis equal tight
colorbar
%text(Nz*0.95,My,'\rightarrow','HorizontalAlignment','right','fontsize',35)
%text(Nz*0.65,My*1.1,'pure aliasing','HorizontalAlignment',...
   % 'right', 'fontsize', 12)
title(strcat('Si Substrate - Coronal'),'fontsize', 12);
%xlabel('axis perpendicular to B_0 \rightarrow');
ylabel('B_0 direction \rightarrow');
```

```
 axis equal tight;


% the final result of using virtual zero-padding:
subplot(3,3,9);
imagesc(squeeze(dField_3D_noAliasing_Si(My, :, :))',intensityWindow);axis equal tight
colorbar
%text(Nz*0.95,My,'\rightarrow','HorizontalAlignment','right','fontsize',35)
%text(Nz*0.65,My*1.1,'cleared result','HorizontalAlignment',...
    %'right', 'fontsize', 12)
title('Si Substrate - Sagittal','fontsize', 12);
%xlabel('axis perpendicular to B_0 \rightarrow');
ylabel('B_0 direction \rightarrow');
 axis equal tight;
----------------------------------------------------------------------

% Fourier Based Field-shift Calculation for MRI
% - k-space Filtering (KF) implementation
% - implemented with 'virtual' zero-padding

%% Written 22-06-2012 by Job Bouwman (jgbouwman@hotmail.com)
% Update 14-06-2013: to cope with anisotropic voxel size
% Update 26-01-2014: implemented a numerical trick to further increase the
%         calculation speed with ~30% . As all distributions are real
%         in the spatial domain, the imaginary channel of the convolution
%         can be used for a second convolution. This channel is exploited
%         to calculate the aliasing distribution.
% Update 20-10-2014: the use of nested functions allows larger matrices
%         again 13% faster, by using more efficient nested functions

%% method description (including scientific references)
% This is an efficient implementation of the Fourier-based procedure to
% calculate the susceptibility-induced field-shift if an object
% with known susceptibility distribution (dChi_3D) is placed within
% a strong homogeneous magnetic field (B0).

% This method is based on the publication of:
% Salomir et al, "A fast calculation method for magnetic field
% inhomogeneity due to an arbitrary distribution of bulk susceptibility"
% Concepts in Magnetic Resonance Part B: Magnetic Resonance Engineering,
% Volume 19B, Issue 1, pages 26–34, 2003

% However, the original method needs (inefficient zero-padding)
% Cheng YCN, Neelavalli J, Haacke EM. "Limitations of calculating field
% distributions and magnetic susceptibilities in MRI using a Fourier
% based method". Phys Med Biol 2009;54:1169–1189
```

```
% In the proposed method here, aliasing is removed by estimating
% this artifact using an additional convolution in a lower resolution,
% which is feasible due to the smooth decay of the dipole function.
% The article describing the principle of low resolution aliasing
% subtraction:
% Job G. Bouwman, Chris J.G. Bakker. "Alias subtraction more efficient than
% conventional zero-padding in the Fourier-based calculation of the
% susceptibility induced perturbation of the magnetic field in MR"
% 2012, Magnetic Resonance in Medicine 68:621630 (2012).
% Please refer to this article when using this script.


%% How to use this file:
% dChi_3D is your 3D susceptibility distribution
%   * the third dimension of dChi_3D is the one parallel to B0.
%   * the values of your dChi_3D are assumed to be relative to the
%     dChi of the embedding medium. In practice this will either be:
%     - relative to the dChi of air (0.36 ppm) if you want to calculate the
%       field for example in a complete head model
%     - relative to the dChi of tissue (-9.05 ppm) if you want to calculate
%       the local effect of for example a small implant embedded in tissue.
% voxelSize (either in mm, centimeter, or inches)
%    * we use the matlabconvention: [dy, dx, dz]

% Example:
%    B0 = 3; % tesla;
%    voxelSize = [1 1 2]; % mm
%    gyromagneticRatio = 2*pi*42.58e6
%
%    dB = B0*calculateFieldShift(dChi_3D, voxelSize);
%    dOhmega = dB*gyromagneticRatio;

function dField_3D = calculateFieldShift(varargin)


    % Checking the input parameters:
    if or(nargin < 1, nargin > 2)
        error('Please supply two arguments (dChi_3D and voxelSize).');
    end
    dChi_3D = varargin{1};
    if or(length(size(dChi_3D)) ~= 3,  min(size(dChi_3D)) < 2)
        error('Input dChi_3D must be of dimension 3.');
    end

    if nargin == 2
```

```
    voxelSize = squeeze(varargin{2});
    if or(size(voxelSize,2)~=3, size(voxelSize,1)~=1)
        error('voxelSize must be a vector of length 3.');
    end
else
    display(['In calculateFieldShift.m the voxelSize was not '...
            'specified. The script assumed it to be isotropic:']);
    voxelSize = [1,1,1]
end

% making sure that the size of the distribution in each dimension
% is a multiple of four:
[NyInput, NxInput, NzInput] = size(dChi_3D);
if mod(NxInput,4)+mod(NyInput,4)+mod(NzInput,4) > 0
    conventionalPad = mod(4-...
        [mod(NyInput,4),mod(NxInput,4),mod(NzInput,4)], 4);
    dChi_3D = padarray(dChi_3D,conventionalPad,'post');
end
FOV = voxelSize.*size(dChi_3D);

%% The Fourier-based convolution:
% 1) The forward Fourier Transform (FT):
    % NB: Instead of doing an extra convolution to calculate the
    % effect of aliasing (as proposed in the article), here we use
    % the 'imaginary channel' to do this.
    % This is done by downscaling the artificial environment, and
    % adding this as an imaginary component to the original
    % (unpadded) susceptibility distribution. Together this is
    % referred to as the "DUAL" distribution:
    FT_dChi_3D_DUAL = fftn(dChi_3D + 1i*Zc(D(dChi_3D)));
          clear dChi_3D;
% 2) multiplication with the dipole function:
    FT_dField_3D = FT_dChi_3D_DUAL.*KF_kernel(FOV,size(FT_dChi_3D_DUAL));
          clear FT_dChi_3D_DUAL;
% 3) inverse FT to spatial domain:
    dField_3D_DUAL = ifftn(FT_dField_3D);
          clear FT_dField_3D;
% 4) Subtracting the upscaled, cropped center of the aliasing:
    dField_3D = real(dField_3D_DUAL) - UC(imag(dField_3D_DUAL));
         clear dField_3D_DUAL;

% returning the field shift in the same size:
if mod(NxInput,4)+mod(NyInput,4)+mod(NzInput,4) > 0
    dField_3D = dField_3D(1:NyInput, 1:NxInput, 1:NzInput);
end
```

```
% END OF MAIN FUNCTION


% NESTED functions:
% (before the update of 20-10-2014 these were subfunctions)
function kernel = KF_kernel(FOV,N)
   % FOV : field of view in x, y, and z directions
   % N   : no of samples in kx, ky, kz
   kx_squared = ifftshift((-N(2)/2:N(2)/2-1)/FOV(2)).^2;
   ky_squared = ifftshift((-N(1)/2:N(1)/2-1)/FOV(1)).^2;
   kz_squared = ifftshift((-N(3)/2:N(3)/2-1)/FOV(3)).^2;

   [kx2_3D,ky2_3D,kz2_3D] = meshgrid(kx_squared,ky_squared,kz_squared);

   kernel = 1/3 - kz2_3D./(kx2_3D + ky2_3D + kz2_3D);
   kernel(1,1,1) = 0;
end

function DX = D(X)
   % downscales a 3D distribution by factor two, by collapsing each cube
   % of eight voxels into one single voxel (average value)
   DX =      X(1:2:end,1:2:end,1:2:end);
   DX = DX + X(1:2:end,1:2:end,2:2:end);
   DX = DX + X(1:2:end,2:2:end,1:2:end);
   DX = DX + X(1:2:end,2:2:end,2:2:end);
   DX = DX + X(2:2:end,1:2:end,1:2:end);
   DX = DX + X(2:2:end,1:2:end,2:2:end);
   DX = DX + X(2:2:end,2:2:end,1:2:end);
   DX = DX + X(2:2:end,2:2:end,2:2:end);
   DX = DX/8;
end

function ZcX = Zc(X)
   % This operator is complementary to zero-padding: the result is
   % a void space embedded in an environment of copies of X.
   % The resulting 3D distribution is 2 times as large
   % as the original in each dimension
   Nx = 2*size(X, 2);  mid_x   = (Nx/4+1):(Nx*3/4);
   Ny = 2*size(X, 1);  mid_y   = (Ny/4+1):(Ny*3/4);
   Nz = 2*size(X, 3);  mid_z   = (Nz/4+1):(Nz*3/4);
   ZcX = repmat(circshift(X, [Ny/4, Nx/4, Nz/4]), [2 2 2]);
   ZcX(mid_y, mid_x, mid_z) = 0;
end

function center = UC(domain)
   % UC = Upscaling + Cropping:
```

```
      % both crops as upscales (factor 2) the central part of a larger
      % distribution. Therefore the size of input ('domain') and output
      % ('center') are the same.
      Nx = size(domain,2); Mx=round(1/4+Nx/4+(1:Nx)/2); Sx=Mx+(-1).^(1:Nx);
      Ny = size(domain,1); My=round(1/4+Ny/4+(1:Ny)/2); Sy=My+(-1).^(1:Ny);
      Nz = size(domain,3); Mz=round(1/4+Nz/4+(1:Nz)/2); Sz=Mz+(-1).^(1:Nz);

      center =          27/64*domain(My,Mx,Mz);
      center = center +  9/64*domain(My,Mx,Sz);
      center = center +  9/64*domain(My,Sx,Mz);
      center = center +  3/64*domain(My,Sx,Sz);
      center = center +  9/64*domain(Sy,Mx,Mz);
      center = center +  3/64*domain(Sy,Mx,Sz);
      center = center +  3/64*domain(Sy,Sx,Mz);
      center = center +  1/64*domain(Sy,Sx,Sz);
   end
end
```